Microstructure, nanostructure, and local crystallography in perovskite ferroelectrics and antiferroelectrics.

Rafael Villaurrutia Arenas

A Thesis submitted for the degree of Doctor of Philosophy

University of Glasgow

October 2010

Declaration

This thesis has been written solely by myself and details the research I have carried out within the Solid State Physics Group in the Department of Physics and Astronomy at the University of Glasgow. The work described is my own except where otherwise stated.

This Thesis has not been submitted in any previous application for a higher degree.

January 19, 2011

Contents

List of Figures

Acknowledgements

Foremost, I would like to thank my supervisor, Dr Ian MacLaren. He has been an excellent mentor, teaching me all he could with lovely patience . I will always be impressed by his vast and quick intellect, ability to manage several projects at once and his willingness to participate in all aspects of research. I have also received great support from all the people of SSP group at the University of Glasgow, especially Dr Sam McFadzean, Brian Miller, Collin How and William Smith. My students colleagues and postdocs of SSP group and the University of Glasgow itself. I would like to thank to Dr Umar Farooq for everything he taugth to me and for his friendship. I would like to thank to CONACYT for the provision of a PhD studentship.

Abstract

Selected area and Kikuchi diffraction patterns, traditional bright field and dark field imaging techniques in electron microscopy as well as high resolution TEM and STEM techniques, together with electron backscattered electron diffraction technique have been used to study the domain structures, local crystallography and atomic structures in PZT-based materials. Reliable EBSD mapping of 90° domains in a tetragonal $Pb(Zr_x, Ti_{1-x})O_3$ with $x = 0.5$ ferroelectric perovskite has been achieved for the first time, together with reliable automated orientation determination from TEM-Kikuchi patterns. This has been used to assess the local crystallography of domains by determining misorientation angles at 90° domain boundaries and thus local c/a ratios. In most cases, a good agreement is found between local c/a ratios and global measurements by X-ray diffraction, but some clear discrepancies have also been found suggesting that real local variations are present, perhaps as a consequence of compositional inhomogeneities.

The details of the domain structure of the incommensurate antiferroelectric structure in La-doped zirconium-rich lead zirconate titanate have been revealed in detail for the first time. The structure is dominated by 60° domain boundaries close to {101} planes of the primitive perovskite cell; and tilts of the perovskite sublattice of about 0.5° are also noted at such boundaries consistent with a small tetragonal distortion of the primitive cell. Within each domain a streaked nanostructure is revealed under weak diffraction conditions perpendicular to the long b-axis of the incommensurate supercell, which appears to be a consequence of planar faulting perpendicular to this b-axis. 90° domain boundaries are also observed but are less frequent than 60° boundaries and in contrast to previous reports, these often have rather curved and irregular boundary planes. The atomic arrangement of these 90° boundaries was studied by aberration corrected HRSTEM. Different stackings and periodicities were identified.

Chapter 1

Introduction

Understanding the relationship between structure and properties can lead to both physical insight and enhanced materials properties. In that sense, electron microscopy techniquesare powerful tools to analyse the structure and structure changes in materials. Because the attainable scattered intensities for electrons are many times larger than those for x-rays, electron diffraction allows us to study the interior structure of matter down to a few cubic-nanometres in size. Ferroelectric materials allow for a variety of intriguing applications, due to their piezoelectric and polarisation-switching properties. The latter has led to exciting recent technologies such as the ferroelectric random access memories, used for non-volatile memory storage in information technology. A ferroelectric is an insulating system with two or more discrete stable or metastable states of non-zero electric polarisation in zero applied electric field, referred to as "spontaneous" polarisation. In ferroelectric crystals, the spontaneous polarisation is produced by the displacement of ions in the crystal structure, depending on their positions in the unit cell. One structure that makes possible such atomic arrangement of ions and allows the polarisation-switching to happen is the perovskite structure. One of the most interesting compositions of perovskite oxides is the Lead Zirconate Titanate (PZT) range of compositions; $Pb(Zr_x, Ti_{1-x})O_3$, based piezoelectric ceramics are an important class of functional materials and are widely used as sensors, transducers, actuators, multilayer capacitors, and as mentioned above, ferroelectric memory devices. These ceramics develop a spontaneous electrical polari-

sation below the Curie temperature and this is usually coupled with a crystallographic distortion; this coupling between crystallographic distortion and electrical polarisation leading to the piezoelectric effect. In order to minimise both strain and electrostatic energies, domains are formed in the grains with different polarisation orientations and these normally form boundaries at specific crystallographic planes to minimise strain. PZT ceramics with $x < 52.5\%$ adopt a tetragonally distorted perovskite crystal structure below the Curie temperature, and as a consequence of the significant distortion of the unit cell ($> 2\%$), lamellar domain structures are formed with the domain boundaries on stress-free $\{101\}$ planes and the unit cells in the two domains related by a rotation of nearly 90° about a $\langle 010 \rangle$ axis. The exact rotation angle is related to the c/a ratio of the material through the formula: $\mathrm{c/a} = 1/\tan([90^\circ - \delta]/2)$, where δ is the deviation from 90° [1]. There have been suspicions in the past that the composition and structure of PZT is not always homogeneous due to processing considerations, and therefore methods for assessing local (sub-micron scale) crystallography are likely to be very useful. This local crystallography can be assessed using orientation mapping in electron microscopy, provided the accuracy of orientation determination is sufficient ($\sim 0.1^\circ$). On the other hand, in a macroscopic arrangement, all three possible orientations of the [001] axis need to be present to ensure zero overall strain as a result of the ferroelectric transformation, and this imposes the requirement of a more complex structure containing different lamellar arrangements within the same grain; in large-grained materials this often results in the formation of the so-called herringbone structure which has been discussed in detail by Arlt and Sasko [2]. Unfortunately, the junctions between the different lamellar structure are inevitably strained, and must therefore act as stress concentrations [3]. In order to decrease the high stress concentrations at the domain boundaries and to change the polarisation and switching behaviour, these ceramics are doped with different elements. One of the most interesting dopants due to the different phase transitions induced in the system is the lanthanum dopant. Lanthanum doping $Pb(Zr_x, Ti_{1-x})O_3$ materials was found to increase the stability range of the antiferroelectric orthorhombic state on the Zr-rich side of the phase diagram [4,5]. Thus, the La modifier is an antiferroelectric

intensifier for $Pb(Zr_x, Ti_{1-x})O_3$ based ceramics as it converts a ferroelectric phase into an antiferroelectric one [6]. Antiferroelectric materials also have potential applications on devices in microelectronics applications due to their unique dielectric, piezoelectric, and electro-optical properties [7]. These features of antiferroelectric materials are a consequence of a ferroelectric-antiferroelectric phase transition. Such transformations can be studied based on the modulated structures derived during the structure transformations. Lead zirconate titanate ceramics with a Zr:Ti ratio of 90:10 and doped with 2-4 % La display an incommensurate antiferroelectric phase with a long period ordering along a perovskite [110] direction, but with a periodicity of 7-8 (110) spacings [10]. Many details of the domain structure and atomic structure of the incommensurate phase remain unclear to date and have been investigated in detail in this thesis. Chapter 2 of this thesis is a brief review of the ferroelectricity in ceramics which explains the importance of PZT ceramics in technological applications, its crystallographic features, and the differences between the doped and undoped PZT. Chapter 3 explains the principles of the experimental and analysis methods used in the experiments. Firstly, the mathematics of misorientation in crystals is outlined including the use of Euler angle description. Secondly, the techniques used to prepare the ceramics for TEM and EBSD analysis are reviewed, as ceramics are non-conducting materials and the preparation process is not trivial. Finally, the principles of the microscopy techniques and their relevance in this work are outlined. These two chapters deals with the fundamental principles of ferroelectricity and the applications and characteristics of ferroelectric materials; the principles of the mathematics used in this work and the physics of the microscope techniques used in this work. Nevertheless, these chapters should not be treated as a reference on ferroelectricity, nor on electron microscopy, both of which have been extensively reviewed by many authors. Rather, they attempt to provide a brief overview of the material which is of specific relevance to the original research work presented in the later chapters of this thesis. Chapter 4 concentrates on showing the automated methods developed for accurate and unambiguous indexing of domain orientations in PZT ceramics using both electron backscatter diffraction (EBSD) and transmission electron microscopy (TEM)

Kikuchi patterns, assessing the accuracy of such techniques and the effect of errors/noise on the results, and using these to make some initial comparisons of local and bulk crystallography. These results constitute the basics of the crystallographic analysis of the PZT tetragonal phase which is the main aim of this thesis work. Chapter 5 has a brief review of the principles of modulated structures and incommensurate phases as a starting point for the analysis of the Lanthanum doped PZT. This is followed by a discussion of the ferroelectric-antiferroelectric phase transition of PLZT, as well as the different features of such materials. Finally, the bulk of this chapter is concerned with a detailed electron microscopy study of microstructure and nanostructure of the incommensurate antiferroelectric phase, as well as initial studies on its atomic structure. Finally, chapter 6 presents the conclusions and future work. It should also be made clear that much of the work presented in this thesis has been already published in three papers [8,9,10] referenced at appropriate places in this thesis.

Bibliography

[1] MacLaren, I., Schmitt, L.A., Fuess, H., Kungl, H., Hoffmann, M.J., J. Appl. Phys. 97, 094102 (2005).

[2] Artl, G., and Sasko, J., J. Appl. Phys. 51, 4956, (1980).

[3] Damjanovic, D., Rep. Prog. Phys. 61 1267-1324, (1998).

[4] Li, J.F., Dai, X., Chow, A., Viehland, D., J. Mater. Res. 10, 926,(1995).

[5] Shebanov, L., Kusnetsov, M., Sternberg, A., J. Appl. Phys. 76,4301, (1994).

[6] Feng, Y., Xu, Z., Li, H., Yao, X., Ceramics International, 30, 1393-1396, (2004).

[7] Xu, B., Moses, P., Pai, N.G., Cross, L.E., Appl. Phys. Lett. 72,(5), 593-595, (1998).

[8] Farooq, M.U., Villaurrutia, R., MacLaren, I., Burnett, T.L., Comyn, T.P.,Bell, A.J.,Kungl, H., and Hoffmann, M.J. , J. Appl. Phys., 104, 024111, (2008).

[9] Farooq, M.U., Villaurrutia, R., MacLaren, I., Kungl, H., Hoffmann, M.J., Fundenberger, J.-J. and Bouzy, E., Journal of Microscopy, 230, 445, (2008).

[10] Villaurrutia, R., MacLaren, I., Pelaiz, A., Journal of Physics Conference series, EMAG conference, (2009).

Chapter 2

Ferroelectricity in ceramics

Ferroelectric ceramics have long been used as sensors and actuators due to their piezoelectric properties. They are capable of high frequency response and are thus ideal for ultrasonic applications. Recently, attention has focused on developing materials for ferroelectric memory applications. This chapter deals with the fundamental principles of ferroelectricity and the applications and characteristics of ferroelectric materials. Nevertheless, this chapter should not be treated as a reference on ferroelectricity, which has been extensively reviewed by many authors. Rather, it attempts to provide a brief overview of the principles and relevance of these materials. Section 2.1 is a revision of the principles and the principal variables for ferroelectric phenomena. Subsection 2.1.1 deals with the paraelectric-ferroelectric phase transition as this is of the utmost importance in this thesis. Subsection 2.1.2 is a revision of the unit cell distortions due to the different phase transformations in ferroelectrics, as well as the formation of domains. Subsection 2.1.3 covers the different physical properties characteristics of ferroelectric materials and its origins. Section 2.2 is a review of the properties and applications of PZT ceramic as a ferroelectric material, as it is the material studied in this thesis. Section 2.3 provides an overview of the importance and characteristics of the microstructure and crystallographic features of PZT. Finally, section 2.4 covers the characteristics and applications of doped PZT.

2.1 Ferroelectricity

A dielectric crystal is an insulator by definition, wherein no transport phenomena occur [1]. In such materials the polarisation effects caused by applying an external electric field are too small to cause an observable change in the physical properties, such as elastic, optical or thermal behaviour [2]. Nonetheless, there exist a large, but limited number of crystals that exhibit polarisation values many orders of magnitude bigger than the dielectric crystals. The phenomenon exhibited by these crystals is called *ferroelectricity*, and the crystals exhibiting these phenomena are called ferroelectric. Ferroelectricity is a spontaneous electric polarisation of a crystal, which can be reversed or rotated by applying an external electric field [5]. The term ferroelectricity is used in analogy to the term *ferromagnetism*. Just as ferromagnetic crystals exhibit a spontaneous magnetic moment and hysteresis effects in the relationship between magnetisation and magnetic field, ferroelectric crystals show a spontaneous polarisation and hysteresis effects in the relationship between dielectric displacement and electric field [2]. Ferromagnetism was already known in materials like iron, when ferroelectricity was discovered in 1920 in Rochelle salt by Valasek [7]. Thus, the prefix *ferro* meaning "iron", was used to describe this property in spite of the fact that most ferroelectrics do not have iron in their unit cells. In the dielectric materials, the constituent atoms are considered to be ionized to a certain degree and are either positively or negatively charged. In such ionic crystals, when an electric field is applied, cations are attracted to the cathode and anions to the anode due to electrostatic interaction. The electron clouds are deformed causing electron dipoles. The elctron clouds also deform, causing electric dipoles. This phenomenon is known as *electric polarisation*. Lets assume that dipole moments result from the displacement of one type of ion A (electric charge q) relative to the crystal lattice. Consider the case in which the polarisation is caused by all the A ions being displaced equally in a lattice. It follows that, at any individual A ion site, there exists a local field from the surrounding polarisation $\mathbf{P}$, even if there is no external field [27]. It can be shown that:

$$E_{local} = E_0 + \sum_i \frac{3(p_i \cdot r_i)r_i - r_i^2 p_\imath}{4\pi\varepsilon_0 r_i^5} \tag{2.1}$$

hence,

$$E_{local} = (\frac{\gamma}{3\varepsilon_0})\mathbf{P} \tag{2.2}$$

This local field is the driving force for the ion shift. Here γ is called the *Lorentz factor* and ε_0 is the permittivity. If the ionic polarisability of ion A is α, then the dipole moment of the unit cell of this crystal is:

$$\mu = (\frac{\alpha\gamma}{3\varepsilon_0})\mathbf{P} \tag{2.3}$$

The energy of this dipole moment (dipole-dipole coupling) is

$$w_{dip} = -\mu_{local} = -(\frac{\alpha\gamma^2}{9\varepsilon_0^2})\mathbf{P}^2 \tag{2.4}$$

Defining N to be the number of atoms per unit volume:

$$W_{dip} = N w_{dip} = -(\frac{N\alpha\gamma^2}{9\varepsilon_0^2})\mathbf{P}^2 \tag{2.5}$$

Furthermore, when the A ions are displaced from their nonpolar equilibrium positions, the elastic energy also increases. If the displacement is $\mathbf{u}$, and the force constants k and k', then the increase of the elastic energy per unit volume can be expressed as:

$$W_{elas} = N[(k/2)\mathbf{u}^2 + (k'/4)\mathbf{u}^4] \tag{2.6}$$

Here,$k'(> 0)$ is the higher-order force constant. By rewriting the last equation using:

$$\mathbf{P} = Nq\mathbf{u}, \tag{2.7}$$

where q is the electric charge, the total energy can be expressed as:

$$W_{tot} = W_{dip} + W_{elas} = [(k/2Nq^2) - (N\alpha\gamma^2/9\varepsilon_0^2)]\mathbf{P}^2 + [k'/4N^3q^4]\mathbf{P}^4 \tag{2.8}$$

Thus, if the coefficient of the elastic term is equal to or greater than the coefficient of the dipole-dipole coupling, then $\mathbf{P}$=0; A ions are stable and remain at the non-polar equilibrium positions. Otherwise, a shift from the equilibrium position is stable.

Ferroelectrics are polar materials with at least 2 equilibrium orientations of the permanent polarisation vector in the absence of an external electric field, and in which the spontaneous polarisation vector can be switched between those orientations by an electric field. This is the reason why these crystals can be used in memory storage devices [4]. The external electric field applied to a ferroelectric crystal generates a macroscopic polarisation. The macroscopic bulk polarisation is produced by the displacement of positive charges in an opposite direction to negative charges. At the surface of the crystal there must then be a net charge density of opposite signs on opposite sides of the crystal [9] (Fig. 2.1).

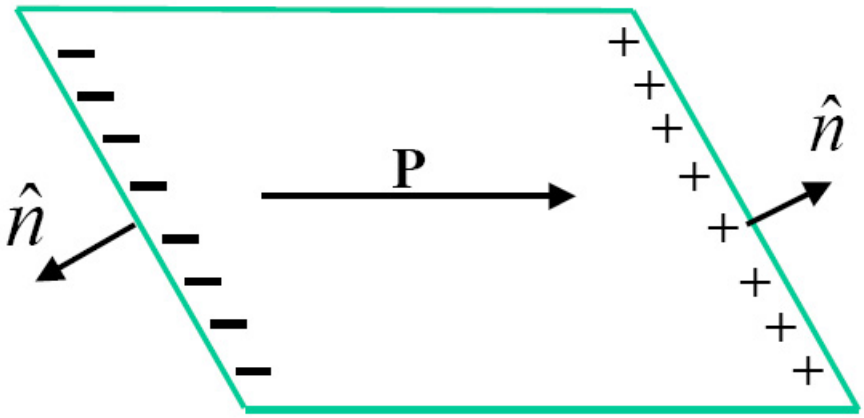

Figure 2.1: Surface charge density generated by a bulk polarisation at an interface (after Kittel, [8]).

When considering the field that acts in an atom, it is not difficult to show that the total electric field acting at the centre of a sphere when all the dipoles are aligned parallel to an axis is: $E = E_0$ for a lattice of cubic symmetry. The local field at an atom is the sum of the external electric field E_0 and the field from the dipoles within the specimen due to other atoms [8]. Figure 2.2 shows the standard method of summing the

dipole fields, which consists on summing over a moderate number of neighbouring atoms inside an imaginary sphere concentric with the reference atom. Taking into account the contributions (shown in figure 2.2) from the external field (E_0), the depolarisation field (E_1) which is the field associated with the outer boundary, the Lorentz cavity field (E_2) which is the field associated with the surface of the spherical cavity, and the field from the dipoles within the specimen (E_3), the local electric field is $E_{local} = E_0 + E_1 + E_2 + E_3$. But this contribution to the local field is the total field at one atom caused by the dipole moments of all the other atoms in the specimen.

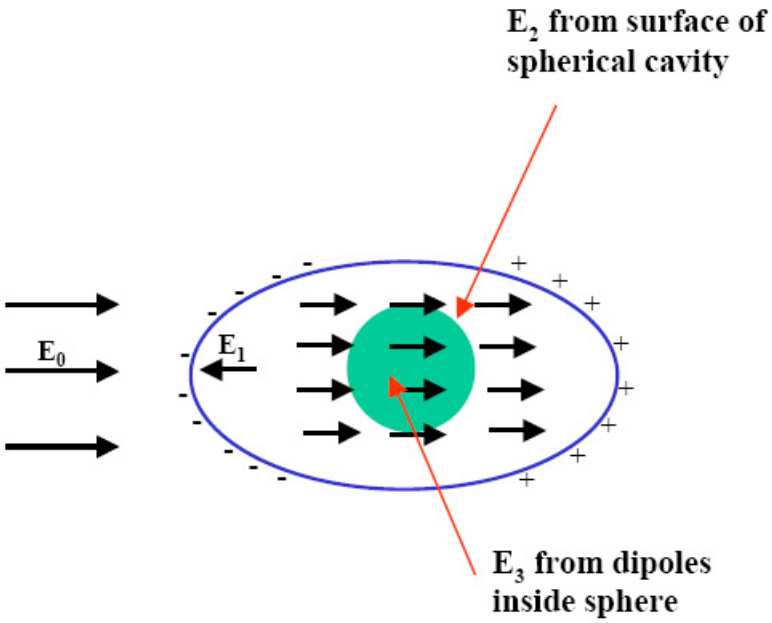

Figure 2.2: Internal electric field on an atom in a crystal (after Kittel et. al., [8]).

2.1.1 Paraelectric-Ferroelectric phase transitions

Many properties of materials can be enhanced when they undergo a phase transition. This is particularly true for ferroelectric and piezoelectric ceramics [4,8]. Phase transitions in which the resulting crystal structure is a distorted form of the pre-transformation crystal structure are called displacive phase transitions [9]. One of the most important

examples of displacive phase transition is the paraelectric-ferroelectric transformation in perovskite ferroelectrics, which includes ferroelectric distortions of the unit cell together with rotations of structural polyhedra. Displacive transitions in such crystals are possible due to their simple perovskite crystal structure. The general formula of the perovskite compounds is ABO_3, where A is a monovalent, divalent or trivalent cation, and B a pentavalent, tetravalent or trivalent cation. Some examples of the most common perovskites compounds are barium titanate ($BaTiO_3$), lead titanate ($PbTiO_3$), potassium niobate ($KNbO_3$) and potassium tantalite ($KTaO_3$), all of which show significant ferroelectric activity [12]. In addition, many of their solid solutions are also ferroelectrics. A widely used example is PZT, a solid solution of lead titanate ($PbTiO_3$) and lead zirconate ($PbZrO_3$). It is a tetragonal structure polarised along $\langle 100 \rangle$ in Ti-rich compositions and a rhombohedral structure polarised along $\langle 111 \rangle$ in Zr-rich compositions [2,13].

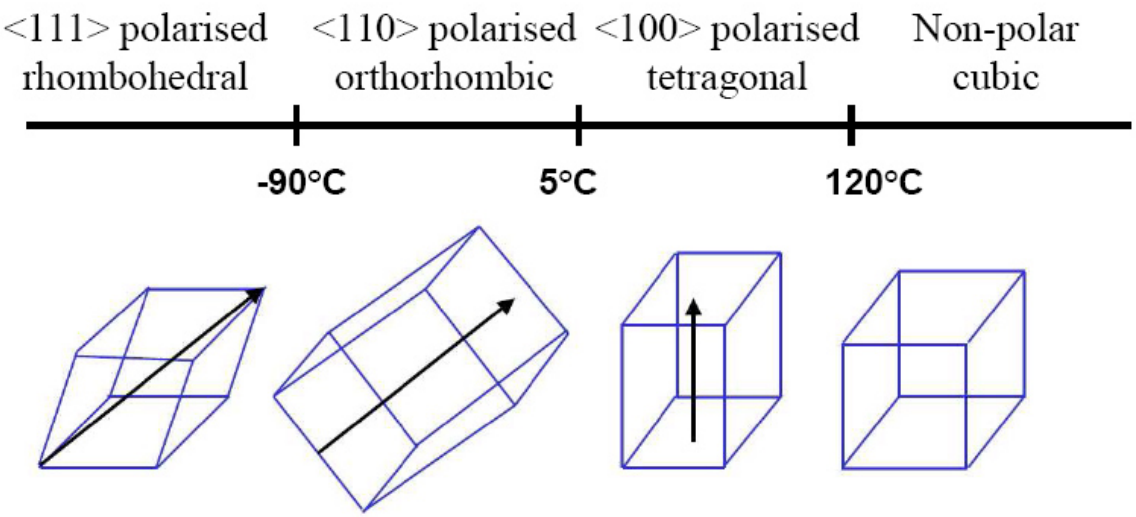

Figure 2.3: Phase transformation in $BaTiO_3$ (after Bhattacharya and Ravichandran et. al., [11]).

The different distortions of the structure during phase transitions in perovskites can be seen in figure 2.3, which shows various crystalline phases of $BaTiO_3$ at different temperatures: cubic and non-polar above its Curie temperature (120°C), $\langle 100 \rangle$ polarised at room temperature, $\langle 110 \rangle$ polarised under 5°C, and $\langle 111 \rangle$ polarised rhombohedral below

-90°C.

2.1.2 Unit cell distortion and domain formation

The transition into a ferroelectric phase usually leads to strong anomalies and anisotropy in many of the properties of the material and is accompanied with a distortion of the unit cell as shown in Figure 2.3. This distortion is associated with the spontaneous polarisation [3]. The spontaneous polarisation in these ceramics is usually not uniformly aligned throughout the whole crystal along the same direction, as it is a statistical phenomenon. In thermal equilibrium the number of atoms with energy E is proportional to $exp(-E/kT)$; so at any finite temperature other orientations will also be present [1]. The regions of the crystal with uniformly oriented spontaneous polarisation are called ferroelectric domains. The reversal of the net macroscopic dipole moment of a ferroelectric crystal occurs through the nucleation and growth of domains that are favourably oriented with respect to the applied electric field [14]. These domains are formed in order to minimise both strain and electrostatic energies caused during the phase transition [1-4].

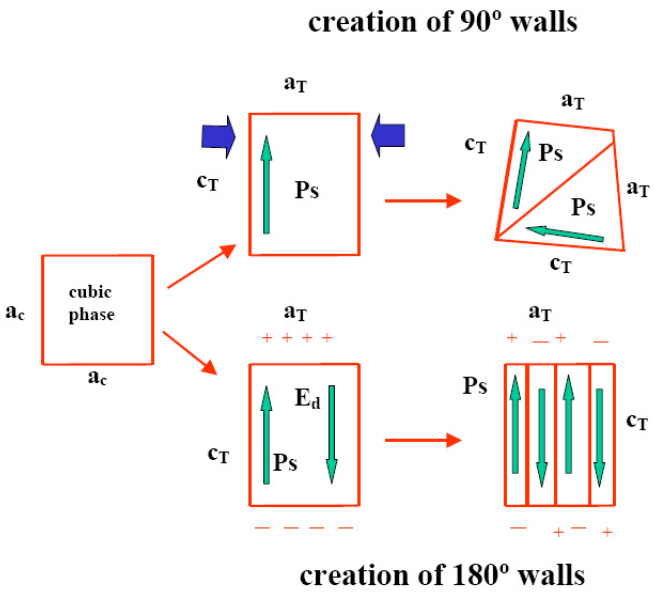

Figure 2.4: Formation of 90° and 180° ferroelectric domain walls in a tetragonal perovskite ferroelectric, such as PZT (after Damjanovic., [3]).

In general, these domains only differ in the direction of polarisation and they are crystallographically classified as twins (in which the structure is mirrored across the boundary plane)[25]. The boundary separating two domains is called the domain wall. Walls, separating the domains with oppositely orientated polarisation, are called 180° domain walls whereas those, which separate regions with mutually perpendicular polarisation, are called 90° domain walls (Figure 2.4). The formation of such domain walls is not arbitrary at all. Thus, domains separating regions of different polarisation must satisfy two conditions of compatibility [14]. The first condition is the mechanical compatibility condition, which ensures the continuity or the coherence of the interface. The second is the electrical compatibility condition, which ensures that no bound charge exists in the domain walls. The 180° and 90° domain walls shown in figure 2.4 are the only two types of boundaries that satisfy these two conditions simultaneously during the phase transition from a cubic paraelectric to a tetragonal ⟨100⟩ polarised ferroelectric [16]. Similar rules can be defined for phase transitions from cubic to ferroelectrics of other symmetries as to the allowed domain walls which result. These have been well reviewed by Fousek and Janovec [26].

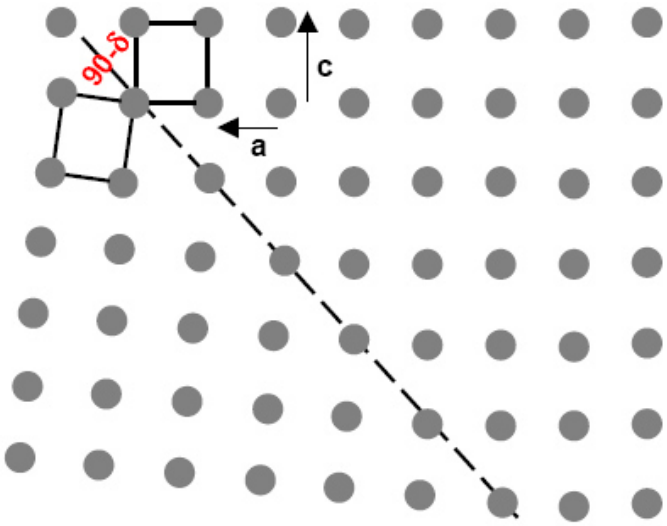

Figure 2.5: [100] Schematic representation of the mismatch in a 90° domain boundary in a tetragonal perovskite (after MacLaren, Schmitt, Fuess, Kungl and Hoffmann., [10])

The 90° domain walls in tetragonal ferroelectrics, separate domains where the polarisation axes are rotated by approximately 90°. In this particular case, as the c_T and a_T axes are different lengths and the angle between polarization directions on each side of a 90° domain wall must be slightly smaller than 90° in order to promote good lattice matching as shown in figure 2.5. Perfect lattice matching between adjacent domains normally results in the formation of lamellar structures of alternating domains as shown in Figure 2.6. This matching can be found only on one given (101) plane in tetragonal ceramics [10].

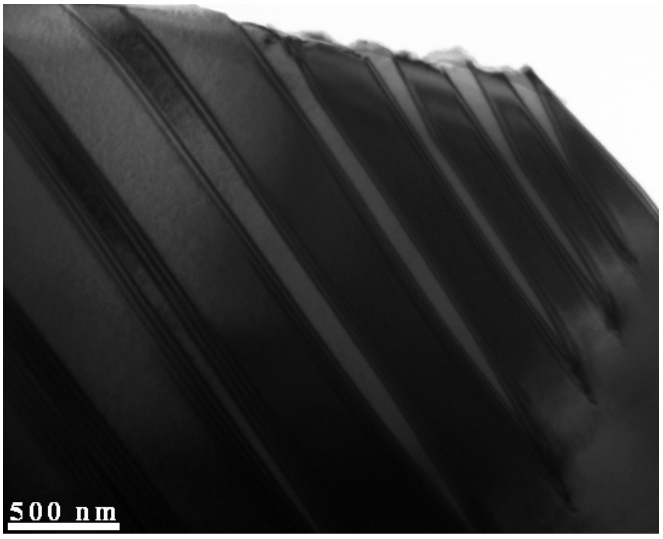

Figure 2.6: TEM image of an undoped PZT 50/50, showing lamellar domain structure where two domains alternate.

2.1.3 Ferroelectricity, pyroelectricity and piezoelectricity

The internal electric dipoles of a ferroelectric ceramic are coupled to the crystal lattice so anything that changes the lattice will change the strength of the dipoles (in other words, a change in the spontaneous polarisation)[1]. The change in the spontaneous polarisation results in a change in the surface charge. Two stimuli that will change the lattice dimensions of a material are force and temperature. Thus, when a crystal is heated or cooled, the internal or external conduction cannot yield enough current to

compensate for the change of the dipole moment, and the crystal acts as an electric dipole. For this reason these crystals are called pyroelectrics [2]. The generation of a surface charge in response to the application of an external stress to a material is called piezoelectricity. Ferroelectric crystals are a subgroup of the piezoelectrics, as the piezoelectrics are a subgroup of the pyroelectrics. In this sense, all ferroelectrics are piezoelectrics and pyroelectrics [5]. Piezoelectricity is one of the most appreciated features of ferroelectric ceramics as many of the recent advances in modern technology are based on this phenomenon. Symmetry plays an important role in determining the piezoelectric effect. The simplest example is the role of a centre of symmetry. As an applied stress cannot remove centre of symmetry in a crystal, it cannot create an electrical polarisation in a centrosymmetric crystal. Thus, the first symmetry condition that must be met for a piezoelectric crystal is that it will not have a centre of symmetry. There are further symmetry conditions on the type of stress that can induce an electrical polarisation [17]. In order to illustrate this phenomenon, as this is a very important property of ferroelectrics, let us suppose we have a positively charged atom surrounded by anions as shown in figure 2.7. If a force is applied on the crystal in the way shown in figure 2.7, the centres of the negative charges and the positive charges no longer coincide. This separation of charges produces a dipole.

Another particular feature of ferroelectric crystals is the outstanding property of the reversibility of the polarisation by an electric field. This reversibility is a consequence of the fact that the polar structure of the ferroelectric materials is a slightly distorted non-polar structure. One of the consequences of domain switching (polarisation reversal) is the existence of a hysteresis loop (figure 2.8). The field is applied along the direction of polarisation. This increases the polarisation reaching P_s called the saturation polarisation. The field is then reduced to zero, so that the polarisation returns to its equilibrium value. The value of polarisation at zero field is called the remenant polarisation (P_r). The field is then increased in the opposite direction. The polarisation is then reduced, instead than immediately switching direction. It is only when the reverse field reaches a certain strength known as the coercive field (E_c) that the polarisation switches directions

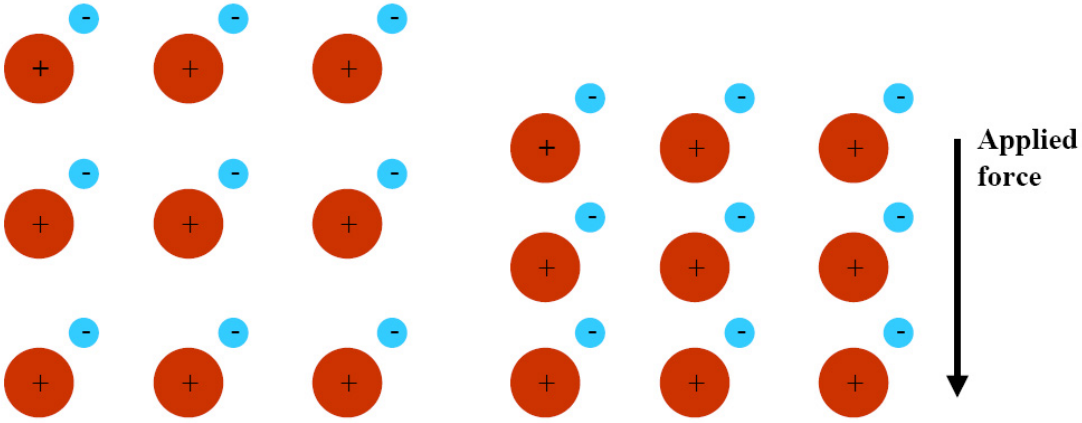

Figure 2.7: Mechanism of the piezoelectric effect in PZT ceramics (after Heywang, Lubitz and Wersing., [17]).

[1].

Many times, after setting the polarisation, the domains are randomly oriented due to different electrostatic and stress processes. When the domain orientation is random neither the pyroelectric nor the piezoelectric effects are present. A remarkable feature of the polycrystalline ferroelectric materials is that they can be polarised by applying an electric field. The reversibility of the permanent polarisation gives rise to a non-linear dielectric behaviour. This polarisation reversal by a field is called *poling* (figure 2.9) [12].

In a ferroelectric, the dipole moments on the atoms in each unit cell align in the same direction. However, there are some polar crystals in which the dipole moments of the atoms in adjacent unit cells point along opposite directions. These are called antiferroelectric crystals [5] and the displacive phase transition associated with this state is called an antiferroelectric phase transition [1]. An antiferroelectric state is defined as one in which lines of ions in the crystal are spontaneously polarised in antiparallel directions to give a net polarisation of zero. In distortions from simple cubic lattices the antiferroelectric state is often likely to be more stable than the ferroelectric state [19]. The antiferroelectric state, contrary to the ferroelectric one, will not be piezoelectric as

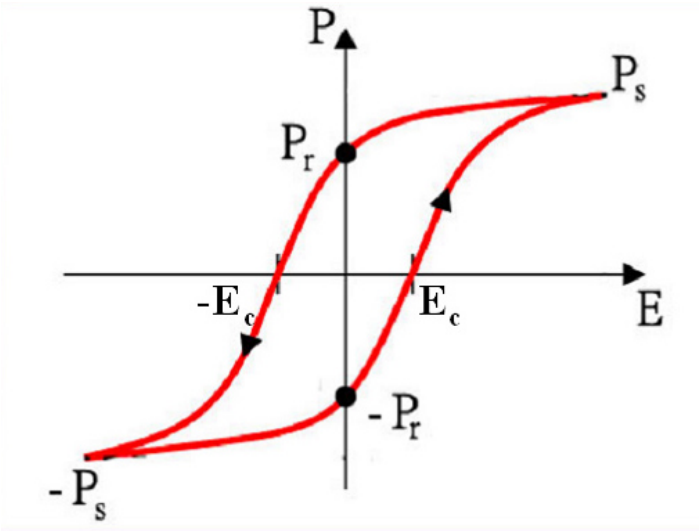

Figure 2.8: Ferroelectric hysteresis loop (after Heywang, Lubitz and Wersing., [17])

a centre of symmetry will exist [1,12]. Figure 2.10 shows the difference between the paraelectric, ferroelectric and antiferroelectric states. It is important to note that such antiparallel dipole ordering will necessarily produce larger unit cells than for the simplest ferroelectric orderings.

2.2 Lead Zirconate Titanate and its Applications

As mentioned before, one of the most exciting and commercially important ferroelectric materials is the PZT ceramic. lead zirconate titanate, $PbZr_xTi_{1-x}O_3$, based piezoelectric ceramics are used in a wide range of applications. There are several directions for ferroelectrics research and development: substrate-film interfaces and high-strain states, finite size effects, nanotubes and nanowires, actuators and sensors, transducers for use at various frequencies up to the extreme ultrasonic regime, electrocaloric devices, ferroelectric random access memories (FeRAMs), dynamic random access memory (DRAM) capacitors, electron emitters, weak-magnetic field sensors, magnetoelectrics, self-assembly, and more [9]. By the moment of writing this thesis the most ambitious technological project for PZT ceramics application is the Terabit ferroelectric memory. This device has not been achieved and the state of the art hard-wired device achieves a storage density of

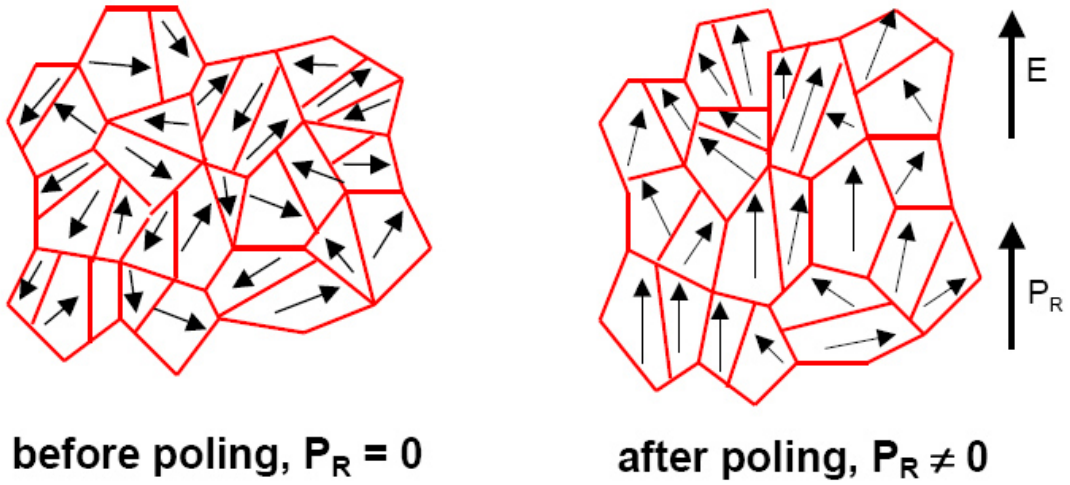

Figure 2.9: Polycrystalline ferroelectric with random orientation of domains before and after the poling (after Damjanovic., [3]).

$0.3Tb/in^2$. Nonetheless, Symetrix and Matsushita Electronics Corporation (MEC) have produced PZT FeRAMs with breakdown fields of 1.5 MV/cm [5]. In spite of the large range of ferroelectric applications for PZT ceramics, the major applications are based on their piezoelectric characteristics. The particular feature that makes PZT ceramics one of the most suitable materials for these applications is the ease of switching, giving PZT ceramics their piezoelectric characteristics. As piezoelectric materials PZT ceramics are used for coupling mechanical and electrical energy in a wide variety of electromechanical devices. The direct piezoelectric effect is more used to generate charge or high voltage in applications such as spark ignition of gas in space heaters [6]. Using the converse effect, small mechanical displacements and vibrations are generated in actuators by applying an electric field. Acoustic and ultrasonic vibrations can be generated by an alternating field applied at the mechanical resonant frequency of a piezoelectric device and can be detected by amplifying the field generated by vibration incident on the material, which is usually applied for ultrasonic transducers [11]. Another important application of PZT piezoelectric features is frequency control. Such applications include: actuators and ultrasonic motors; electronic components such as resonators, wave filters, delay lines; gas

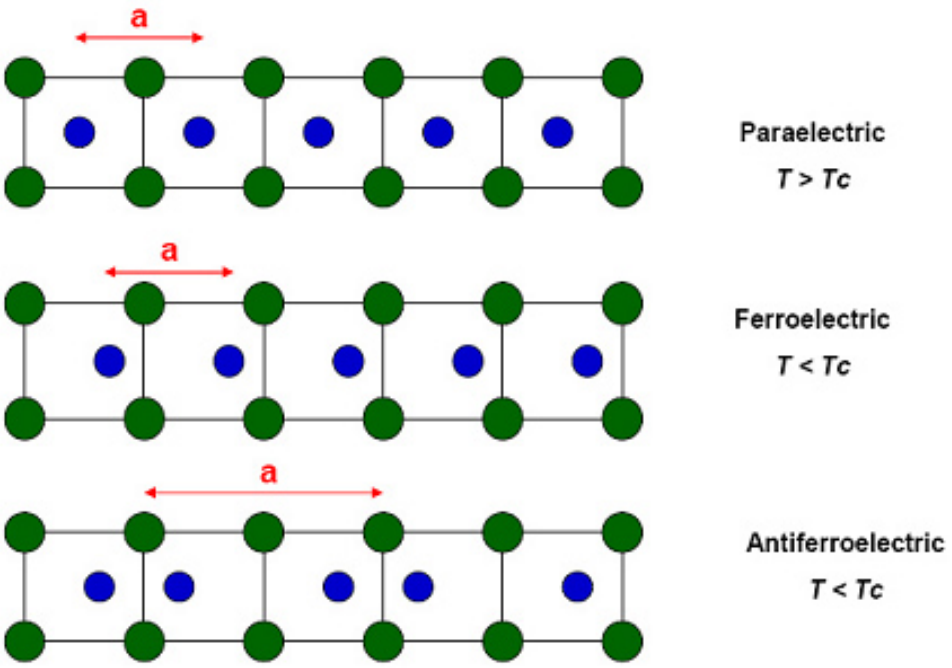

Figure 2.10: Differences between paraelectric, ferroelectric and antiferroelectric states (after Kittel., [8].

igniters, ultrasonic cleaning and machining. Piezoelectric-based sensors like accelerometers, automotive knock sensors, vibration sensors, strain gages, and flow meters have been developed because pressure and vibrations can be directly sensed as electric fields [6,11,18].

2.2.1 Microstructure and crystallographic features

At first sight, the perovskite family seems to be based on a deceptively simple crystal structure. Figure 2.11 shows the ideal perovskite structure. The chemical representation of this perovskites is ABO_3 where A and B are cations. A is on the origin, B cations have fractional coordinates of $\frac{1}{2}, \frac{1}{2}, \frac{1}{2}$, and the oxygen atoms have coordinates $\frac{1}{2}, 0, \frac{1}{2}; 0, \frac{1}{2}, \frac{1}{2}$.

As can be seen in figure 2.11a the B cation is in octahedral coordination with the surrounding oxygen anions, and neighbouring BO_6 octahedra are joined at the corners to form a network that runs throughout the crystal. The A sites have 12 oxygen neighbours as can be seen in figure 2.11b [3]. The most important feature of perovskite structures

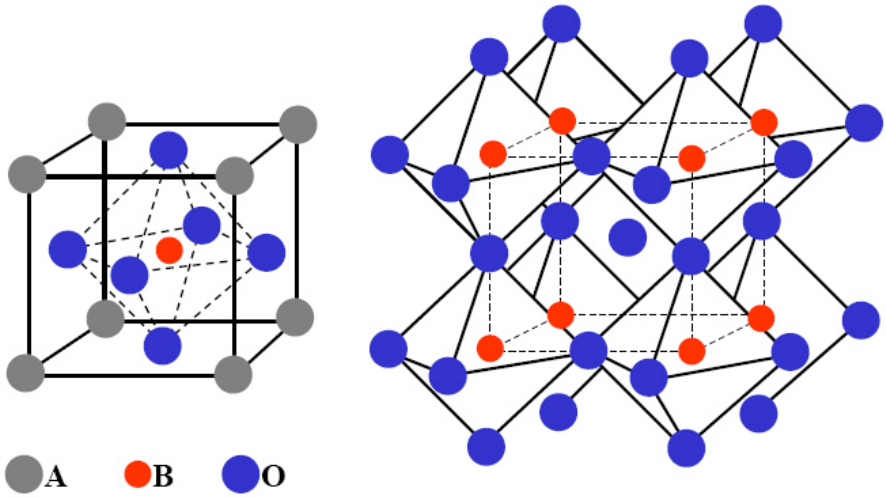

Figure 2.11: a) Ideal perovskite structure with chemical composition, ABO_3 b) as a network of corner-shearing octahedra (after Damjanovic et. al., [3]).

is that they allow many structural phase transitions depending on the details of the chemical composition. The reason why this structure allows many structural phase transitions is that there are several size mismatches between the A and B cations and this size mismatch allows to the unit cell to distort at a structure. The ability of the perovskite to distort is what makes this structure suitable to allow many different pairs of cations, and include mixtures of more than two kinds of them. As a consequence of this flexibility in the structure the perovskites undergo displacive transitions. This kind of transitions implies small displacements of the atoms in such a way that the symmetry in the structure changes. There is no change in bounding or coordination, as in many other phase transformations, but the environment of any atom changes slightly. These displacive transitions will be studied in detail in chapter 5 of this thesis. As mentioned above, the most important phase transition in perovskites (based on their electronic applications) is the ferroelectric phase transition. PZT ceramics are ferroelectric materials with a perovskite structure that undergo several ferroelectric transitions depending on temperature. Figure 2.12 shows the different phase transitions in PZT ceramics and their respective polarisation directions.

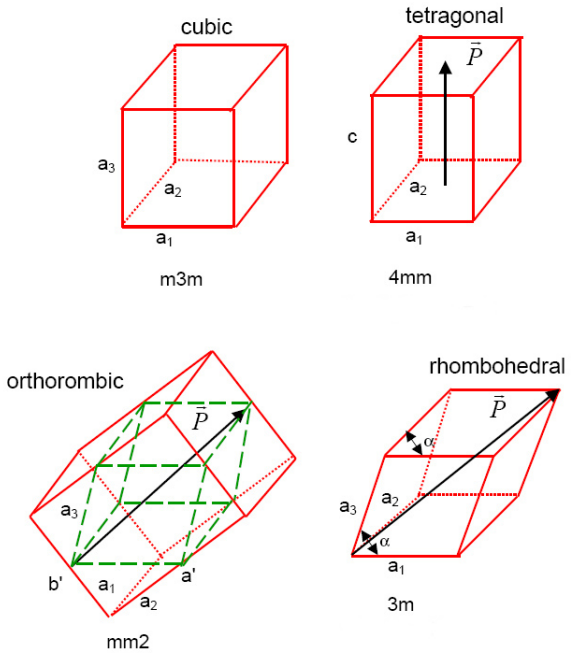

Figure 2.12: Different structure phase transformations and its polarisation directions in PZT ceramics (after Fatuzzo and Merz, [12]).

Note that in the case of PZT ceramics the structure transition below the Curie temperature (around 340°C for a composition of around 52% of Ti) causes a break of the symmetry and the system goes from a centrosymmetric to a non-centrosymmetric state resulting in the appearance of the ferroelectric state [12]. This phenomenon coupled with the electric polarisation leads to the piezoelectric effect where an electrical polarisation is induced by the application of an elastic stress. Thus, we can say that the technological relevance of these piezoelectric ceramics lies in the susceptibility of the perovskite structure to such structural phase transitions. Since such phase transformations result in the formation of nanoscale domain structures, the macroscopic properties of PZT ceramics are critically dependent on the nanostructure. In the previous sections it was mentioned that PZT ceramics are the most important and applied piezoelectric material. When cooling below Curie temperature, the perovskite structure of the PZT suffers a displacive phase transformation and atomic displacements. For Ti-rich PZT the point symmetry

changes from cubic $m3m$ to tetragonal $4mm$ at Curie temperature with a large resulting static polarisation, which can be very difficult to switch. But in order to maximise the switchable polarisation of the PZT phase, compositions around the boundary between the stable compositions for the tetragonal and the rhombohedral forms are chosen. At the Curie point the ideal cubic paraelectric PZT transforms to a ferroelectric phase near the morphotropic phase boundary (MPB) between the rhombohedral and tetragonal phase, as shown in figure 2.13. Very large piezoelectric coupling between electric and mechanical variables is attained near the MPB and a maximum value of switchable polarisation is achieved.

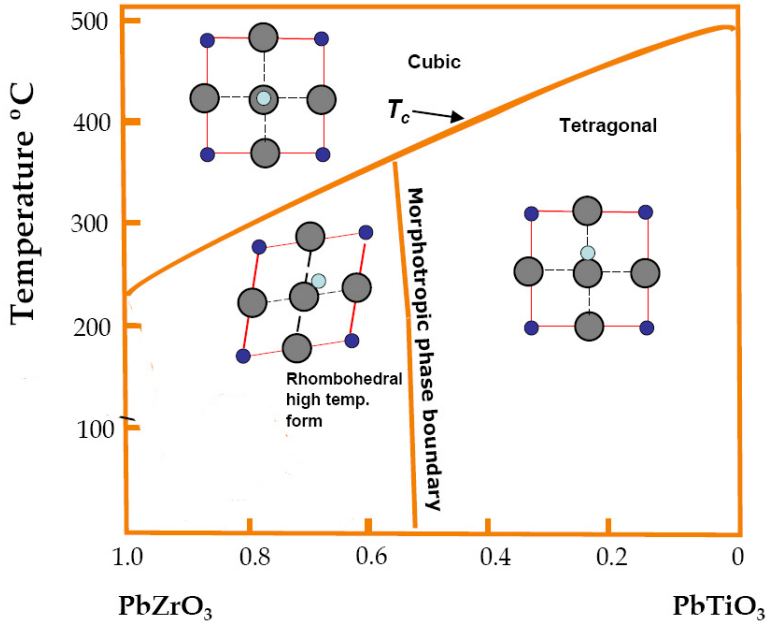

Figure 2.13: Phase diagram and associated structural changes at the Curie temperature and the MPB (after Jona and Shirane, [2]).

2.2.2 Doped and undoped PZT

Besides the physical properties of the undoped PZT commented so far, an important number of variations in such properties can be achieved by doping with different elements. Dopants are always added to PZT in commercial applications, especially to

enhance the piezoelectric response and to modify the microstructure [22]. The techniques for modifying piezoelectric ceramics include element substitution and doping. In general, the term "element substitution" implies that cations in the perovskite lattice, for example, $Pb^{2+}, Zr^{4+},$ and Ti^{4+}, are replaced partially by other cations that have the same chemical valence and ionic radii similar to those of the replaced ions. The new substituent cation usually occupies the same position as the replaced cation in the perovskite lattice, and thus a substitutional solid solution is formed; the term "doping" implies that some ions whose chemical valences differ from those of the original ions in the lattice, are added to PZT ceramics. There are two main types of dopants: donor dopants and acceptor dopants. Donor dopants cause Pb-vacancies by substituting a higher valence ion for Pb^{2+} or for $(Ti, Zr)^{4+}$ [6]. Examples of donor dopants are $Nb^{5+}, Ta^{5+}, La^{3+}, W^{6+}, Th^{4+}, B^{3+} and Sb^{5+}$. Acceptor dopants cause O-vacancies by substituting a lower valence ion for Pb^{2+} or for (Ti, Zr)$^{4+}$. Examples of acceptor dopants are $Sc^{3+}, Mg^{2+}, K^{+} or Fe^{3+}$ [24]. Examples of the changes in properties are the drastically increased of P_r and P_{sat} values in PZT when doped with 1.5 mol% of PYN [23]. These changes in properties and microstructure result in changes in direct applications of PZT ceramics. In particular the fatigue behaviour of PZT, which is a critical problem in applications for FRAM devices, has been extensively studied. To overcome the switching fatigue problem in PZT ceramics, different dopants have been proposed. Some of the most studied and more suitable dopants are LaNb and Sb [24]. Zinc doping into PZT tends to decrease the remnant polarization in a manner similar to lanthanum doping of PZT. An examination of the ionic radii and defect chemistry of the system implies that, zinc substitutes into the B-site of the ABO_3, perovskite lattice [21].

Bibliography

[1] Solymar, L., Walsh, D., Electrical properties of materials, Oxford University, Oxford, UK, (2003).

[2] Jona, F., Shirane, G., Ferroelectric Crystals, Monographs on Solid State Physics, Pergamon Press, Germany, (1962).

[3] Damjanovic, D., Rep. Prog. Phys. 61, 1267-1324, (1998).

[4] Dove, M.T., Structure and Dynamics: An atomic view of materials, Oxford University Press. Oxford, UK, (2003).

[5] Scott, J.F., Science. 315, 954-959, (2007).

[6] Schwarts M., Smart Materials Vol. 2, John Wiley & Son. New York.

[7] Valasek, J., Physical Review 15: 537, (1920).

[8] Kittel, C., 8th edition Introduction to Solid State Physics, John Wiley & Son. New York, (2005).

[9] Rabe, K., Ahn, Ch. H., Triscone J.-M.(Eds.) Physics of Ferroelectrics, A Modern Perspective, Springer, (2007).

[10] MacLaren, I., Schmitt, L.A., Fuess, H., Kungl, H., and Hoffmann, M.J., J. Appl. Phys., 97, 094102 (2005).

[11] Bhattacharya, K., and Ravichandran, G., Acta Materialia, 51, 5941-5960, (2003).

[12] Fatuzzo, E,. and Merz, W.J., Ferroelectricity. Amsterdam: North-Holland, (1967).

[13] Holt, M., Hassani, Kh., and Sutton, M., Phys. Rev. Lett. 95, 085504, (2005).

[14] Burcsu, E., Ravichandran, G., and Bhattacharya, K., Appl. Phys. Lett. 77, 1698, (2000).

[15] Rogan, R.C., Tamura, N., Swift, G.A., and Ustundag, E., Nat. Mater. 2, 379, (2003).

[16] Shu, Y.C., and Bhattacharya, K., Phil. Mag. B. 81, 2021-2054, (2001).

[17] Heywang, W., Lubitz, K., and Wersing, W., (2008) Piezoelectricity, Springer. Germany.

[18] Ahn, C.H., Rabe, K.M., and Triscone, J.-M., Science. 303, 488-491, (2004).

[19] Kittel, C., Physical Review 82: 5, (1951).

[20] Won-Youl Choi, Joon-Hyung Ahn, Won-Jae Lee, and Ho-Gi Kim, Mater. Lett. 37, 119-127, (1998).

[21] Melnick, B.M., Scott, M.C., Paz de Araujo, C.A., and McMillan, L.D., Integrated Ferroelectrics, 3, 293-300, (1993).

[22] Tan, Q., Xu, Z., Viehland, D., Phil. Mag. B 80, 1585, (2000).

[23] Qiu, W., and Hng, H.H., Materials Chemestry and Physics, 75, 151-156, (2002).

[24] Choi, W.Y., Materials Mater. Lett., 37, 119-127, (1998).

[25] Hammond, C., The basics of Crystallography and Diffraction, Oxford University Press, UK, (1993).

[26] Fousek, J., and Janovec, C., J. Appl. Phys. 40, 135 (1969).

[27] Uchino, K, Ferroelectric Devices, Marcel Dekker, Inc., New York U.S.A., (2000).

Chapter 3

Experimental and analysis methods

A complete nanostructural characterisation requires the revision of the fabrication methods used in the materials, as well as the processing and analysis methods available for characterisation. The ceramic preparation method depends on the application of such a ceramic. In ceramics with electro-optics applications, the homogeneity and purity are more important factors than in the case of ceramics for piezoelectric applications. This is because the impurities are more easily detected optically than electrically. To choose the correct method of fabrication and preparation of the samples is essential for successful characterisation. The characterisation of PZT ceramics in this thesis was carried out by electron microscopy techniques. Thus, a brief revision of the basics of the techniques applied is necessary in order to justify their use. In this chapter, the methods available for ceramic fabrication and the principles of sample preparation for transmission electron microscopy (TEM) and electron backscatter diffraction (EBSD) characterisation are reviewed. In order to achieve a clear idea of the procedure followed for microscopy data analysis in this thesis, a revision of the principles of such method is presented as well. Section 3.1 is a revision of the methods used in ceramic preparation and states the route followed for the fabrications of the samples used in this work. Section 3.2 is a revision of the sample preparation routes followed for TEM and EBSD characterisation in the two different PZT compositions analysed in this work. This section shows as well the importance and problems of sample preparation. Section 3.3 describes the principles of

misorientation in crystals in order to describe the concepts used in the analysis of microscopy. Section 3.3.1 explains the procedure followed to describe mathematically the misorientation between crystals and justifies the method chosen for such a description in this thesis. Section 3.4 deals with the principles of the diffraction methods used in this thesis and introduces the analysis technique used to calculate misorientations. Section 3.5 describes the basics of imaging acquisition in TEM and the crystallographic information obtained in electron microscopy. Finally, section 3.6 gives some examples of the different microscopy techniques applied to to study ceramics.

3.1 Ceramic preparation

For piezoelectric applications the usual method of preparation is the traditional mixed oxide/carbonate method [42]. Together with the composition and powder preparation, densification is a main factor for obtaining pore free ceramics. Figure 3.1 shows a general scheme of the traditional methods applied in ceramics preparation. The sintering process is an older technique than the hot-pressing one, but has limitations for obtaining total densification in some cases. Nonetheless, there exist alternative methods to improve this technique and obtain the desired densities. The most popular of these is the use of an oxygen atmosphere during firing, which is used in ceramics containing lead (PZT and PLZT) [43].

Another alternative is the hot-pressing process, which allows very high density ceramics to be achieved; thus, it is applied in transparent ceramics preparation with very good results. Generally, PZT solid solutions are synthesised by solid-state reaction of the corresponding oxides (mixed-oxide route) or by calcining of sol-gel derived precursors. In both cases the reaction kinetics of the solid solution formation, the sintering behaviour, and the grain growth are controlled by the different diffusion coefficients of Pb, Ti, Zr, and the modifier (additives). Detailed studies of the reaction sequence for the mixed-oxide route during calcination show lead titanate as the first reaction product before the PZT solid solution is formed [44].

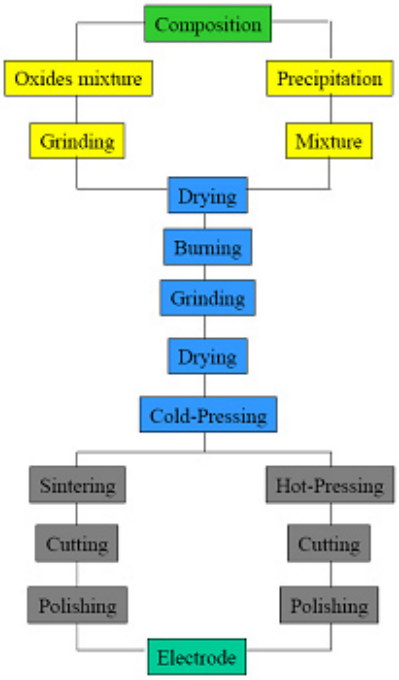

Figure 3.1: General scheme explaining the modern electro-ceramics preparation process (after Suarez-Gomez, [43])

Complete densification of doped PZT ceramics can be achieved by pressureless sintering in oxygen at temperatures between 1100°C and 1300°C. The most critical factor during sintering is the control of PbO vapour pressure to avoid PbO weight loss and a change in composition [45]. The PbO excess leads to the formation of a liquid phase, and consequently, to an enhanced densification rate during the initial and intermediate stages of sintering [46]. Since sintered ceramics with PbO excess can exhibit PbO-rich grain boundaries, careful control of the sintering atmosphere is necessary. Another important parameter for densification and microstructural development is the influence of the additives (dopants)[43]. For the experiments shown in this work, two different PZT ceramic samples were prepared. The first kind, the undoped PZT ($PbZr_xTi_{1-x}O_3$) with nominal compositions of x=*0.5* were prepared by the conventional mixed-oxide process with 3 mol% PbO excess. The oxides were homogenised for 3 h by attrition milling using isopropyl alcohol as milling media. After drying in a rotary evaporator, the powder mixtures were calcined in air at 850°C and 875°C, respectively, for 2 h. The dried

powders were afterwards consolidated into green compacts of 15 mm thickness and 10 mm diameter by using rubber molds and cold isostatic pressing at 630 MPa. Complete ($PbZr_xTi_{1-x}O_3$) with nominal composition of x =50% solid solution formation after calcination was confirmed by X-ray diffraction [44]. The second kind of samples prepared was the Lanthanum doped PZT with the composition $Pb_{1-3x/2}La_x\Delta^A_{x/2}(Zr_{0.9}Ti_{0.1})_{1-5x/4}O_3$, being x the doping level of La (mol%), and taking into account the generation of vacancies ($\triangle$) on the A site of the perovskite structure. The procedure for making these samples was the same than the one used in the undoped PZT with just two main differences: Three different compounds were used, x = 2, 3 and 4 mol%, and we refer to this compound as PLZT x/90/10. Powders were fired at 950°C for 90 min after mixed and milled for 120 min. Then, PVA binder was added and green compacts were formed at a constant pressure of 150 MPa. Sintering was achieved at 1250°C for 120 min and cylindrical samples were then cut into thin disks, plated and poled near saturation at 4 kV/mm [23,24].

3.2 Specimen preparation for microscopy

Sample preparation is roughly speaking a non-straightforward step in electron microscopy characterisation; but it is a determinant and difficult issue for ceramics characterisation due to their physical properties. Ceramic samples typically have a high electrical resistivity and, in the absence of a conductive coating, can quickly acquire a charge under the electron beam. In the case of TEM characterisation, this charge can cause a large enough electric potential to produce a dielectric breakdown in some parts of the specimen and variations in the surface potential. This results in astigmatism, image instabilities and disproportionate brightness [9]. Furthermore, physical damage of the sample due to charge can be experienced, as well as changes in the morphology and structure of the domain boundaries due to domain boundaries movement induced by the electron beam [47]. One solution to this problem is to coat the specimen with a conductive material such as carbon. However, there are several issues surrounding the coating process. One

of the principal problems is that the coating adds an extra layer of unwanted material to the ceramic, as the carbon coating must be deposited in relatively thick layers [33]. The stability of the domain pattern in PZT is strongly dependent on several factors including the nature of the conductive coating, the electron-beam intensity, and the location of the beam on the sample [47]. In the case of EBSD, as has been mentioned in this thesis, the misorientation determination of two grains is obtained from the local crystallographic orientation of each grain from the analysis of local EBSD Kikuchi patterns. In practice, this determined orientation has an uncertainty, which is controlled by the clarity of the EBSD patterns. If the surface layers of the ceramic are damaged, the coating invariably becomes more than an obstacle to obtain patterns and causes misindexing problems in the EBSP, as the signal for the image comes from a depth of up to half the penetration depth [48]. In addition, rough surfaces can trap the incident electrons and cause charging effects, which may blur the patterns. Therefore, special final polishing or damage-removal techniques like colloidal silica polishing are needed in order to obtain a surface free from damage. The electric fields resulting from the surface charging can be sufficiently high to induce phase changes or domain migration. Room temperature observations of carbon-coated samples showed little evidence for beam-induced domain migration or specimen charging. The specimen preparation objective for EBSD can be stated very simply: the top 10-50 nm of the specimen must be representative of the region from which crystallographic information is achieved, since it is from this region that the diffraction information is acquired. Thus, the only crucial aspect of sample preparation for EBSD is that the specimen surface must not be obstructed in any way by mechanical damage, surface layers, or contamination [43,47]. Besides all the methods of polishing there is a very effective technique based on gentle ion beam milling (2kV and 3.5 mA argon, for 10 minutes) [35]. With this technique the effects of rough surfaces can be overcome and the electron backscatter diffraction pattern (EBSP) obtained are clearer at least for some materials. In the case of PZT ceramics, the summarized route for EBSD sample preparation could be: grinding, polishing, and coating. Nonetheless, for the samples presented in this work we added a light-etching prior the coating.

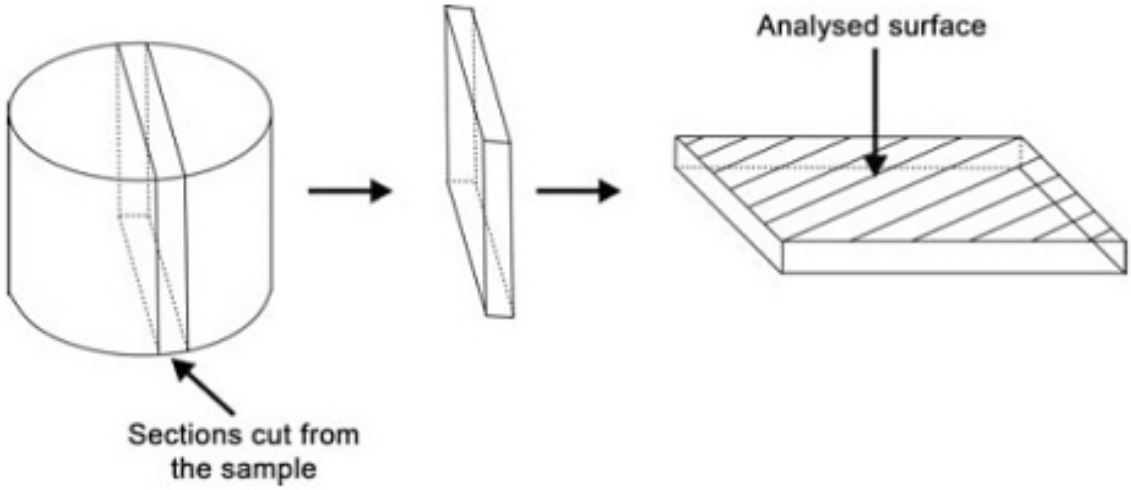

Figure 3.2: Sample sectioning process for EBSD and TEM analysis

The samples studied in this work were prepared for microstructural investigation as shown in figure 3.2, by sectioning the pieces vertically. The samples were received as-sintered state, in a cylinder shape with diameter of 9 mm. For TEM analysis the starting material was also the rectangular section shown in figure 3.2. Four smaller disks of 3 mm in diameter were cut out from each slice. These were then ground to about 150 μm and then dimpled to a thickness of 20 μm in the centre. The samples were ion milled in a Gatan PIPS (Gatan Inc., Pleasanton, CA) using 4 kV Ar+ ions and a 4° incident angle from top and bottom, and finally coated with a thin film of carbon to minimise charging. The thickness of sections cut for EBSD analysis was 2 mm, and ground on 1000 grit silicon carbide papers and polished using 6, 3 and 1 μm diamond paste, followed by a final polish with colloidal silica to remove strains and provide a high quality surface finish. A light etch of 100 ml H_2O, 5 ml HCl and five drops HF was applied for 11 seconds to reveal a slight amount of domain topography and finally, a thin coat of carbon was evaporated onto the sample to minimise charging [40].

3.3 Misorientation in crystals

The physical properties of polycrystals usually differ from those of single crystals with the same chemical composition and structure. There are too many factors inherent in a polycrystalline material that do not exist in single crystals, which relate specific properties of the bulk material to the relationship between crystal pairs [1]. In fact, a significant amount of research on polycrystalline materials is concerned with the accurate determination of orientation relationships between adjacent crystals. There are many practical applications, as in the study of anisotropy and texture as well as in various mechanical property assessments. Needless to say, the properties of interfaces depend critically on the relative orientations of the crystals that they connect [4], as well as the interface plane.

In order to analyse the physical properties in polycrystalline materials it is necessary to describe the relation between pairs of grains. One factor that allow us to describe the relationship between two neighbouring crystals is the misorientation. The misorientation is a re-expression of the orientation of two neighbouring crystals in terms of the relative orientation between them [2]; in other words, the non-coincidence between two lattices of a bicrystal. How the orientations of crystals residing in the same polycrystal are related, is defined by the geometry of the system (bicrystal). The term geometry is used to denote crystallographic parameters. Figure 3.3 represents a bicrystal illustrating the two orthogonal coordinate systems of the two crystals taken with the same origin and two unit vectors which are: the total rotation axis $\vec{u}$, and the grain boundary normal $\vec{n}$.

As seen in figure 3.3, the two crystal lattices are not coincident, but one lattice is misoriented (rotated) by a certain amount with respect to the other and vice versa. An axis of misorientation/angle of misorientation pair is commonly used to describe the relationship between two grains; briefly, the misorientation axis is a direction common to both grains around which one of the grains must be rotated by the angle of misorientation, in order to achieve the orientation of the other grain[3]. In order to rotate a crystal relative to a fixed system, it is necessary to define the axes around which the rotation of an angle

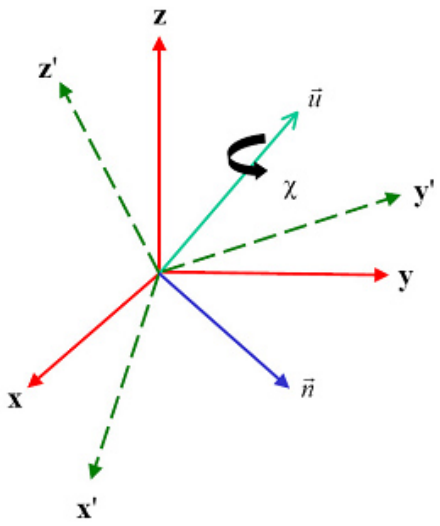

Figure 3.3: The two orthogonal coordinate systems of a bicrystal, one being rotated around the rotation axis$\vec{u}$ by an angle χ. $\vec{n}$ is the grain boundary normal for the bicrystal. (after Lange, [1])

will result in the alignment of this crystal with the reference system. In the case of a bicrystal the reference system is the set of aeis of the first crystal, while the axes of the second crystal are aligned with those of the first one by a rotation through the angle of misorientation, about the axis of misorientation [uvw] [2]. Figure 3.4 shows in a graphic way, the angle/axis of misorientation concept.

If crystal 1 from figure 3.4 is chosen as to be the reference crystal in the system, then the crystal axes of grain 2 must be referred to the coordinate system of the crystal 1 in order to rotate from $[u, v, w]_2$ to $[u, v, w]_1$. A 3x3 matrix whose columns represent the direction cosines of crystal 2 referred to crystal 1 can calculate the rotation necessary to transform the crystal axes of crystal 2 onto crystal 1 [6].

$$g = \begin{bmatrix} g_{11} & g_{12} & g_{13} \\ g_{21} & g_{22} & g_{23} \\ g_{31} & g_{32} & g_{33} \end{bmatrix} \tag{3.1}$$

The matrix in equation 3.1 is called the rotation matrix and is an alternative representation of a misorientation. Both, the rows and the columns of the matrix are unit vectors;

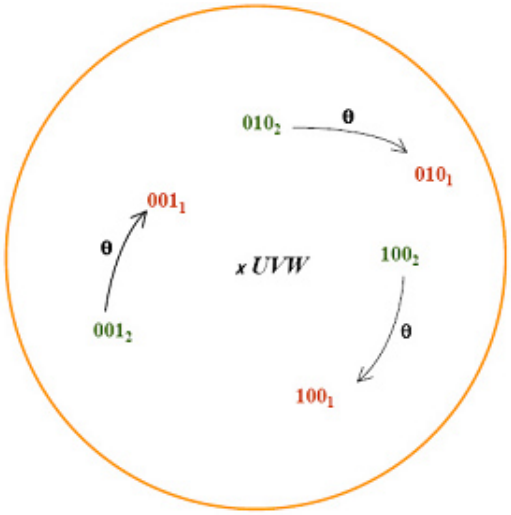

Figure 3.4: Stereographic projection representation showing angle/axis misorientation. The crystal axes of grain 1 by a rotation θ through UVW (after Randle, [3]).

thus, the matrix is orthonormal and the inverse of the matrix is equal to its transpose. It is clear that the matrix has non-independent elements, as it has nine numbers and a misorientation just needs three independent variables to be fully specified [3]. Thus, if we know the coordinate system (C_1) of crystal 1, we can obtain the coordinate system of crystal 2 (C_2) from multiplying it by the misorientation matrix composed by and UVW as follows [12]:

$$C_2 = gC_1 \tag{3.2}$$

Due to the properties mentioned above, the rotation matrix is a suitable mathematical tool to describe the misorientation for any of the different orientation descriptors. Since only three independent variables are needed to fully specify an orientation, the most suitable method of expressing these three numbers is the three Euler angles descriptor. The Euler angle description describes orientations conveniently in three parameters and is described in the following section.

3.3.1 Euler angles

The complete orientation of a crystal in a polycrystalline material must be specified by three Euler angles [8], which are defined as follows. It is assumed that the crystal frame of reference is parallel to the specimen coordinate system. It is then rotated successively through three rotations φ_1 about the [001] z axis, Φ about the new [100] x axis and φ_2 about the new [001] z axis [10]; φ_1, Φ, φ_2 are the Euler angles. The Euler angles essentially describe the orientation of a crystal rather than a plane, and hence require a three dimensional representation [11,12]. Usually, the angular parameters are plotted as Cartesian coordinates. There is more than one convention for expressing the Euler angles, the most commonly used is the one formulated by Bunge [2] shown in figure 3.5, as defined above and used in this work.

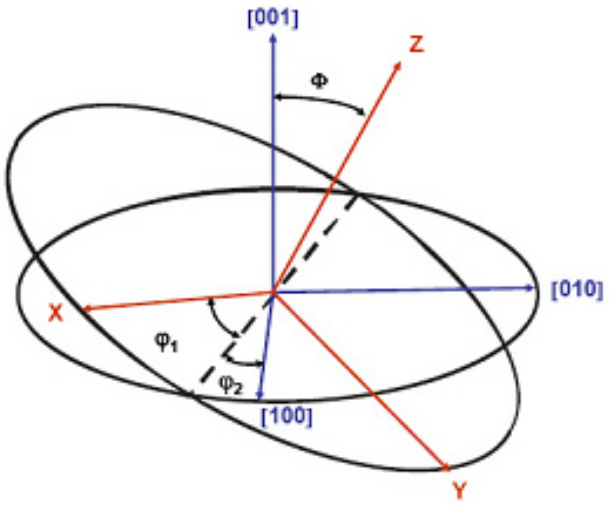

Figure 3.5: Definition of Euler angles that describe the rotation between two sets of axes XYZ and 001, 010, 001. (after Randle, [3])

Each point in Euler space represents a crystal orientation. The three dimensional orientation distribution functions gives the relative frequency of crystals having the orientation described by the Euler angles, measured in multiples of the random distribution. Analytically, the three rotations are expressed as[7]

$$g_{\varphi_1} = \begin{bmatrix} \cos\varphi_1 & \sin\varphi_1 & 0 \\ -\sin\varphi_1 & \cos\varphi_1 & 0 \\ 0 & 0 & 1 \end{bmatrix} \tag{3.3}$$

$$g_{\Phi} = \begin{bmatrix} 1 & 0 & 0 \\ 0 & \cos\Phi & \sin\Phi \\ 0 & -\sin\Phi & \cos\Phi \end{bmatrix} \tag{3.4}$$

$$g_{\varphi_2} = \begin{bmatrix} \cos\varphi_2 & \sin\varphi_2 & 0 \\ -\sin\varphi_2 & \cos\varphi_2 & 0 \\ 0 & 0 & 1 \end{bmatrix} \tag{3.5}$$

By multiplication of these three matrices in order, an expression is obtained which links the rotation matrix to the Euler angles

$$g = g_{\varphi_2} g_{\Phi} g_{\varphi_1} \tag{3.6}$$

Thus, the matrix in terms of the Euler angles is given by[11]:

$$g = \begin{bmatrix} \cos\varphi_1\cos\varphi_2 - \sin\varphi_1\sin\varphi_2\cos\Phi & \sin\varphi_1\cos\varphi_2 + \cos\varphi_1\sin\varphi_2\cos\Phi & \sin\varphi_2\sin\Phi \\ -\cos\varphi_1\sin\varphi_2 - \sin\varphi_1\cos\varphi_2\cos\Phi & -\sin\varphi_1\sin\varphi_2 + \cos\varphi_1\cos\varphi_2\cos\Phi & \cos\varphi_2\sin\Phi \\ \sin\varphi_1\sin\Phi & -\cos\varphi_1\sin\Phi & \cos\Phi \end{bmatrix} \tag{3.7}$$

From figure 3.3 it is easy to recognise the domain of Euler angles as being $0° \leq \varphi_1, \varphi_2 \leq 360°$ and $0° \leq \Phi \leq 180°$. It is easy to see as well that the sine and cosine functions in equation 3.7 are defined only in the range of $-90° \leq \varphi_1, \varphi_2 \leq 90°$. Hence, determination of Euler angles from equation 3.7 is not straightforward since the range of the angles has to be considered too. The correct value has to be decided by taking the information in other matrix elements into account [7].

3.4 Diffraction information

In order to determine the structure of crystals we need to use, inevitably, beams of radiation. The requirement is that the wavelength of the radiation will need to be smaller than typical interatomic distances if there is to be adequate resolution in the reconstructed image of the atoms in the crystal [51]. Structure determination for crystals is currently performed with the use of x-ray and neutron diffraction, which average over many identical cells by focusing beams into directions defined by the crystal's reciprocal lattice[50]. Nonetheless, electron diffraction is one of the major electron microscopy techniques and has been used for phase identification, structure and symmetry determination, foil thickness measurement, lattice parameter measurement, disorder and defect identification [52]. Recent development has significantly improved the quantitative analysis of electron diffraction intensities and has brought new types of highly accurate electron diffraction techniques for structure refinement and structure factor measurement. The recent development in the new generation of field-emission electron microscopes and energy-filter promise further development in single atomic column scattering and diffraction from nanometer-sized molecules, clusters, wires and other low-dimensional objects[52,53]. Hence, local internal structures are imaged with the use of transmission electron microscopes as resolution of $\sim 1\mathring{A}$ for crystalline samples is possible with recent developments in microscopy [54-57]. The interaction between the incoming fast electrons in the beam and an atomic nucleus in the sample gives rise to elastic scattering where almost no energy is transferred. The interaction between the fast electrons and atomic electrons, results in inelastic scattering, where the transmitted electron can lose an appreciable amount of energy [48]. Diffraction is the elastic scattering of electrons (deflection by the Coulomb field of atomic nuclei) in a crystalline material [23]. Depending on the acceleration voltage, the electrons emitted from a cathode are typically accelerated to energies from about 1 keV up to 400 keV. These electrons are gathered and focused by electromagnetic lenses to form the incident beam that is directed onto the specimen. All this happens in a low pressure or high vacuum chamber to avoid electron interaction with

the surrounding gases and the chemical reaction (poisoning) of the filament with traces of oxygen [49]. The transmission electron microscope (TEM) uses the transmitted electrons while the scanning electron microscope (SEM) detects the electrons emitted into the half space of the incident beam [18] (figure 3.6). Since the electrons can be regarded as waves, they can be diffracted by crystal lattices. When electrons interact with matter, we expect them to interact (via Coulomb interactions) with the negatively charged electron clouds, as well as the positively charged nuclei of the atoms.

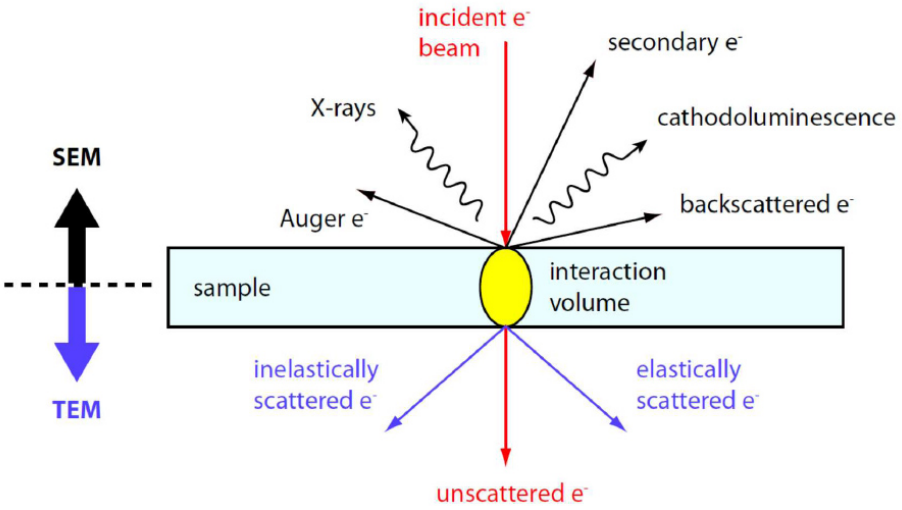

Figure 3.6: Signals generated when a high-energy beam interacts with a thin specimen. (after Williams and Carter, [18])

The interaction of electrons with matter is, therefore, stronger than the interaction of X-ray with matter [19]. As electrons interact very strongly and are very sensitive to matter's valence electrons or bonding electrons [20], diffraction with electrons is a very powerful tool in the structure and chemical analysis of matter. In order to extract all the crystallographic information of a specimen, different electron diffraction techniques are employed in diffraction analysis. In the next section a revision of the electron diffraction techniques used in this thesis is made.

3.4.1 Diffraction in TEM

A transmission electron microscope (TEM) consists of a source of electrons (the electron gun) and a series of electromagnetic lenses, as shown in figure 3.7. The most critical components of a magnetic lens are the soft-iron pole-pieces, which produce an axially symmetric magnetic field for focusing the electrons. The rest of the lens is a magnetic yoke containing the windings for energising the lens with a d.c. current, the magnetic field, and hence the focal length of the first lens is changed [16].

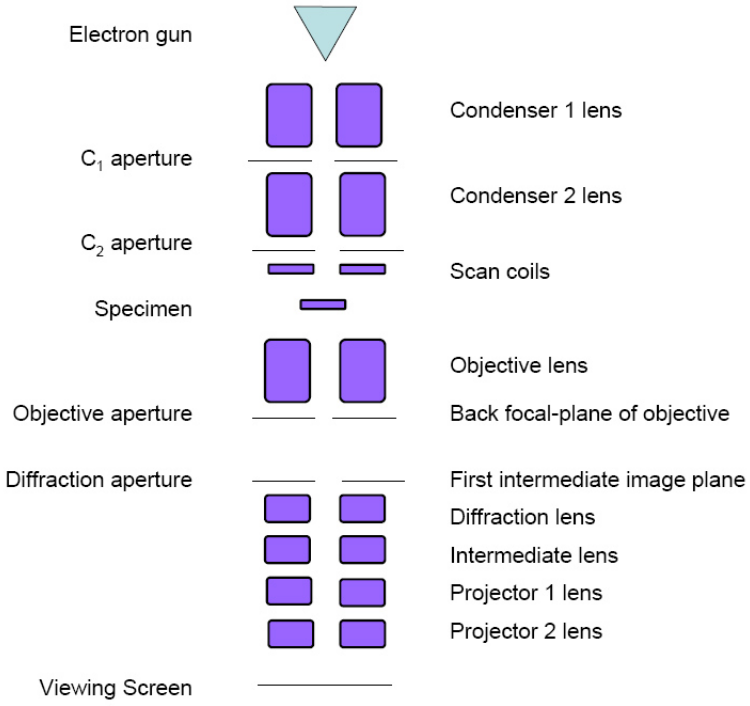

Figure 3.7: Schematic diagram of the lenses and apertures in a modern TEM. (after Champness, [16])

Electrons from the gun enter the condenser lens system whose purpose it is to control the illumination of the sample. The condenser lens system in many microscopes, consists of two lenses: Condenser 1 and Condenser 2, and a set of apertures as shown in figure 3.7. the first lens is used to form a demagnified image of the gun cross-over and determines the diameter of the beam on the sample. The strength of the Condenser 1 lens can be set to a small number of manufacturer predetermined settings. The Condenser 2 lens, being

user controllable, alters the intensity of the illumination of the sample by controlling the angular convergence of the beam. Further choice of the illumination conditions are provided by the aperture strip, which lies below the Condenser 2 lens. Selection of a smaller aperture provides a beam with higher spatial coherence but decreased current density [55]. Electrons after leaving the condenser lens system are incident on the sample and a diffraction pattern is produced in the back focal-plane of the objective lens. The diffraction lens can be reduced in strength (increasing its focal length) by decreasing the current in the windings so that a diffraction pattern is produced in the back focal-plane of the objective lens is focused on the viewing screen [16]. An objective aperture can be inserted located at the back focal-plane of the objective lens as shown in figure 3.8, the plane at which a diffraction pattern of the specimen is first produced,which limits the collection angle of the lens allowing us to control the depth of field, the depth of focus, the angular resolution of the diffraction pattern, etc [18]. Figure 3.8 shows the ray path of the electrons passing through the objective lens and selected area diffraction apertures when forming a diffraction pattern in the final screen. The use and features of the selected area diffraction aperture are discussed in the next two sections.

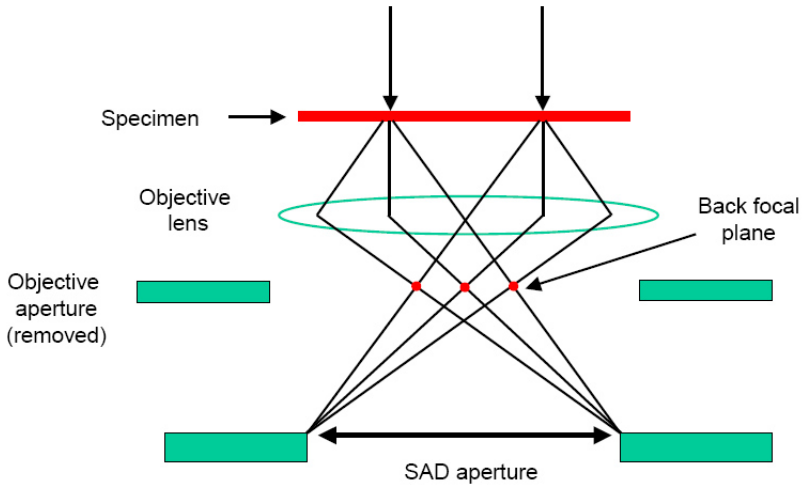

Figure 3.8: Ray diagram showing the objective lens in a SADP formation. (after Williams and Carter, [18])

3.4.2 SAD, CBED and Kikuchi patterns

A determinant feature of electron diffraction is the fact that the wavelengths achieved in the TEM are many times smaller than the lattice parameter of atomic arrays. Such a wavelength can be calculated considering the wave-particle duality of electrons through the de Broglie relation

$$\lambda = \frac{h}{p} \tag{3.8}$$

The momentum of an electron, is attained by accelerating through a potential V to give kinetic energy

$$eV = \frac{p^2}{2m} \Rightarrow \lambda = \frac{h}{\sqrt{2m_0 eV}} \tag{3.9}$$

But, electrons travel at relativistic speeds, and therefore the relativistic mass must be considered,$m_0 \rightarrow \gamma m_0$, where γ is the relativistic correction

$$\gamma = \sqrt{\frac{1}{1 - (\frac{v}{c})^2}} \tag{3.10}$$

this gives the relativistic wavelength of

$$\lambda = \frac{h}{\sqrt{2m_0 eV(1 + \frac{eV}{2m_0 c^2})}} \tag{3.11}$$

A typical electron wavelength is 0.0025 nm for 200 kV[18]. As the electron beam impinges on the crystal lattice plane in a given angle only the planes that fulfil equation 3.12 (Bragg's equation) generate diffraction spots in the pattern.

$$n\lambda = 2d_{hkl} \sin\theta \tag{3.12}$$

Using Bragg's equation and the geometry of the electron ray path shown in figure 3.9 described by the camera constant Lλ an equation for the interplanar spacing (d_{hkl}) between the planes that generate the diffraction pattern can be derived.

$$d_{hkl} = \frac{L\lambda}{D} \tag{3.13}$$

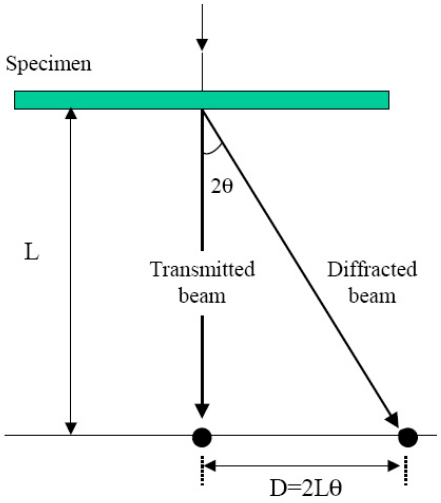

Figure 3.9: Formation of the diffraction pattern on the screen of the microscope. The two reflections are separated a distance D in a direction perpendicular to the planes. L is the camera length. (after Dorset, [20])

Where D is the distance between the incident 000 and the hkl spot in the diffraction pattern. Comparing the measured d_{hkl} value with tables containing the standard interplanar distances for the studied crystal structure allows the determination of the (hkl) plane generating the diffraction spot. To view a diffraction pattern on the viewing screen, the intermediate lens (and very weakly the projector lens) is changed so that the plane of the screen is now conjugate with the back focal plane of the objective lens. If an aperture of diameter R (selected-area aperture) is placed as diffraction aperture in figure 3.10a, only those electrons passing through an area of diameter R/M, where M is the magnification of the specimen, will reach the screen [16](under ideal conditions). The selected area aperture is demagnified back in the focal plane, around 50 times. So, a SAD aperture of 50 μm, will select an area of around 1 μm in the sample. The diffraction pattern from such an area is called selected area diffraction pattern (SADP). The selected area diffraction technique allows the observation of the diffraction pattern taken

from small areas of the specimen when the beam is approximately parallel [20]. Because of the very short wavelength of the electrons, the diffraction angle shown in figure 3.9, are very small as well. This means that the planes are all situated almost parallel to the beam[23]. In the case of diffraction at crystals with periodicities of the order of 10-100 nm, the range of camera lengths available by normal SAD may only give a small pattern. Thus, in order to achieve larger camera lengths, it is necessary a primary beam with an illumination aperture smaller than the diffraction angle [49].The subsequent lenses further magnify the diffraction pattern, and camera lengths of several hundreds of metres (about eight times larger than the maximum normally available in the SAD mode [16]) can be obtained.

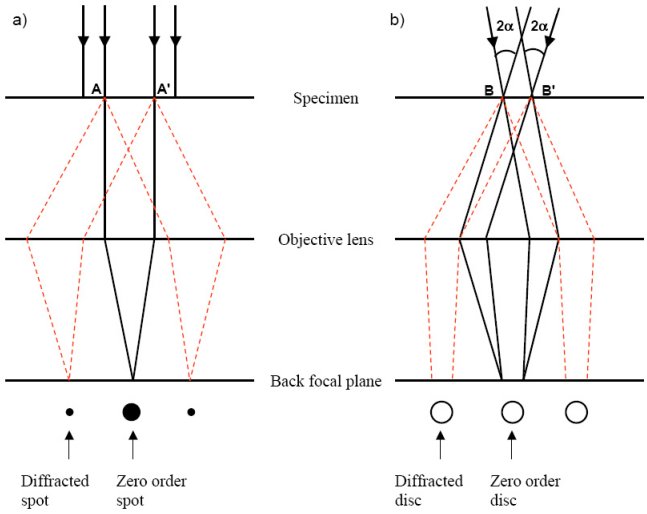

Figure 3.10: Ray path of a (a) conventional selected area diffraction pattern (SADP), (b) a convergent-beam electron diffraction pattern (CBEDP). (after Champness, [16])

If the electron beam is focused to a spot on the specimen, a convergent beam electron diffraction pattern (CBEDP) [22] is formed in the back focal plane of the objective lens. This is often called micro or nano-diffraction, as the volume of the specimen sampled by the electron beam is much smaller than in conventional SAD. The diffraction pattern is composed of discs (rather than spots) and the detail within the discs is sensitive to the crystal symmetry and to any strain in the crystal. The discs correspond to the points

of the SADP and may be indexed in exactly the same way [21]. The diameter of the discs depends on the angle of convergence 2α, and the size of the C2 aperture shown in figure 3.10b, controls this angle, which must be $> \theta_B$ (the Bragg angle). SAD and CBED are diffraction techniques based on elastically scattered electrons (electrons that have lost no energy during the scattering process). But as the thickness of the specimen increases, the probability for an electron to be scattered more than once increases. Some of these inelastically scattered electrons can be subsequently elastically scattered (Bragg diffracted) by lattice planes and produce Kikuchi lines [18]. As shown in figures 3.11a and 3.11b, two rays from the diffuse inelastic scattering are incident on the planes at the Bragg angle and will be diffracted by them. As ray 1 is closer to the forward direction than ray 2, it is more intense and an excess number of electrons will arrive in the back focal plane at B; therefore, a deficiency of electrons will be noticeable at D. This will generate a bright line at B and a dark line at D. these lines are the Kikuchi lines [16]. Since diffraction of electrons through the Bragg angle is occurring in all directions, the locus of the diffracted radiation is the surface of a cone (Kossel cone) which extends about the normal of the reflecting atomic planes with half apex angle $90^\circ - \theta_B$ as shown in figure 3.11c.

The angular separation of the pair of lines is 2θ and their spatial separation in the back focal plane is g (the same as the distance from the diffraction spot to the origin in a SADP). The bright line is associated with a hkl or $+g$ reflection and the dark line is associated to the $\bar{h}\bar{k}\bar{l}$ or a $-g$ reflection. Thus, they are useful to determine the exact orientation of a crystal to within about 0.1 degree. The crystallographic importance of Kikuchi patterns is based on the fact that they are directly related to the orientation of the planes from where they have been reflected. Therefore, the usefulness of Kikuchi patterns for determining orientations is superior to the SAD technique [24]. Besides the advantages of Kikuchi patterns mentioned already, the pattern can be qualitatively interpreted to obtain information on lattice strain [63], identification of grain/phase boundaries [62].

The interpretation of a Kikuchi pattern, i.e. the determination of the crystallographic orientation, is performed in two steps:

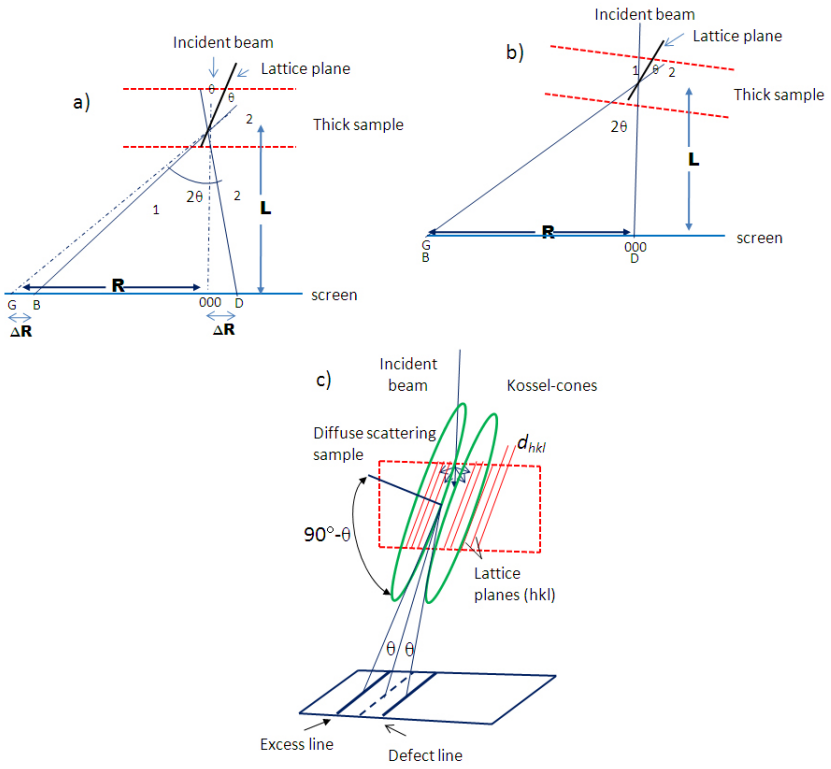

Figure 3.11: Geometry of Kikuchi lines. a) The lattice plane (hkl) is close to, but not exactly at, the Bragg angle θ to the incident beam. G is the diffraction spot hkl, b) rotation of the crystal in a) has brought the lattice to a Bragg condition with respect to the incident beam, c) Kikuchi lines in TEM showing the Kossel-cones (after Champness, [16])

- Indexing the pattern by identifying the crystallographic indices of the lines and poles in the pattern.
- Determining the relative position of the poles or lines with respect to an external reference frame.

The problem for the interpretation of Kikuchi patterns is that indexing and subsequent orientation determination are heavily time consuming and care is needed to avoid errors [61]. A Kikuchi diffraction pattern can be obtained in a TEM as well as in a SEM applying electron backscatter diffraction (EBSD).

3.4.3 EBSD

The combination of SEM with electron backscatter diffraction (EBSD) is a powerful technique which allows imaging and characterisation of microstructural crystalline materials [14]. EBSD is predominantly used in materials science for the measurement of crystal orientation and grain boundary maps in polycrystalline materials, and for the identification of the phase of crystallites [15].

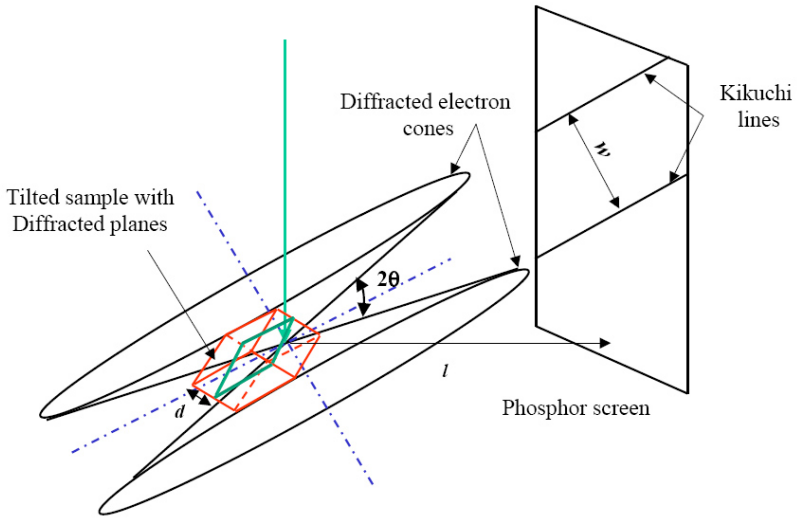

Figure 3.12: Ray diagram showing the geometry of Kikuchi lines formation during diffraction in EBSD (after Edington, [23])

Automation of pattern indexing and crystal orientation measurement are the principal features of this technique which allows rapid mapping of crystal orientations. The typical angular precision of orientation measurements made by commercial EBSD systems is of the order of 0.2 degrees and spatial resolution of the order of 20 nm [63]. Experimentally, EBSD is conducted using a scanning electron microscope (SEM) equipped with a phosphor screen, as shown in figure 3.12. The sample has to be tilted 70 degrees towards the EBSD detector. This is to reduce the path length of the backscattered electrons in the material and to enhance the backscattered signal by allowing the maximum diffraction of the electrons [11]. Diffraction of electrons from the atomic planes gives rice to backscattered Kikuchi patterns [23]. The set-up shown in figure 3.12 allows capturing diffraction

patterns of different points of a region that was imaged in an initial step using the in-lens secondary electron detector in the SEM. When a crystalline sample is examined, one would expect the EBSD to detect a small number of diffraction spots, since the highly collimated incident beam impinges the crystal lattice at a fixed angle. A large fraction of the primary electrons are inelastically scattered by the atoms of the sample material and this serves as a divergent electron source in the sample. Since this source of diffuse electrons is created near the sample surface, the electrons can undergo subsequent elastic scattering and exit the specimen as backscattered electrons [16]. Divergent electrons that impinge atomic planes at angles, which satisfy Bragg's equation, are diffracted to form a set of paired large angle cones corresponding to a specific lattice plane. These cones are detected as a pair of parallel Kikuchi bands and received on a phosphor screen, and a video (or CCD) camera captures the image of the pattern (from the phosphor screen) for further processing by a computer [13]. Orientations of grains/crystals can be determined by point analysis, where orientation data is collected from manually selected points on the sample surface, or by orientation mapping. During orientation mapping the electron beam scans the sample surface in a regular pattern step by step. At each step, electrons are diffracted at the crystallographic planes in the sample and a diffraction pattern is obtained. The EBSD software automatically locates the position of Kikuchi bands, measures band width and inter-band angles, and compares these to theoretical data about the relevant phase. In this way the orientation at a specific location (manually selected point or for each point in an orientation map) is determined. To allow high accuracy in orientation, digital image enhancement is incorporated in the software [34]. Since the centre line of a Kikuchi band is a projection of a diffracting crystal lattice plane, each band can be indexed by the corresponding Miller indices. The intersections of Kikuchi bands, or zones, correspond to the intersection of zone axes in the crystal with the phosphor screen and are indexed with direct-lattice indices. Indexing of the Kikuchi bands and zone axes, and calculation of the crystal orientation of the sample region that formed the pattern, is usually performed by an algorithm using the Hough transform of the diffraction pattern (figure 3.13) [72].

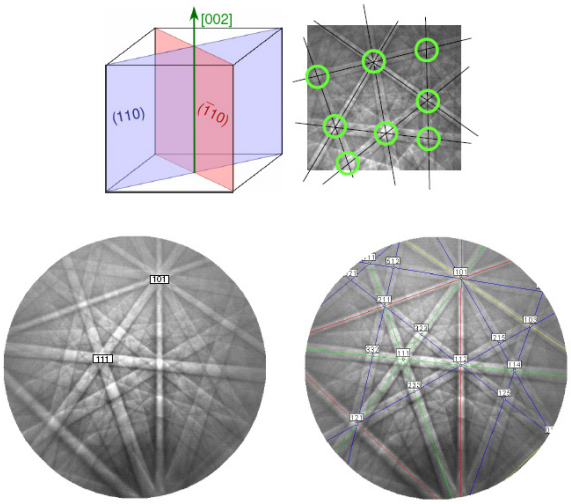

Figure 3.13: Crystal orientation calculation by identifying zone axes and indexing kikuchi patterns, using EBSD(after EDAX Courses, [34]).

Using Bragg's equation, it is possible to derive an approximation for d, the spacing of the diffracting lattice planes, which only depends on ω, the width of the Kikuchi band and parameters that are defined by the experimental setup

$$d = \frac{n\lambda}{2\sin\theta} = \frac{nl\lambda}{\omega} \tag{3.14}$$

where n is an integer, λ is the wavelength of the electrons, θ is the angle of incidence of the electrons on the diffracting plane and l the distance between the sample and the screen as shown in figure 3.12. Hence, planes with small d-spacings generate thicker Kikuchi bands than wider separated planes. Since the pattern is directly linked to the crystallography, the pattern changes as soon as the beam crosses a grain boundary. Therefore, the colour of the corresponding pixels also changes. Hence, grains with different orientations are represented by different colours in the orientation mapping (OM) [7]. When measuring an OM, there are usually some pixels which remain unidentified. Such zero solutions can be a result of poor pattern quality due to pattern overlap at grain boundaries, dirt on the surface, residual strains in the surface introduced by mechanical polishing, and/or due to the presence of an unidentified phase. Since EBSD is

a technique that analyses backscattered electrons with a short penetration depth, even a thin conducting coating layer distorts the diffraction pattern. This is the reason why non-conducting EBSD samples are coated with a carbon layer of around 3nm thick. The mapping procedure can also be used for phase identification. A phase map reveals the spatial distribution of the different identified phases in the mapped region. In order to be able to identify patterns of a particular phase, the unit cell parameters, the atom possitions and the crystallographic space group of the phase need to be known. The time required to acquire orientation data depends on the detector sensitivity, the speed of the data processing system, the number of bands to be identified for orientation determination, Hough transform resolution, the number of phases to be distinguished and the step size selected.

3.4.4 Mapping with Kikuchi patterns

When comparing the Kikuchi patterns arising from TEM and EBSD, two main differences can be found.

- The capture angle is about five times greater for the EBSD pattern than for the TEM pattern. This is a consequence of the experimental set-up in both cases and facilitates pattern indexing and identification of the symmetry elements for EBSD and TEM.

- $\bar{h}\bar{k}\bar{l}$ The Kikuchi lines are sharper in the TEM case than in that of EBSD, such that defect and excess lines can be distinguished in the former. This is a consequence of the different electron transfer functions in the two cases and means that the greater precision in measurements from the diffraction pattern is obtained in TEM [7].

As has been stated already, Kikuchi patterns are used for orientation determination by creating orientation maps. The problem with mapping with Kikuchi patterns is that indexing the patterns is extremely time consuming and prone to errors [64]. EBSD offers a fully automatic creation of orientation maps. Nonetheless, TEM offers the advantage of better spatial resolution and better accuracy in relative orientation maps on transmission

microscopes. A very important and efficient system used in this thesis, for creating maps using Kikuchi patterns is the Euclid's Phantasies (EP) software [64]. In this system, orientation maps are obtained using a step-by-step beam scan on a computer controlled TEM with a CCD camera. At each step, acquired diffraction patterns are indexed and orientations are determined. The accuracy of orientation determination can be better than 0.1 degree. The spatial resolution is estimated to be about 10 nm. The latter feature makes this TEM orientation mapping system an important tool for studies at fine scale unreachable by SEM/EBSD systems.

3.5 TEM imaging

As mentioned in section 3.4 and shown in figure 3.8, the objective aperture is located at the back focal plane of the objective lens. In this plane, the distance from the optic axis represents the angle relative to the optic axis of the electrons that have just left the specimen [23,30]. When electrons leave the specimen parallel to the optical axis, they are deflected by the objective lens and cross the optical axis at the back focal plane (see figure 3.8). The electrons that arrive at the specimen parallel to the optic axis, and are scattered through an angle α, arrive at the objective lens at a radial distance $R = utan\alpha \approx f$ from the optic axis (see figure 3.14).

After being deflected by the objective lens, these electrons cross the optic axis at the first intermediate image plane (see figure 3.15) at a relative large distance from the lens ($\sim$ 10 cm). Therefore, below the objective lens the scattered electron beam is almost parallel to the optic axis, and its displacement from the optic axis in the back focal plane is [55]. As shown in figure 3.14, by inserting an aperture of diameter D (centred around the optic axis) at the back focal plane, we can ensure that the electrons passing through the rest of the imaging system are those with scattering angles between zero and α, where $\alpha \approx tan\alpha \approx R/f = D/(2f)$ [30]. Electrons scattered through larger angles are absorbed by the aperture and do not contribute to the final image. By making α small, it is possible to ensure that almost all of the scattered electrons are absorbed by the diaphragm [18].

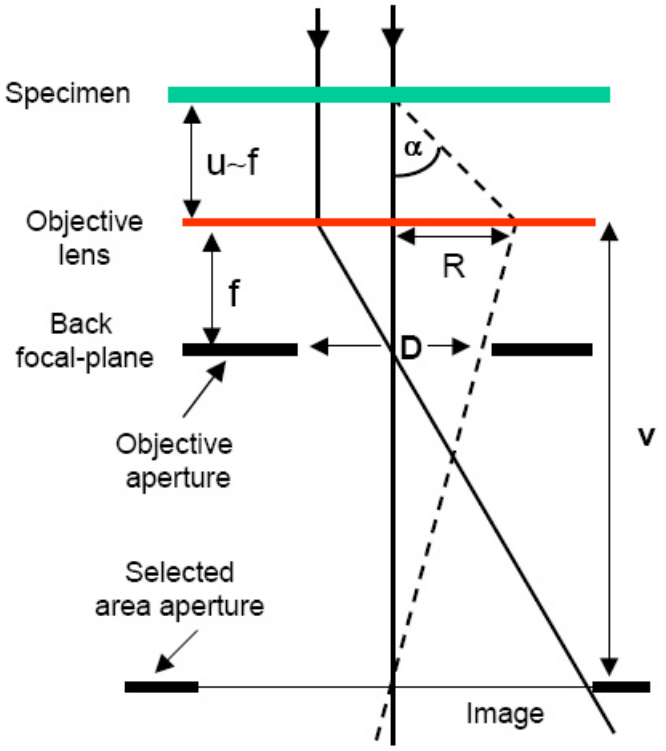

Figure 3.14: Electron ray path at the level of the objective lens. The diffracted area is selected with the selected-area apperture located in the image plane of the objective lens. (after Edington, [23]).

As a result, regions of the specimen that scatter electrons strongly will appear as dark areas in the final image [55].

Conventional TEM allows either the magnification of the image or the acquisition of the diffraction pattern formed by the objective lens. A major advantage of the TEM is the ease with which a microscopist can switch from one mode to the other. The formation of a diffraction pattern, as been discussed in section 3.4, is achieved in the TEM by adjusting the imaging system lenses so that the back focal plane of the objective lens acts as the object plane of the intermediate lens. Then the diffraction pattern is projected at the screen as shown in figure 3.15a. On the other hand, readjusting the intermediate lens so that its object plane is the image plane of the objective lens, an image will be shown at the screen as shown in figure 3.15b [17].

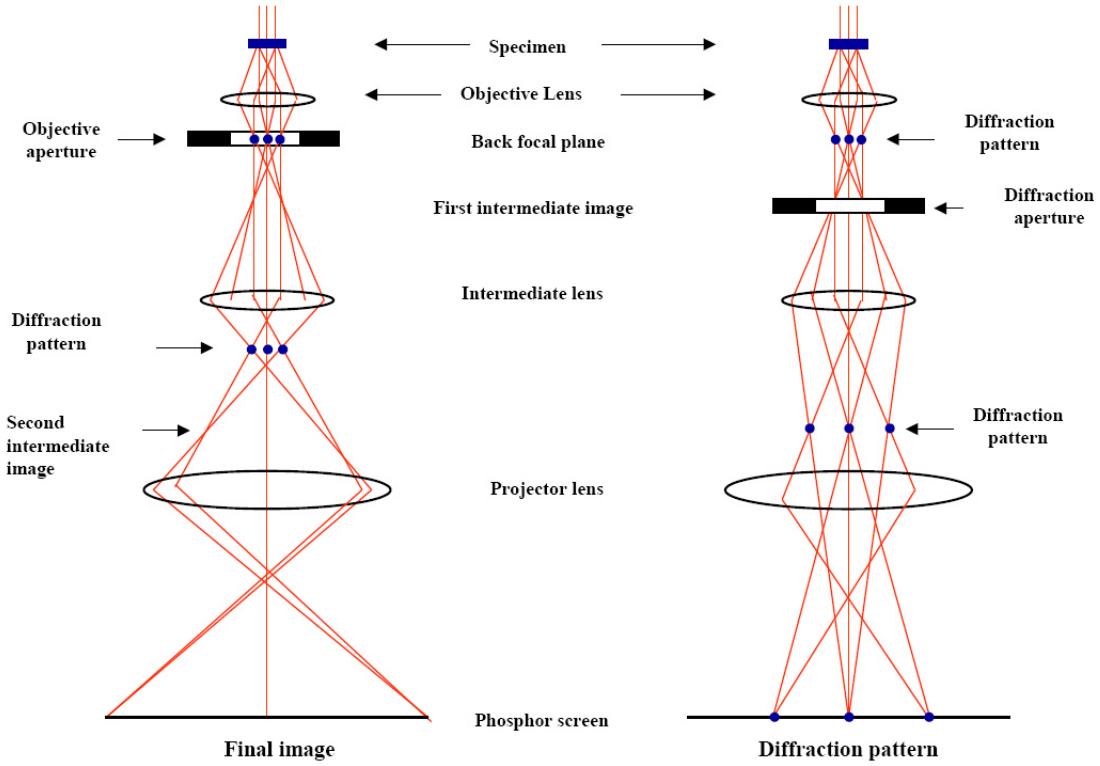

Figure 3.15: Electron ray path for image and diffraction mode. Imaging mode: the intermediate image, produced by objective lens, is magnified by the intermediate and projective lens. Diffraction method: the intermediate lens is adjusted so that the back focal plane of the objective lens is imaged on the phosphor screen (after Williams and Carter, [18]).

3.5.1 Bright field and Dark field

From equation 3.12 and using the small-angle approximation, it is possible to deduce that the wavelength of the electrons in TEM can be written in terms of the scattering angle as:

$$\lambda = 2\theta_{hkl} d = \theta d \tag{3.15}$$

where $\theta = 2\theta_{hkl}$ is the angle of scattering of the electrons resulting from the diffraction process as shown in figure 3.9. In a polycrystalline material, few particular orientations of

the atomic planes will satisfy equation 3.13 and these will diffract the incident electrons strongly. Provided the corresponding scattering angle θ exceeds the semi-angle α of the objective aperture, the diffracted electrons will be absorbed by the objective diaphragm and those areas of the specimen will appear dark in the TEM image [49]. Areas of the specimen where the atomic planes do not satisfy equation 3.13 will appear bright, as most electrons passing through them will remain un-deviated.

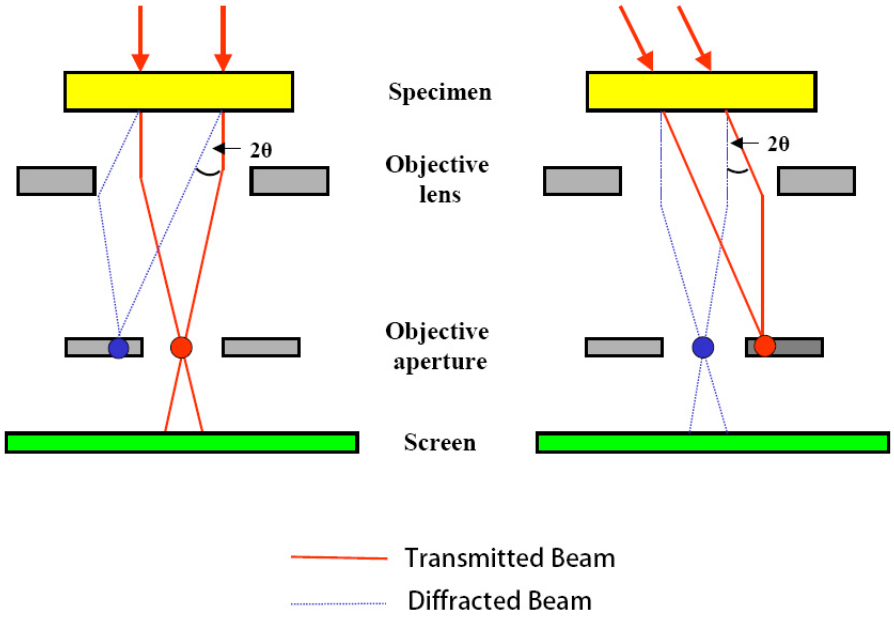

Figure 3.16: Ray diagrams showing (a) a Bright field image formed by the direct beam, and (b) a Dark field image formed with a specific off-axis scattered beam (after Williams and Carter, [18]).

From a SAD pattern it is possible to obtain images in two different ways: 1) using the transmitted beam, 2) using the diffracted beam. These two ways of imaging are the most basic imaging operations performed in the TEM and are called Bright field and Dark field respectively. The normal procedure to form a Bright field image from an SAD pattern, is by inserting an objective aperture around the incident beam in the back focal plane of the objective lens, blocking out most of the diffraction pattern, and to project the image formed by the lens onto the viewing screen [18]. In practice it is better to use

the beam tilts to shift a diffracted beam so that it goes through the aperture since this ensures that the image-forming rays after the sample still travel close to the optic axis and do not suffer excessive lens aberrations. Thus, if we select either of the diffracted reflections the image formed by the lens and projected onto the viewing screen is a Dark field image (figure 3.16).

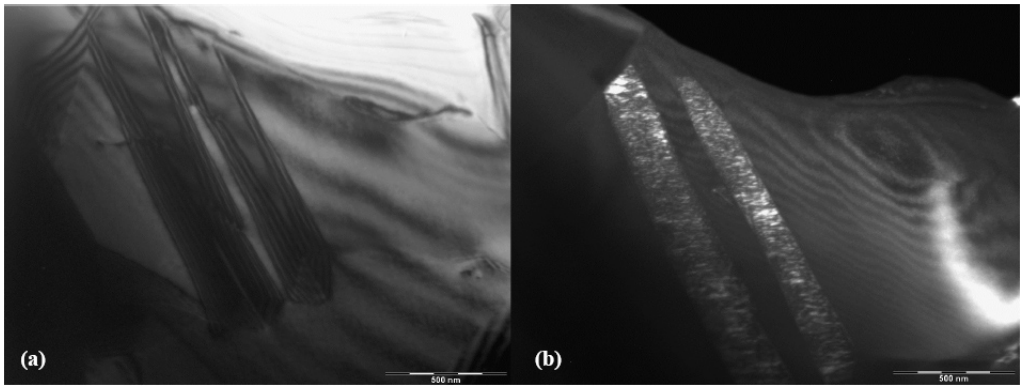

Figure 3.17: A comparison of (a) a Bright field image of two domains in a PZT ceramic showing the domain boundaries, and (b) a Dark field image of the same two domains showing the nano-structure that lies inside the domains.

As the areas that diffract strongly appear darker in the Bright field mode and brighter in the Dark field mode, these techniques are used in a complementary way. The aim of taking Dark field images is to get different contrast than the one obtained in the Bright mode and thus, different information as shown in figures 3.17a and 3.17b. Dark areas in a bright field image could be diffracting into a number of different beams, whereas bright areas in a dark field image are definitely diffracting into the selected beam, thus, interpretation can be simpler. Also, contrast can be better with bright features on a dark background than with dark features on a bright background. As the areas that diffract strongly appear darker in the Bright field mode and brighter in the Dark field mode, these techniques are used in a complementary way. The aim of taking Dark field images is to get different contrast than the one obtained in the Bright mode and thus, different information as shown in figures 3.17a and 3.17b. Dark areas in a bright field image could be diffracting into a number of different beams, whereas bright areas in a dark field image

are definitely diffracting into the selected beam, thus, interpretation can be simpler. Also, contrast can be better with bright features on a dark background than with dark features on a bright background. Ordinary Dark field imaging techniques (figure 3.16) allow us to use only a small fraction of the scattered electrons. This can be a disadvantage if were interested on imaging all the portions of the specimen or all the phases that are diffracting into a set of diffraction spots. To overcome this disadvantage, as well as to avoid taking all the individual reflections in a SADP, we can carry conical dark field imaging (also called hollow-cone) [18]. In this Dark field imaging technique, a specific set of diffracted beams is collected by the objective aperture when the conical-scanning beam satisfies a particular Bragg condition. The specimen is illuminated along a hollow cone and, by suitable control of the microscope's tilt coils, the incident electron beam is bent spinning around the optic axis [74,75]. Using this illumination high angle cone dark field images are obtained which differ significantly from ordinary bright or dark field images. This can be demonstrated by the two images in figure 3.18 (a further impressive example is published in [75]). Figure 3.18b shows a dark field image of a rhombohedral 60:40 PZT ceramic taken with the ordinary dark field technique. In this figure we cannot see any structure inside the wedge shape domain. Whereas in figure 3.18a we can see the nanodomains inside the same wedge shape domain. Figure 3.18a is a conical dark field image. In this thesis work, all the dark field images presented in the experiments are conical dark field images. These images were taken using the conical option in the Dark field mode available in the T20 and TF20 FEI Tecnai microscopes.

3.5.2 Crystallographic information from EM

The simultaneous availability of different types of information has made EM very important in materials science. As the length scale of materials problems steadily decreases, nano-scale structural crystallography information is becoming more necessary. Although the standard operating mode in the electron microscope is direct imaging, widely used in morphological studies, defect studies, and certain types of atomic scale investigations, combining this with diffraction information in becoming increasingly important. By

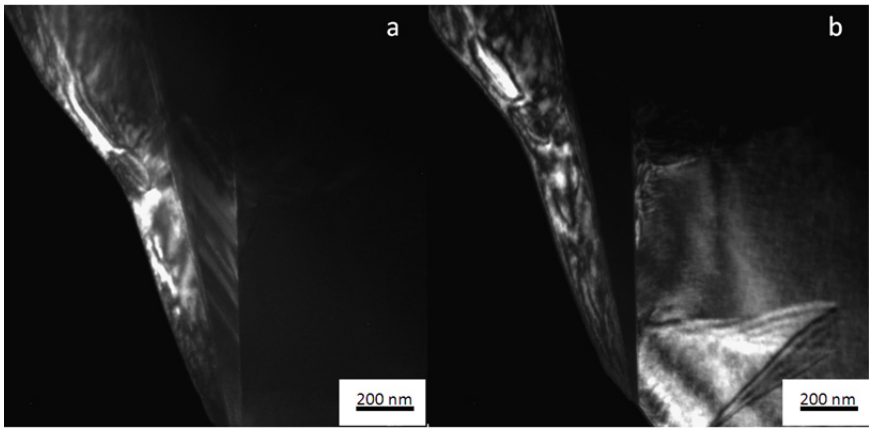

Figure 3.18: A comparison of (a) a conical dark field image of a wedge shape domain, and (b) an ordinary dark field image from the same area. Both images show a wedge shape domain from a rhombohedral 60:40 composition PZT ceramic with different information in the inside.

changing lens excitations in the imaging system, the diffraction pattern of the illuminated region is displayed, providing detailed symmetry and crystallographic information [56]. Historically, X-ray techniques have been at the forefront of structural crystallography enabling straightforward determination of structure models from diffraction intensity measurements [57]. Nonetheless, there are several disadvantages from the perspective of nanomaterials characterisation. One of the most obvious disadvantages is in determining the structure of areas with an extent of less than 10 nm, or sorting out nanomaterials where more than one phase is present. TEM has traditionally played a complementary role to X-ray methods in crystallography, partly because image resolution was insufficient except in specialized high-energy instruments and also because data quality from Transmission Electron Diffraction (TED) was limited by multiple scattering. Nevertheless, the ability to form a fine probe and to collect diffraction patterns are of significant advantage. Another important advantage is that we can relate the features in a bright or dark field image to the crystallography that can be determined from a diffraction pattern from the same area, allowing a local understanding of the crystallography in materials. In recent years, the field has seen a huge leap in the imaging capabilities of

high resolution TEM (HRTEM) and high resolution STEM (HRSTEM) modes due to the introduction of aberration-corrective optics allowing point resolutions of less than $1\mathring{A}$ [58]. This also allows an understanding of local crystallography, which may not be the same as global average crystallography. The work done in this thesis combines the advantages of TEM imaging and diffraction to study local crystallography in ferroelectrics and antiferroelectrics.

Bibliography

[1] Lange F.F., Acta Met., 15, 311 (1967).

[2] Randle, V., (1993) The measurement of the grain boundary geometry, IOP Publishing.

[3] Randle, V., and Ralph, B., Journal of Materials Science. 21, 3823-3828, (1987).

[4] Bhadeshia, H.K.D.H., (1987) Worked examples in the geometry of crystals, The Institute of Metals.

[5] Bollmann, W., (1982) Crystal lattices, Interfaces, Matrices, Published by the Author.

[6] Sutton, A.P., and Balluffi, R.W., (2003) Interfaces in Crystalline Materials, Oxford Science Publications.

[7] Randle,V. and Engler, O., (2000) Texture Analysis, CRC Press.

[8] Wenk, H.R., Lonardelli, I., Franz, H., Nihei, K., and Nakagawa, S., Geophysics, 72, E69-E75, (2007).

[9] Schwartz, A.J., Kumar, M. and Adams, B.L., (2001) Electron Backscatter Diffraction In Materials Science, Kluwer Academic/Plenum Publishers.

[10] Werner, E., and Prantl, W., J. Appl. Cryst. 21, 311-316, (1988).

[11] Farooq, M.U., PhD Thesis, Chalmers University of Technology, Gothenburg, Sweden (2005).

[12] Matthies, S., and Wenk, H.R., Vinel, G.W., J. Appl. Cryst. 21, 285-304, (1988).

[13] Randle, V., M. Caul, M. and Fiedler, J., 3, 224-233, (1997).

[14] Humphreys, F.J., Journal of Materials Science, 36, 3833-3854; (2001).

[15] Dingley, D.J., and Randle, V., Journal of Materials Science, 27, 4545-4566; (1992).

[16] Champness, P.E., Electron Diffraction in the Transmission Electron Microscope. BIOS (2001).

[17] OKeefe, M.A., Ultramicroscopy, 108, 196-209; (2008).

[18] Williams, D.B., Carter, C.B., (1996) Transmission Electron Microscopy, Kluwer Academic/Plenum Publishing.

[19] De Graef, M., McHenry, M.E., Structure of Materials, Cambridge (2007).

[20] Dorset, D.L., Estructural Electron Crystallography, Plenumen Press (1995).

[21] Stoter, L.P., Journal of materials Science, 16, 1356-1366, (1981).

[22] Zuo, J.M., Ultramicroscopy, 41, 211, (1992).

[23] Edington, J.W. (1975) Electron Diffraction in the Electron Microscope, MacMillan, London.

[24] Kaynuma, Y., Acta Cryst., 8, 247, (1955).

[25] Goodman JW, Introduction to Fourier Optics, McGraw-Hill, NY (1968).

[26] Gaskill JD, Linear Systems, Fourier Transforms and Optics, John Wiley, NY (1978).

[27] Spence JCH, (1988), Experimental High-Resolution Electron Microscopy, Oxford University Press.

[28] Snoeck E, Warot B, Ardhuin H, Rocher A, Casanove MJ, Kilaas R y Htch MJ, Thin Solid Films 319 (1998) 157.

[29] Stadelmann P, Ultramicroscopy 21 (1987) 131.

[30] De Graef, (2003), Introduction to Conventional Transmission Electron Microscopy, Cambridge University Press.

[31] Tilley, R., (2006) Crystals and Crystal Structures, Wiley.

[32] Hammond, C., (1993) The basics of Crystallography and Diffraction, Oxford University Press.

[33] Kingery, W. D., Bowen, H.K., Uhlmann, D.R., (1976) Introduction to Ceramics, John Willey and Sons.

[34] EDAX Courses at www.edax.com

[35] Shao-Ju Shih, Myung-Beom Park, Cockayne D.J.H., Journal of Microscopy, 227, (2007).

[36] Proc. 14th conf. Electron Microsc. (ICEM), Cancun, Mexico. IOP Pub. Danvers USA (1998).

[37] MacLaren, I., Farooq, M.U., Villaurrutia, R., Microscopy Today, 16, 5, (2008).

[38] Reaney, I.M., Petzelt, J., Voitsekhovskii, V.V., Chu, F., Setter, N., J. Appl. Phys. 73, 3, (1994).

[39] Villaurrutia, R., MacLaren, I., Pelaiz, A., EMC 14th European Congress, Aachen, Germany, (2008).

[40] Farooq, M.U., Villaurrutia, R., MacLaren, I., Kungl, H., Hoffmann, M.J., Fundenberger, J.-J. and Bouzy, E., Journal of Microscopy, 230, 445, (2008).

[41] Farooq, M.U., Villaurrutia, R., MacLaren, I., Burnett, T.L., Comyn, T.P.,Bell, A.J., Kungl, H., and Hoffmann, M.J., J. Appl. Phys., 104, 024111, (2008).

[42] Suarez-Gomez, A., Durruthy, M.D., Pelaiz-Barranco, A., Calderon-Pinar, F., De Frutos, J., Saniger- Blesa, J.M., Revista Mexicana de Fisica S, 52, 2, (2006).

[43] Suarez-Gomez, A., PhD. Thesis, University of Havana, (2003).

[44] Hammer, M., and Hoffmann, M.J., J. Am. Ceram. Soc., 81, 3277-84, (1998).

[45] Atkin, R.B., and Fulrath, R.M., J. Am. Ceram. Soc., 54, 265-70, (1971).

[46] Kingon, A.I., and Clark, J.B., J. Am. Ceram. Soc., 66, 256-60, (1983).

[47] Sample preparation companies, Allied High Tech Products web-page, www.alliedhightech.com.

[48] Egerton, R.F., (2008), Physical Principles of Electron Microscopy, Springer Press.

[49] Reimer, L., Kohl, H., (2008), Transmission Electron Microscopy, Springer Series in Optical Sciences. [New York, U.S.A.].

[50] Zuo, J., Vartanyants, I., Gao, M., Zhang, R., Nagahara, L.A., Science, 300, (2003)

[51] Dove, M.T., (2003) Structure and Dynamics: An atomic view of materials, Oxford University Press.

[52] Huang, W.J., Jiang, B., Sun, R.S. and Zuo, J., Ultramicroscopy, 107, 1159-1170, (2007).

[53] Huang, Zuo, J., Jiang, B., Kwon, K.W., and Shim, M., Nature Phys., 5, 129-132, (2009).

[54] Zuo, J., Tao, J., Phys. Rev. B., 63, 060407, (2001).

[55] Craven, A., Personal Notes for Microscopy Course, University of Glasgow, (2007).

[56] Spence, J.C.H., Science, 299, 839, (2003).

[57] Hauptman, H.A., Acta Cryst., A52, 490-496, (1996).

[58] Haider, M., Muller, H., and Uhlemann, S., Ultramicroscopy, 81, 163-175, (2000).

[59] Krivanek, O.L., Corbin, G.J., Dellby, N., Elston, B.F., Keyse, R.J., Murfitt, M.F., Own, C.S., Szilagyi, Z.S. and Woodruff, J.W., Ultramicroscopy, 108, 179-195, (2008).

[60] Wen, J., Mabon, J., Lei, C., Burdin, S., Sammann, E., Petrov, I., Shah, A.B., Chobpattana, V., Zhang, J., Ran, K., Zuo, J., Microsc. Microanal., 16, 183-193, (2010).

[61] Baba-Kishi, K.Z., and Dingley, D.J., J. Appl. Cryst., 22, 189-200, (1989).

[62] Went, M.R., Winkelmann, A., Vos, M.., Ultramicroscopy, 109, 1211-1216, (2009).

[63] Wilkinson, A.J., Meaden, G., and Dingley, D.J., Mater. Sci. Tech., 22, 1271, (2006).

[64] Schwarzer, R.A., Ultramicroscopy, 67, 19-24, (1997).

[65] Pennycook, S.J., and Jesson, D.E., Phys. Rev. Lett., 64, 938, (1990).

[66] Browning, N.D., Chrisholm, M.F., and Pennycook, S.J., Nature, 366, 143-146, (1993).

[67] Yan, Y., Meaden, Chrisholm, M.F., Duscher, G., Maiti, A., Pennycook, S.J. and Pantelides, S.T., Phys. Rev., 81, 3675-3678, (1998).

[68] Abe, E., Pennycook, S.J., Painter, G.S., and Becher, P.F., Nature, 428, 730-733, (2004).

[69] Urban, K.W., Nature Materials, 8, 460-462, (2009).

[70] Krivanek, O.L., Chisholm, M.F., Nicolosi, V., Pennycook, T.J., Corbin, G.J., Delby, N., Muritt, M.F., Own, C.S., Szilagyi, Z.S., Oxley, M.P., Pentelides, S.T., and Pennycook, S.J., Nature, 464, 571-574, (2010).

[71] Matsunaga, H., Nishimura, H., Saito, T., Yamamoto, T., and Ikuhara, Y., Philos. Mag., 83, 4071-4082, (2003).

[72] Wilkinson, A.J., and Hirch, P.B., Micron, 28, 279-308, (1997).

[73] Schwarzer, R.A., and Gerth, D., Journal of Electronic Materials, 22, 607-610, (1993).

[74] Hartung, F., and Schmitz, G., Phys. Rev. B., 64, 245418, (2001).

[75] Schmitz, G., and Haider, F., Scripta Mater., 37, 1951, (1997).

Chapter 4

Local crystallography and mapping of domain structures in tetragonal PZT

The different phase transformations occurring below the Curie temperature in PZT ceramics result in a high number of crystallographic transformations and unit cell misfits at grain and domain boundaries which modify the domain structure and hence, the macroscopic properties of such materials. In order to assess these crystallographic alterations, a microscopy technique sensitive to small changes in orientation as well as an adequate technique for data analysis and interpretation is necessary. In that sense, electron diffraction Kikuchi patterns in TEM together with electron backscatter diffraction techniques are applied to measure the angle of misorientation in the domain boundaries. The data acquired from both techniques are used to calculate the angle of misorientation across the domain boundaries in order to assess the c/a ratio and to compare these results with x-ray data.

Section 4.1 talks about the local crystallography at domain boundaries, principally in 180° and 90° boundaries in lamellar domains. Section 4.2 gives a reflection in terms of the crystallographic mismatch between the boundaries referred to in the previous section. Section 4.3 describes the experiments carried out using EBSD and shows the

results obtained. Section 4.4 shows the experiments and results carried out using TEM Kikuchi patterns comparing them with the ones obtained with EBSD.

4.1 Local crystallography at domain boundaries.

All PZT compositions form a simple cubic perovskite phase with the space-group $Pm3m$ above the Curie temperature. The symmetry of the structure is lowered in the paraelectric-ferroelectric transition, because the dipole that appears in the unit cell as a result of the displacement of the cations, results in a non-cetrosymmetric unit cell [4].

Thus, below the Curie temperature Lead Zirconate Titanate ferroelectric ceramics ($PbZr_xTi_{1-x}O_3$) with nominal compositions of $x \leq 0.52$, adopt a tetragonally distorted perovskite structure [1] with space-group $P4mm$. This crystallographic distortion coupled with the electric polarisation, as explained in chapter 2, leads to the piezoelectric effect found in these materials [2]. This results in lamellar domain structures with the domain boundaries on stress-free {101} planes as shown in figure 4.1. The differing intensities of the domains arises from a different value of the deviation parameter s from Bragg's condition in adjacent domains [25].

Two kinds of ferroelectric domain boundaries can be found in tetragonal PZTs, 180° and 90° domain boundaries. As was explained in chapter 2, both domain boundaries may reduce the effects of the depolarising electric field, but only the 90° domain boundaries may minimise the elastic energy [26].

For the case of the undoped PZT with a composition of $x=0.5$, 180° domain boundaries were found with zigzag morphology between 90° domain boundaries as shown in figure 4.2. These 180° domain structures located between 90° domains and exhibiting zigzag morphology have been studied by Xinhua *et.al.* and indicate that 180° domains are 90° domain-dependent [25]. Since below T_c the crystal, because of its symmetry, must belong to one of the pyroelectric classes [3], and since the domains differ in the direction of polarisation, they must differ as well in the orientations of their crystallographic axes [27]. Therefore, from the crystallographic point of view, the domain structure is

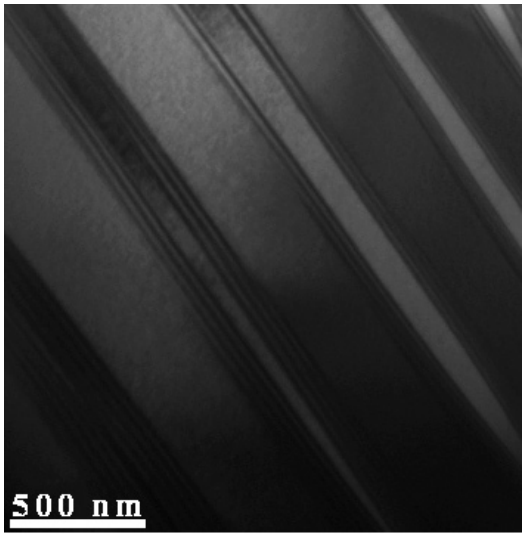

Figure 4.1: Lamellar domains from tetragonal PZT ceramics with nominal compositions of *x=0.5*. This image corresponds to a bright field image.

identical with the twinning structure. In contrast to the ordinary twinning, however, in ferroelectrics the twins arise from a common and uniform paraelectric phase as explained above. For ferroelectrics the twin structure is of the utmost importance as it determines the nature of the polarisation-reversal process, influences the crystal properties due to the presence of individual walls between domains, and because different domains have different orientations with respect to external fields [3].

Such twins occur at the intersection of the domains corresponding to different orientation variants of a lower-symmetry unit cell with respect to the higher-symmetry parent phase. The properties of the twins play an important role in the arrangement of the different domains [6]. The symmetry elements for this space-group are 2 and 4 fold rotations about the c axis together with mirror planes on (100), (010), (110), and the $(1\bar{1}0)$ [2]. At a 90° domain wall the unit cells in the two domains related by a rotation of nearly 90° about a $\langle 010 \rangle$ axis. The exact rotation angle is related to the c/a ratio of the material as explained in chapter 3. There have been suspicions in the past that the structure of PZT is not always homogeneous due to processing considerations. Therefore, assessing local (sub-micron scale) crystallography is important. This local crystallography can be

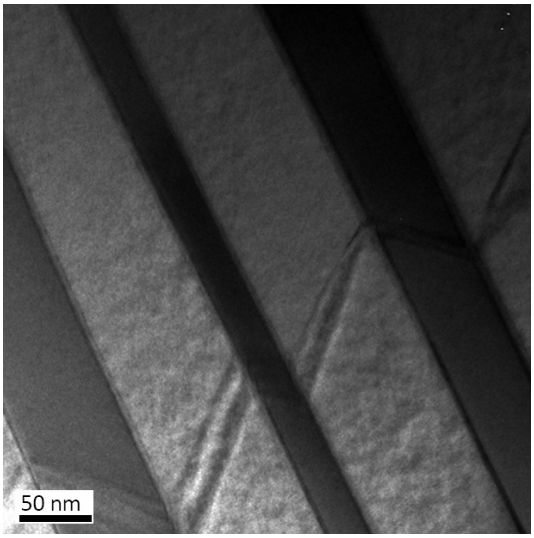

Figure 4.2: 180° domains with zigzag structure between 90° domains observed in tetragonal PZT ceramics ($PbZr_xTi_{1-x}O_3$) with nominal compositions of x=0.5

assessed using orientation mapping in electron microscopy, provided the accuracy of orientation determination is sufficient ($\sim 0.1°$). The study of tetragonal PZT ferroelectric ceramics in this work, aimed to develop automated methods for accurate and unambiguous indexing of domain orientations, using both electron backscatter diffraction (EBSD) and transmission electron microscopy (TEM) Kikuchi patterns, assessing the accuracy of such techniques using these to make some initial comparisons of local and bulk crystallography [35]. Internal stresses are developed by all ferroelectric crystals as none of them cool homogeneously through the transition temperature. In that sense, the domain boundaries formation can be understood as a process for reduction of elastic energy [11]. The majority of boundaries formed in such conditions are 90° domain boundaries, which are a common feature of tetragonal ferroelectrics[5,6]. These boundaries separate regions where the c axis is rotated by approximately 90°. Perfect lattice matching between adjacent domains is only found on one given {101} plane [3] and nominally results in the formation of lamellar domains as described above [2]. This matching has as a consequence, that the angle between the two c axes deviates from 90° as shown in figure 2.6 in chapter 2. The c axes in either side of the boundary include an angle of 90°-δ [6],

where $\delta = 90° - 2\tan^{-1}(\frac{a}{c})$. This deviation from 90° is geometrically required to form a coherent twin interface due to the tetragonality of the PZT 50/50 [11].

4.2 The EBSD treatment.

It is important to stress the fact that the etching and coating are of the utmost importance especially in high spatial resolution EBSD of insulators, and a perfect balance in between these two is essential in order to avoid the drift in the sample and the blurring of the Kikuchi patterns. In the case of PZT ceramics, the etching process is a delicate procedure in EBSD sample preparation as it reveals the domain boundaries, grain boundaries, dislocations and the entire surface of the sample. Because EBSD is performed at high tilts (74° in our case) and the interaction volumes are relatively small, it is a very surface-sensitive technique. Any residual plastic deformation, or inhomogeneities due to fabrication processes, left on the sample surface will affect the Image Quality (IQ) of the patterns as described previously. Other methods can be employed for preparing the sample surface, such as chemical etching. Care must be exercised not to overetch the sample, as this can introduce surface topography, which also tends to degrade the electron backscatter diffraction pattern quality [28,29]. For example, etchants that attack boundaries can leave significant valleys at the boundaries. This can make it difficult to obtain good patterns in areas immediately neighbouring the boundaries. On the other hand, the coating procedure is also critical. For non-conducting PZT samples, the application of a carbon layer is essential to observe high-quality Kikuchi patterns. Carbon is chosen as it has a low atomic number and should therefore minimise absorption effects. As the coating thickness increases, the pattern signal to noise ratio decreases due to diffuse scattering from the coating, and finally, the patterns become completely obscured [30]. Besides these facts, it has been suggested by Koblischa-Veneva *et.al.* that the pits created by etching can cause charging under the beam, which can be overcome with carbon coating [31]. In the case of the experiments carried out in this thesis, it was unfortunately not possible to measure the absolute thickness of the coating used for

these samples. The coating thickness was, nevertheless, maintained at a constant value by observing changes in resistance of a Cu grid, connected to an electric circuit, placed beside the sample in the coating chamber; as the coating thickness increases the resistance of the grid decreases and this can be used to reproducibly apply a coating thickness suitable for non-conducting samples but still allowing good EBSD patterns. The EBSD data was obtained using a FEI Quanta 200F environmental scanning electron microscope (SEM) (FEI, Eindhoven, The Netherlands) equipped with an EDAX Digiview II camera (EDAX-TSL, Draper, Utah, USA) to capture the EBSD patterns. For EBSD pattern acquisition the microscope was operated at 25 kV accelerating voltage and 13 mm working distance with the sample tilted to 74° (the maximum allowable tilt for this microscope) using OIM EBSD data acquisition and data analysis software from EDAX (EDAX-TSL, Draper, Utah, USA). The EBSD system was carefully calibrated at the given working distance before the execution of the experiments. The lattice parameters used for EBSD data analysis (as well as the ones for TEM) were obtained from X-ray diffraction experiments performed using a Siemens D500 diffractometer with Cu Kα radiation using an angular range from 20° to 72.5° and a step size of 0.02°. The diffractograms were obtained from bulk samples, which were polished on 4000 grit silicon carbide papers. Following polishing, the samples were heat treated at 500°C for 4 hours to reduce texture effects. The samples were made by Hans Kungl et. al. in the University of Karlsruhe, Germany [35]. Due to their non-conducting nature, ceramics are more difficult than metals to investigate using EBSD, especially when the goal is to obtain high-resolution orientation data from fine microstructural details. Orientation mapping an area of less than 1 μm^2 is similar to a stationary electron beam. These conditions lead to problems like sample charging, image drift and sample surface contamination under the electron beam making long exposures and large maps almost impossible, even when the sample is coated. Therefore, a strategy had to be devised to minimise these problems as well as to obtain the best quality data. To minimise charging and contamination of area of interest an adjacent area was used to refine the focus. The drift problem was minimised by using smaller beam currents. Further a 4 x 4 binning of the patterns reduced the acquisition

time considerably without compromising the quality of the patterns needed for our work. An accelerating voltage of 25kV was used to more accurately measure the narrow bands and a convolution mask of 5 x 5 pixels was used to enhance and identify peaks in the Hough transform of the EBSD patterns.

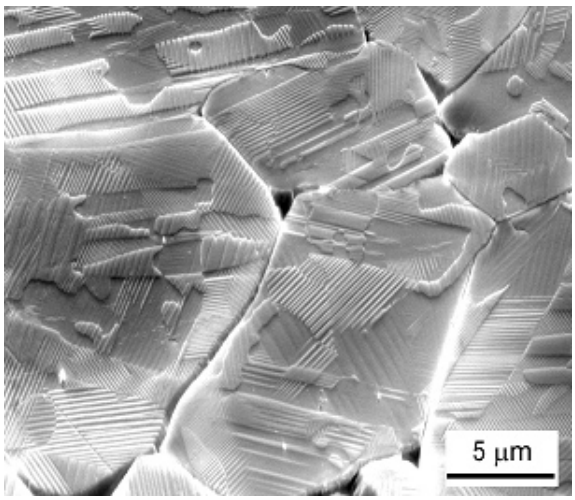

Figure 4.3: SEM secondary electron image of the domain structure from an undoped PZT 50%Zr-50%Ti sample, after etching.

A secondary electron SEM image at a relatively low magnification in fig. 4.3 shows an overall distribution of domains across several grains in a PZT sample slightly etched with 100 mL H_2O, 5 mL HCl and 5 drops HF. The lamellar structure of the domains can be clearly seen across much of the surface, and it is also clear that multiple domain structures occur within each grain. The etching treatment was given to facilitate EBSD investigations because the sample surface in the finely polished state does not reveal any microstructural details making EBSD investigation extremely difficult. The etching also removes a thin layer of material minimising the effects of mechanical polishing. The degree of topography in Fig. 4.4 seems a little high for EBSD investigations, but this image was taken with the sample tilted 74° towards the detector therefore the appearance of topography is exaggerated. The orientation map in Figure 4.4a shows a clear delineation of 90° domains with a colouring according to the inverse pole figure colour key (Fig. 4.4c).

This map was collected from the domains marked by the polygons in figure 4.4b.

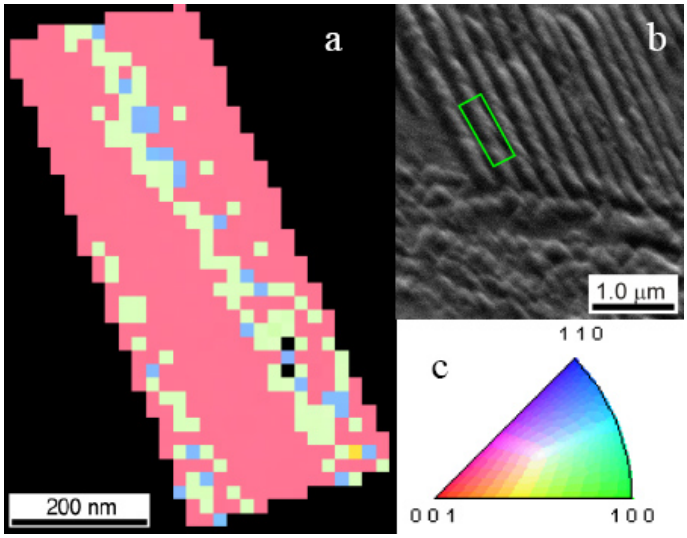

Figure 4.4: (a) EBSD orientation map showing parallel domains in a sample of undoped 50%Zr-50%Ti PZT. (b) Secondary electron image of an area used for mapping. (c) Inverse pole figure colour key.

In spite of the high topography in figure 4.4b, the orientation of 90° domains could be obtained successfully though there were a relatively high number of misindexings in figure 4.4a.

Figure 4.5a is a domain boundary map of the same area as in figure 4.4a; in this map, domain boundaries are highlighted with coloured lines and overlaid on the pattern quality map. The colours represent different angles in the misorientation angle histogram (Fig 4.5b), which present the statistical distributions of the misorientation angles across the domain boundaries. Some of the pixels in the grain boundary map show abrupt colour changes as compared to the adjacent pixels e.g blue and red pixels along the domain boundaries in Fig. 4.5a. Such points occur due to errors in the indexing of the EBSD pattern (perhaps due to poor quality patterns at those points as a result of pattern overlaps at boundaries, surface contamination,damage, or similar) and are not treated as real data. Moreover other random errors are present in all measurements of crystal orientations for a number of reasons including those related to the sample and those related to the orientation measurement system [7,8]. Sample issues may include surface relaxation,

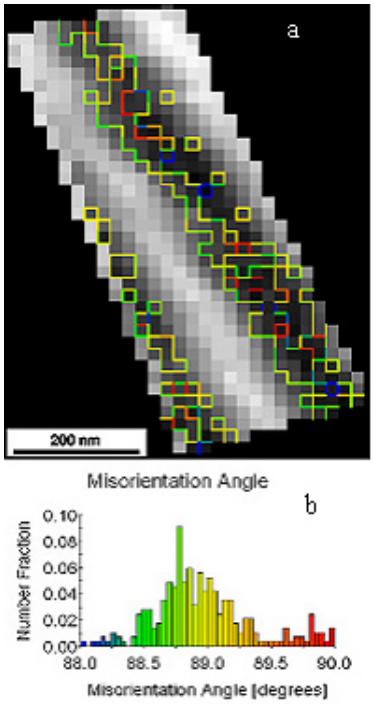

Figure 4.5: (a) and (b) EBSD domain boundary map and misorientation angle histogram from an undoped 50%Zr-50%Ti PZT.

sample bending, and surface layers (including deliberate carbon coating) resulting in loss of pattern definition making the lines harder to detect. Measurement errors are mainly due to diffuseness of the pattern and noise in the CCD camera and its electronics making line location slightly uncertain, also variations in line detection routines can bias the solutions in different directions; a different set of lines detected may result in a slightly different answer. Domain boundary maps with the corresponding histograms have also been obtained from other samples with various compositions (not included in this thesis but published separately [33,35]). Although the mean misorientation is different in each case still the statistical distribution about the mean value is similar proving the reproducibility of the data [35]. Comparing the statistical distribution of misorientation angles obtained from different areas in the same sample has also revealed that the mean value may show small but noticeable variations.

As outlined above, the misorientation angle determined for a region, and specifically

its deviation from 90° reveals key information about the local crystallography in the form of the local c/a ratio and this data is summarised in Table 4.1 for EBSD data from an undoped PZT 50%Zr-50%Ti.

Table 4.1: Misorientation angles and c/a ratios determined using XRD and EBSD methods.

XRD	EBSD	
c/a ratio	90°-δ	Local c/a
	89.00±0.20	1.018±0.004
1.028	88.89±0.22	1.020±0.004
	89.13±0.12	1.015±0.002

4.3 Kikuchi patterns and the calculation of misorientations.

For comparison with the EBSD results, misorientations between parallel domains were also obtained from samples investigated in TEM using Kikuchi patterns. Figure 4.6 shows an example of the automated indexing of a Kikuchi pattern from the TEM. These Kikuchi patterns were indexed using the Euclids Phantasies (EP) software [9]. It was found that provided suitable patterns are recorded with sufficient intensity to allow clear band detection to the edges of the image, unambiguous indexing of the unit cell orientation (not just of the pseudocubic perovskite cell, but also including of the long c-axis direction) was routinely achieved.

A raw TEM-Kikuchi pattern from an undoped PZT 50%Zr-50%Ti sample with the pointer is shown in Figure 4.6a, and the processing steps are then outlined in Figure 4.6b-d. Figure 4.6b shows the result of flattening the high intensity regions and enhancing the low-intensity regions using a logarithmic display of intensity. Figure 4.6c then shows the result of applying an edge-enhancing DCE filter to this logarithmic image; all lines and

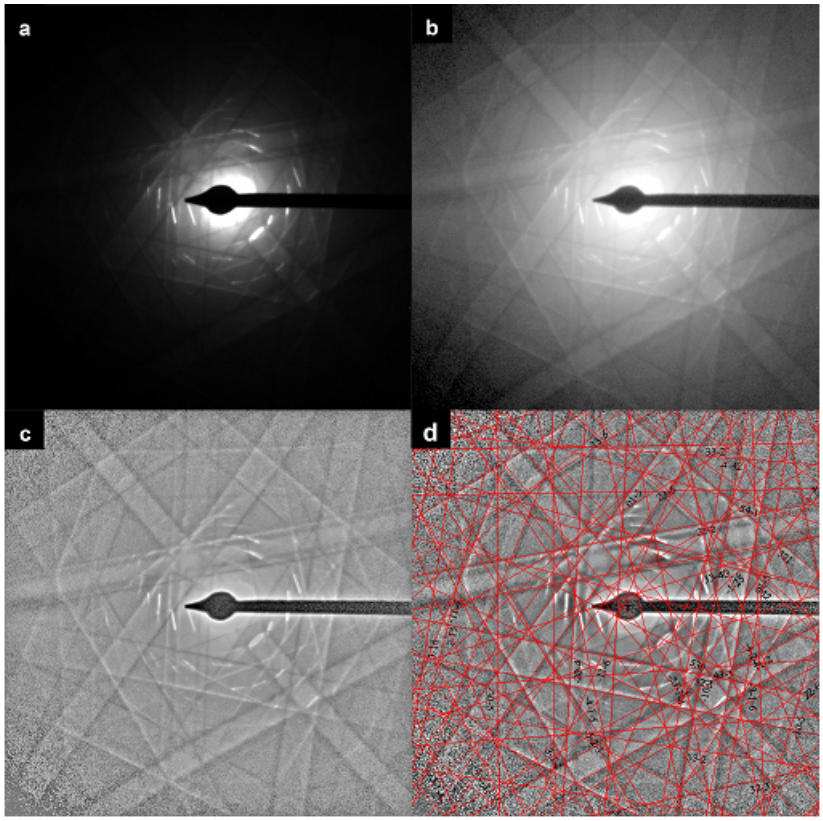

Figure 4.6: TEM Kikuchi pattern from an undoped 50%Zr-50%Ti PZT sample (a) The raw pattern with no contrast adjustment, it is difficult to see much of the pattern when printed. (b) After mapping the intensities onto a log scale to increase the visibility of the low-intensity edge regions. (c) After application of a digital (DCE) filter to enhance the band edges. (d) The same pattern as in (c) with solution lines overlaid.

band edges become much better defined and are thus easier to detect automatically, but the enhancement of noise at the corners of the pattern is also noticeable. Finally, after automatic line detection and fitting of a solution, a display like that in Figure 4.6d is achieved where the predicted Kikuchi lines are overlaid in red on the pattern; a very good match between the experimental pattern and the overlaid solution may be noted. This procedure was used to determine relative orientations at a domain boundary for various PZT samples.

Fig 4.7 shows an area of an undoped 50% Zr/50% Ti PZT sample having parallel domains with the sample oriented such that the domain boundaries are almost edge-on;

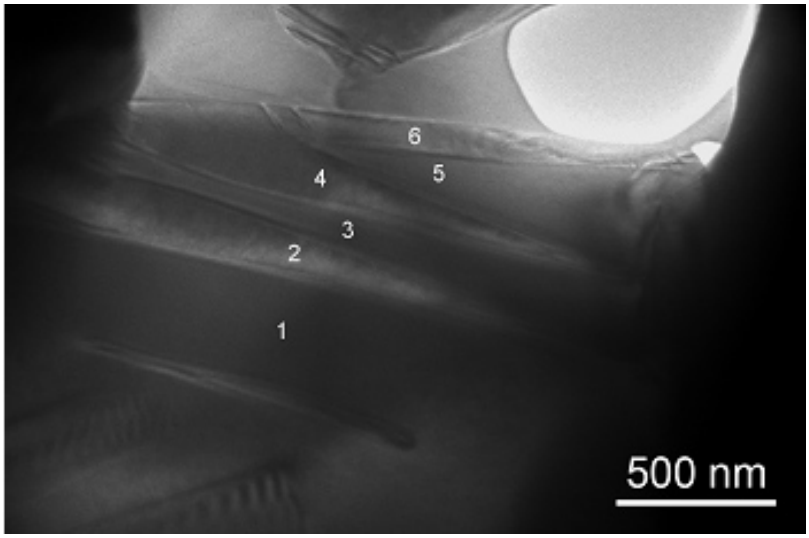

Figure 4.7: Bright field TEM image of domains in undoped 50%Zr-50%Ti PZT with the locations where TEM Kikuchi patterns were recorded.

the locations from where the TEM-Kikuchi patterns were obtained in parallel domains are marked with numbers. The misorientations between adjacent domains are given in Table 4.2.

Table 4.2: Misorientations calculated from the TEM-Kikuchi patterns in the regions marked in Fig. 4.7.

Position pair	1-2	3-4	4-5	5-6
Misorientation (°)	88.23	88.32	88.23	88.39
c/a ratio	1.0314	1.0298	1.0314	1.0285

These values again show a small variability, and this will be discussed in the next section of this chapter. The misorientations calculated from this and similar regions from other samples are given in Table 4.1, converted to equivalent c/a ratios, and compared with EBSD results from the same samples. In order to provide a comparison with global measurements, c/a ratios were also determined from X-ray diffractograms using simple comparison of the (200) and (002) peak positions with zero point correction; these are also summarised in Table 4.3.

Table 4.3: Misorientation angles and c/a ratios determined using XRD and TEM-Kikuchi patterns methods.

XRD	TEM-Kikuchi	
c/a ratio	90°-δ	Local c/a
1.028	88.29±0.08	1.030±0.001

4.4 The effect of small orientation measurement error on misorientation angle measurement.

It has been shown in figure 4.4 section 4.3 in this work, that the misorientations in EBSD tend to show some variation about an average value with a standard deviation typically in the range 0.1-0.2°. The source of this error was investigated further by recording EBSD patterns from a single-crystal silicon wafer (not shown in this work) and reported [35]. The main conclusion of this investigation is that we cannot determine misorientations as well for PZT as for Si. One reason for this will be intrinsic to the materials, since electronic interactions will be more likely in the high-Z PZT resulting in more diffuse scattering with significant energy losses leading to the formation of a more blurred Kikuchi pattern, whereas in the low-Z silicon, phonon interactions resulting in high-angle scattering without significant energy loss will be proportionately more likely, resulting in the formation of a sharper Kikuchi pattern. Another reason for the difference may be related to sample preparation since in the case of PZT the carbon film on the surface will probably cause diffuse scattering and reduce the sharpness of the pattern; although there may be some native oxide on the Si surface, the effect is probably less. Orientation noise also arises in TEM Kikuchi pattern measurements, as a consequence of slight variation in the set of bands detected in a pattern: this may arise as a consequence of contrast, orientation or thickness changes, and sometimes slight changes to the software settings used for band detection are necessary where the standard settings give a match which clearly does not fit some of the outlying lines. Such changes can just have the consequence of finding a crystallographically equivalent solution to the original solution but

can also introduce small misorientations. An experiment was performed where the band detection parameters were adjusted slightly to produce 6 different indexings of the same pattern, all of which appeared by eye to fit the bands very well. The misorientations between all of these orientation determinations were then calculated to give 15 different misorientation values. From these, a mean misorientation angle of 0.09° (or median of 0.08°) with all values <0.2° was calculated, suggesting that the instrumental accuracy of orientation determination from TEM-Kikuchi patterns is better than that for EBSD [35]. The other main source of error in orientation measurements in the TEM will arise from the bending of the thin TEM specimens; this may be measured by recording Kikuchi patterns from different areas within the same domain by simply translating the specimen without tilting, or equivalently, translating the beam without tilting (which requires a carefully aligned microscope). Current measurements suggest that closely separated areas may have misorientations of less than 0.2°, but more widely separated areas often have misorientations greater than 0.5°; the situation is especially bad for the thinner areas adjacent to holes in the ion-beam-thinned specimens, probably due to stress relaxation in these very thin areas. This would suggest that the main limitation to accurate misorientation measurement in the TEM arises from sample bending and not from indexing accuracy. To minimise the effect of this bending on the results two steps can be taken: firstly to only work with data from relatively thick areas of the specimen, and secondly to use the smallest possible step size between spots used for the analysis of the relative orientations between features in a sample. TEM investigations of un-doped PZT 50% Zr/50% Ti has shown that in relatively thick TEM samples where stress release and sample bending were minimised, the c/a ratio was found to be more or less the same over large distance (Table 4.2). The important question on "90°"domains is how these orientation variations within a single crystal as a result of indexing and specimen preparation issues affect the misorientation measurements across domain boundaries. Fortunately, the effects of a small misorientation error on a misorientation measurement have already been calculated [7]. According to these calculations, if there is a random misorientation from a measurement error, it will affect the measured misorientation angle in different

ways depending on the relative orientation of the real and the random misorientation axes; a random distribution of misorientation axes for a fixed error angle, δ, will give a cosine distribution of angles about the true misorientation but will not shift the centre of the distribution significantly for high misorientation angles. In reality, just a fixed error angle δ is not seen but a distribution approximating to a Rayleigh distribution, as previously suggested [8]. Figure 4.8 shows a misorientation distribution graph for a 90° domain boundary in the PZT with a cosine distribution fitted to this distribution. Most of the EBSD orientation maps give misorientation angle histograms which can be approximately fitted by a cosine graph, and in many cases the standard deviations on the misorientation angles listed in Tables 4.1 and 4.3 compare well with the expectation of $\delta/\sqrt{\pi} \approx 0.09°$, with some listed errors such as 0.06°, 0.08°, and 0.12°. In other cases, larger errors are seen, and there could be a number of reasons for this including poorer pattern quality due to microscope setup or specimen preparation related factors, also in one case, it appeared possible that the distribution was bimodal with two different boundaries having slightly different misorientations. Hence it can be inferred that the statistical distribution of misorientation angles along a domain boundary, as shown in Fig. 4.4, is caused by orientation noise rather than real crystallographic or compositional variations along a domain boundary.

However for the same sample a relative shift of the mean value of statistical distribution of misorientation angles obtained from different sample areas may well indicate that the c/a ratio is not constant throughout the sample. Analysing the results for the undoped 50% Zr / 50% Ti samples, however, some larger discrepancies may be noted for both TEM-Kikuchi and EBSD measurements. These may well indicate local variations in *c/a* ratios from the bulk average as a result of local compositional inhomogeneities, but more work would be required to confirm whether or not real compositional and crystallographic heterogeneities are really present in these materials. It is also clear that if the orientation noise could be reduced, we would have a better chance of unambiguously detecting small changes in local crystallography. To detect smaller changes in composition and thus c/a we would need to have more accurate methods for orientation measure-

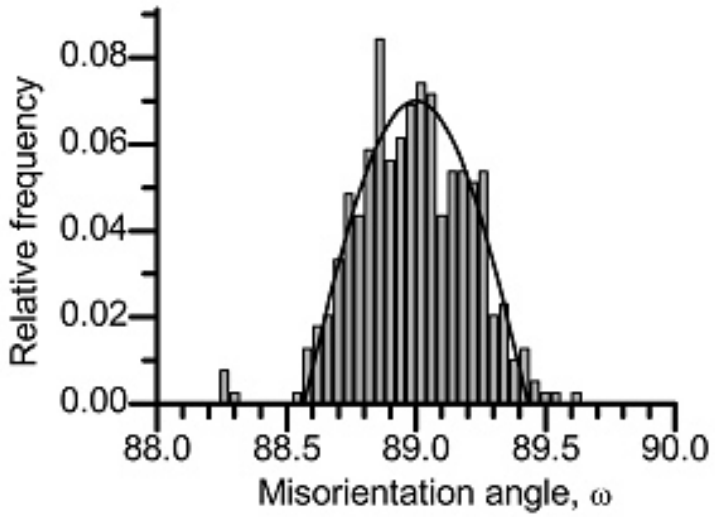

Figure 4.8: Misorientation distribution graph of 90° domain boundary from undoped 50%Zr-50%Ti PZT with a cosine distribution fitted to this distribution.

ment, especially in EBSD. There are a number of things that can be done in this area. Firstly, improved pattern quality (better signal to noise) would help, and in this respect a better EBSD camera would be a significant help. Secondly, better accuracy of orientation determination using pattern matching methods rather than Hough transform based methods has been shown already [7], and these could be explored in future work. Similarly, care will need to be taken with TEM data to maximise accuracy and thus maximise our chances of being able to detect smaller lattice parameter changes.

Bibliography

[1] Farooq, M.U., Villaurrutia, R., MacLaren, I., Kungl, H., Hoffmann, M.J., Fundenberger, J-J., and Bouzy, E., J. of Phys.: Conference Series, 126, 012012, (2008).

[2] MacLaren, I., Schmitt, L.A., Fuess, H., Kungl, H., and Hoffmann, M.J., J. Appl. Phys. 97, 094102 (2005).

[3] Fousek, J., and Janovec, C., J. Appl. Phys. 40, 135 (1969).

[4] Randall, C.A., Barber, D.J., and Whatmore, R.W., J. of Mat. Sci. 22, 925-931, (1987).

[5] Sapriel, J., Phys. Rev. B., 12, 5128 (1975).

[6] Stemmer, S., Streiffer, S.K., Ernst, F., and Ruhle, M., Philos. Mag. A, 71, 713 (1995).

[7] Bate, P.S., Knutsen, R.D., Brough, I., and Humphreys, F.J., J. of Microscopy, 220, 36-46, (2005).

[8] Godfrey, A., Wu, G.L. and Liu, Q., Mater. Sci. Forum, 408-412, 221-226, (2002).

[9] Fundenberger, J.J., Morawiec, A., Bouzy, E., and Lecomte, J.S., Ultramicroscopy, 96, 127-137, (2003).

[10] Artl, G., and Sasko, J., J. Appl. Phys. 51, 4956, (1980).

[11] Artl, G., J. Mater. Sci. 25, 2655, (1990).

[12] Pertsev, N.A., and Artl, G., Ferroelectrics, 123, 27, (1991).

[13] Pertsev, N.A., and Artl, G., Ferroelectrics, 132, 27, (1992).

[14] Burnett, T.L., Comyn, T.P., and Bell, A.J., J. Neutron Res., 12, 39, (2004).

[15] Burnett, T.L., Comyn, T.P., and Bell, A.J., J. Cryst. Growth., 285, 156, (2005).

[16] Hammer, M., and Hoffmann, M.J., J. Am. Ceram., 81, 3277, (1998).

[17] Burnett, T.L., Comyn, T.P., Merson, E., Bell, A.J., Mingard, K., Hegarty, T., and Cain, M., IEEE Trans. Ultrason. Ferroelectr. Freq. Control,. 55, 957, (2008).

[18] Godfrey, A., Wu, G.L., and Liu, Q., Sci. Forum, 221, 408, (2002).

[19] Fedulov, S.A., Venevtsev, Yu, N., Zhdanov, G.S., Smazhevskaya, E.G., and Rez, I.S., Kristallografiya, 7, 77, (1962).

[20] Mori, T., Oliver, E.C., Daymond, M.R., and Withers, P.J., Neutron Res., 12, 39, (2004).

[21] Schmitt, L.A., Schonau, K.A., Theissmann, R., Fuess, H., Kungl, H., and Hoffmann, M.J., J. Appl. Phys. 101, 074107,(2007).

[22] Jimenez, A., and Vicente, J.M., J. Phys. D:Appl. Phys., 33, 1525, (2000).

[23] Kounga Nijiwa, A.B., Aulbach, E., Rodel, J., Turner, S.L., Comyn, T.P., and Bell, A.J., J. Am. Ceram., 89, 1761, (2006).

[24] Wilkinson, A.J., Meaden, G., and Dingley, D.J., Mater. Sci. Technol., 22, 1271, (2006).

[25] Xinhua, Z., Jianming, Z., Shunhua, Z., Qi, L., and Naiben, M., J. Appl. Phys, 89, 9, (2001).

[26] Damjanovic D., Rep. Prog. Phys. 61, 1267-1324, (1998).

[27] Jona, F., and Shirane, G., Ferroelectric Crystals, Monographs on Solid State Physics, Pergamon Press, Oxford, (1962).

[28] Wright, S., and Nowell, M., Microsc. Microanal., 12, 72-84, (2006).

[29] Reszat, J., Glazounov, A., and Hoffmann, M., J. Eur. Ceram. Soc., 21, 1349-1352, (2001).

[30] Small, J.A., Michael, J.R., and Bright, D.S., J. of Microscopy., 206, 170, (2002).

[31] Koblischka-Veneva, A., and Mucklich, F., Crystal Engineering., 5, 235-242, (2002).

[32] Shao-Ju Shih, Myung-Beom Park, and Cockayne D.J.H., Journal of Microscopy, 227, (2007).

[33] Farooq, M.U., Villaurrutia, R., MacLaren, I., Burnett, T.L., Comyn, T.P.,Bell, A.J., Kungl, H., and Hoffmann, M.J. , J. Appl. Phys., 104, 024111, (2008).

[34] Li-chang, Yang., Dumler, I., and Wayman, C.M., Mat. Chem. and Phys., 36, 282-288, (1994).

[35] Farooq, M.U., Villaurrutia, R., MacLaren, I., Kungl, H., Hoffmann, M.J., Fundenberger, J.-J. and Bouzy, E., J. of Microscopy, 230, 445, (2008).

Chapter 5

Understanding incommensurate phases on the ferroelectric-antiferroelectric domain boundary in Lanthanum doped Zr-rich PZT

Lead zirconate titanate ceramics with a Zr:Ti ratio of 90:10 and doped with 2-4% La display an incommensurate antiferroelectric phase. In order to understand the different phase transformations associated with these compositions, a detailed knowledge of the domain structure and the nanostructure of the incommensurate antiferroelectric phase is an indispensable prerequisite. The experiments carried out in these ceramics are based on TEM imaging and diffraction techniques. This chapter explores in detail the domain structures and the nanostructures contained within in one composition range which demonstrates the incommensurate phases of interest: La-doped PZT with La:Zr:Ti ratios of 2:90:10, 3:90:10 and 4:90:10. Section 5.1 is a revision of the basics on modulated structures and incommensurate phases, aiming to give the background needed in this analysis. Section 5.2 deals with the general features of the PLZT compositions used in

these experiments including the analysis of the antiferroelectric-ferroelectric transition in PLZT. Section 5.3 comprises the TEM analysis of the different features found in these compositions of PLZT.

5.1 Modulated structures and incommensurate phases

The crystal structure of many oxides is composed of crystallographic shear phases (CS) built from slabs of a single pattern structure, that can be joined in such a way to produce a change in the overall composition of the solid [17]. The diffraction patterns of oxides containing CS planes resemble these of the original structure; nonetheless, the CS planes impose a new set of diffraction conditions. Due to the periodic character of the modulation, additional sharp peaks appear in the diffraction pattern; just as the Bragg reflections produced by a three-dimensional crystal result from the periodic terms in the structure factor equation [23]. Figure 5.1a shows a typical selected area diffraction pattern of a cubic oxide taken with the beam parallel to [001]. Suppose that the crystal contains parallel but disordered (210) CS planes. The diffraction pattern will be similar to the one of the original structure, but additional diffracted intensity will now be streaked between the spots along the 210 direction. As the CS planes become ordered, the streaks begin to show maxima and minima; thus, the CS planes will produce sharp spots when perfectly ordered (figure 5.1b).

Such additional Bragg reflections, cannot be indexed with three indices hkl; instead, 3 + d indices are required (d = 1, 2 or 3). The necessity for using four or more indices must be understood as a loss of periodicity in three dimensions [26,27]. These additional peaks are referred to as satellite reflections and usually they are weaker than the main reflections. The satellite reflections can lie parallel to one reciprocal axis, but they do not have to [24]. It should be emphasized that modulated structures are not disordered but have long-range order which is reflected in those discrete additional peaks rather than in diffuse streaks [25]. Structures that show extra reflections such as the ones seen in

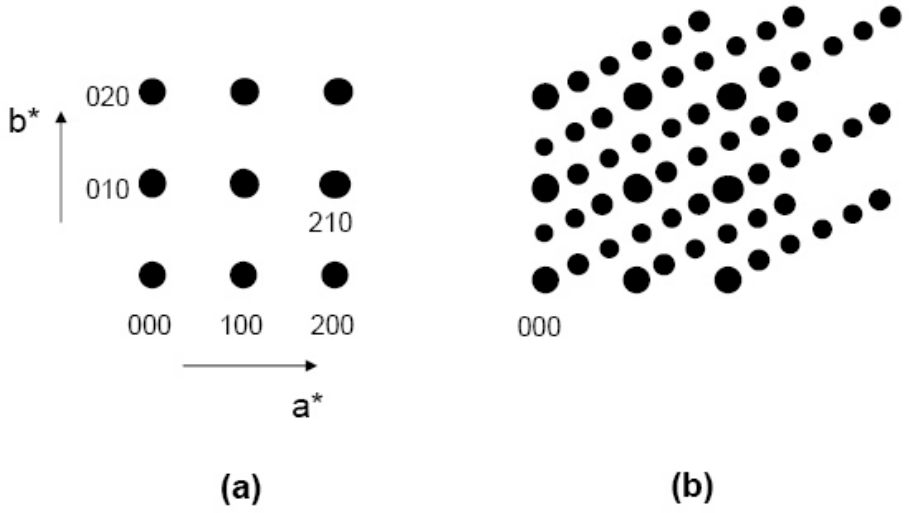

Figure 5.1: Diffraction patterns of crystals containing *CS* planes. a) idealised diffraction pattern from a cubic oxide, b) containing ordered (210) *CS* planes. (after Tilley et. al., [17])

figure 5.1b are known as modulated structures and the extra reflections are known as superlattice reflections. These modulated structures can be described by a modulation function. Modulation functions are wave functions characterised by a wave vector q, which specifies the direction of the wave and the wavelength λ. However, it is found that the superlattice spots do not fit in with the parent reflections, either in spacing or in both the spacing and the direction of the rows. The diffraction patterns and the structures giving rise to this feature are said to be incommensurate. The diffraction pattern of a normal crystal is characterised by an array of spots separated by a distance $1/a = a^*$ that arise from the pattern structure, together with a set of commensurate superlattice reflections that arise as a consequence of the additional ordering. In this case the spot spacing is$1/na = a^*/n$, where n is an integer (figure 5.2a). In modulated structures, the modulation can be in the position of the atoms, called a displacive modulation (figure 5.2b). Displacive modulations sometimes occur when a crystal structure is transformed from one stable structure to another as a result of a change in temperature. Displacive orderings can be commensurate or incommensurate, just as with other types of ordering

such as chemical, charge or magnetic ordering. Alternatively, the modulation can be in the occupancy of a site, called chemical ordering modulation. Figure 5.2a is an example of a commensurate chemical ordering modulation where the diffraction pattern shows spot reflections separated a distance $1/na = a^*/n$, where n is a rational number. Whereas figure 5.2b is an example of displacive incommensurate modulation where the diffraction pattern shows spots separated a distance $1/ka = a^*/k$ where k is an irrational number and $k = \lambda$. In many solids local properties such as electric polarisation and atomic position are found to be modulated with a periodicity q_I which is incommensurate with the periodicity q_p of the underlying lattice [16]. In compounds with partial occupancies of atomic sites, vacancy ordering may lead to incommensurabily-modulated structures. Modulations involving the alternate occupancy of a single crystallographic site with atoms of chemically different elements are defined in the same way as vacancy ordering.

As the spacing between the strakes is $1/nd_{hkl}$, where n is an integer, they fit perfectly into the reciprocal lattice of the crystal and are said to be commensurate with it. Following this idea, we can now describe the position of the atoms in a 1-D lattice as:

$$x_n = na \tag{5.1}$$

Where a is the 1-D lattice constant and n is an integer. If we considered a monatomic basis in which the atoms sit on the lattice points defined above, then, the displacements of the original atoms to the new positions X_n will be given by:

$$X_n = x_n + f\sin(\frac{2\pi}{a}qx_n) = x_n + f\sin(2\pi nq) \tag{5.2}$$

Where f is the modulation amplitude and q describes the modulation wavelength. If q is a non-zero rational number, the new structure is also periodic but with a larger unit cell a/q. This structure is referred as a commensurate superlattice. If q is an irrational number, such as $1/\sqrt{2}$, then the structure does not posses a traditional periodicity but a quasi-periodicity. Such structures are known as incommensurate superlattices [18]. Figures 5.3a and 5.3b illustrate the transitions of a periodic 1-D lattice, with lattice constant $a\prime$, to a commensurate superlattice with q=1/4 and 1/6 respectively ($f = 1/2$).

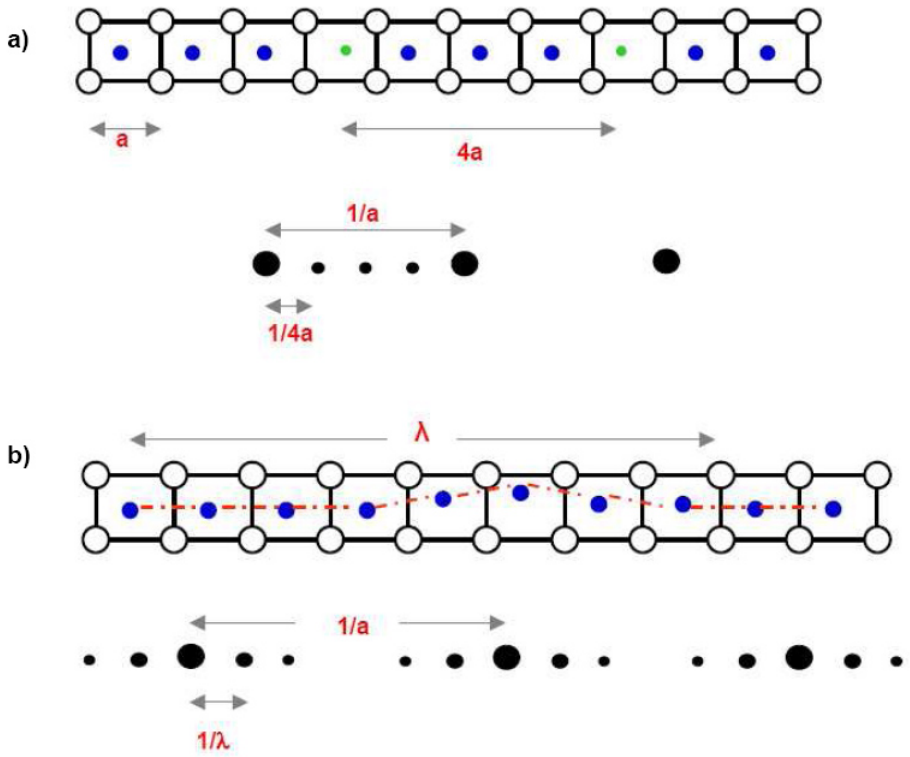

Figure 5.2: Schematic representations of normal and modulated structures and diffraction patterns. a) a normal superlattice, formed by the repetition of atomic substitution, and part of the diffraction pattern showing a commensurate modulation; b) a crystal showing a displacive modulation of the anion positions, and part of the diffraction pattern showing the incommensurate modulated wavelength (after Tilley, [17]).

Figures 5.3c and 5.3d show a similar transformation with (f=1/4), but $q = 1/\sqrt{2}$ and $q = 1/\sqrt{3}$ respectively. As the *sin* function is periodic, but with an irrational period, the modulated lattice is incommensurate with respect to the first lattice.

Incommensurate modulated phases are often found in inorganic solids. In many cases, the transition to the modulated structure corresponds to a change of certain physical properties [20]. Hence it is essential to know the structure of incommensurate phases in order to understand the mechanism of the transition and properties in the modulated state. An example of the diffraction pattern of an incommensurate modulated structure is shown in figure 5.4. This figure shows a [001] diffraction pattern taken from a single domain of a lanthanum doped PZT ceramic of 3:90:10 composition. The weak satellite

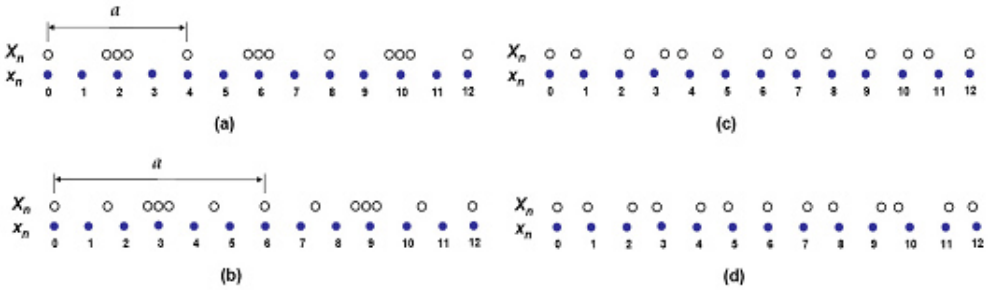

Figure 5.3: Periodic 1-D lattice transitions (a) with $q = 1/4$ and f=1/2 (b) with q=1/6 f=1/2 (c) with $q = 1/\sqrt{2}$ and f=1/4 (d) with $q = 1/\sqrt{3}$ and f=1/4 (after DeGraef, [18])

spots around the principal reflections indicate long period ordering of the crystal structure and are due to the modulation of the basic perovskite structure. The periodicity of such satellite spots was about 22.6$\mathring{A}$, about 7.7 ± 0.2 longer than the (110) spacings. These features are evidence of the incommensurability of this composition.

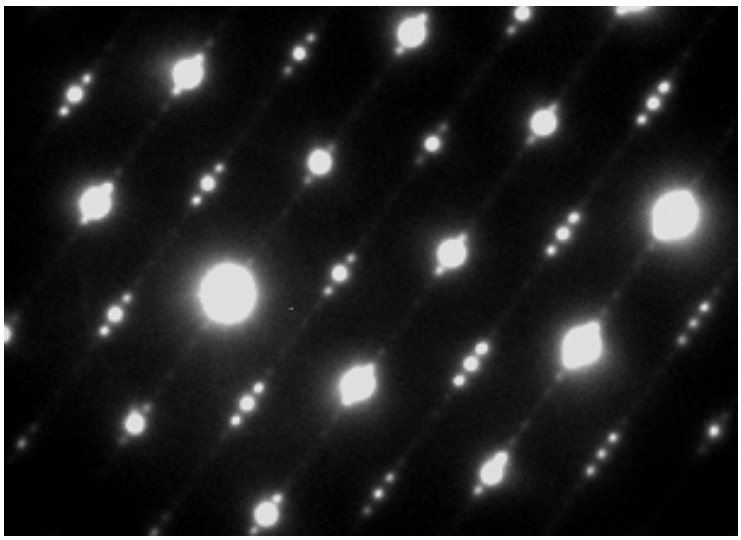

Figure 5.4: [001] Selected area diffraction pattern from a single domain of a Lanthanum doped PZT ceramic (3:90:10 composition)

5.1.1 Lanthanum doped lead-rich PZT ceramics

A variety of PZT-based materials have been developed to meet different specific applications via different compositional modifications. In La-substituted $Pb_{1-x}La_x(Zr_{1-y}Ti_y)O_3$, the antiferroelectric incommensurate phase has been reported to exist between the rhombohedral ferroelectric and antiferroelectric phases. It has been shown that increasing La content with Zr:Ti ratio of 90:10 increases the stability of the antiferroelectric phase due to a disruption of the long-range dipolar interaction [9], suppressing the ferroelectric state, which has less effect on the antiferroelectric state at low La contents (2,3 and 4 at.%). At high La contents ($>$ 4 at.%), the disruption is sufficient to additionally destabilise the antiferroelectric state resulting in the onset of relaxor behaviour [43]. These features have been extensively valuable for electro-optical applications of transparent ceramics [43-45]. Materials with promising characteristics for energy storage applications are those exhibiting antiferroelectric behaviour [46-48]. As functional materials, these antiferroelectric materials are commonly characterised by either a low dielectric permittivity with a field induced transition to a ferroelectric state at a critical electric field (named as threshold field), as is the case of the $PbZrO_3$ system, [13] or a relatively high dielectric permittivity with a decreased electric field strength dependence, as is the case of the lanthanum modified lead zirconate titanate (PLZT) system [49,50]. The phase transitions between the AFE and FE states have been traditionally considered as the object of intensive studies due to the wide range of applications in the electronic industry [51,52] . Recent investigations have led to the increasing interest in the study of such transitions and related phenomena because of the observed coexistence between the antiferroelectric and ferroelectric phases in perovskite structure materials [53-56]. The antiferroelectric-ferroelectric phase transition can occur spontaneously due to several factors, such as a change in the stress configuration promoted by external mechanical driving fields as an increase in the amplitude of the applied ac electric field and/or by thermal changes [13]. It is known that in ferroelectric systems, the ferroelectric domain structure is characterised by a large spontaneous electrical polarisation, whereas classical antiferroelectrics are frequently centrosymmetric materials. Thus, a ferroelectric state can be

induced in antiferroelectric systems with compositions near to the AFE-FE phase boundary (where both phases coexist) by applying high electric field levels. Otherwise, taking into account that antiferroelectric systems are more compact (from the atomic arrangement point of view), ferroelectric compositions close to the AFE-FE phase boundary can be transformed into antiferroelectric state by applying a hydrostatic pressure. Lanthanum modified lead zirconate titanate (PLZT) has been found to show a dispersive behaviour for both rhombohedral and tetragonal phases, as well as to increase the stability range of the antiferroelectric orthorhombic phase in the Zr-rich side of the phase diagram [13]. The corresponding phase diagram at room temperature shows regions where ferroelectric and antiferroelectric phases coexist, and thus both states must be similar free energy values. PLZT compositions close to the AFE-FE phase boundary are well known systems because of the phase switching characteristic, than is to say, the electric field induced AFE-FE phase transformation takes place. It is known that in lanthanum modified PZT ceramics, most of the lanthanum ions locate into the A-sites of the perovskite structure, replacing the lead cations [22]. The perovskite structure (ABO_3) can be considered as a network of BO_6 octahedron, where the B- and the A-site cations are located inside and in the neighbouring of the octahedral, respectively. The stability of the long-range ferroelectric state is believe to be suppressed by decoupling effects caused by the incorporation of lanthanum ions into the A-sites, which is revealed by the decreasing of the ferroelectric-paraelectric transition temperature, when the lanthanum concentration increases. By considering that the addition of small lanthanum concentrations leads to a decrease in the long-range interactions, reducing the stability of the ferroelectric phase, it is expected a reduction of the observed "average" T_m value. However, it would be very difficult for small concentration of the additive cation to suppress the short-range nature of the interactions in the antiferroelectric state. Thus, for the samples studied in this chapter, lanthanum impurities may induce a competition between the antiferroelectric and ferroelectric ordering due to the disruption of long-range dipolar interactions. The Zr-rich end of the $Pb(Zr,Ti)O_3$ (PZT) phase diagram (figure 5.5) is a fascinating region for study where ferroelectric and antiferroelectric ordering schemes compete. According

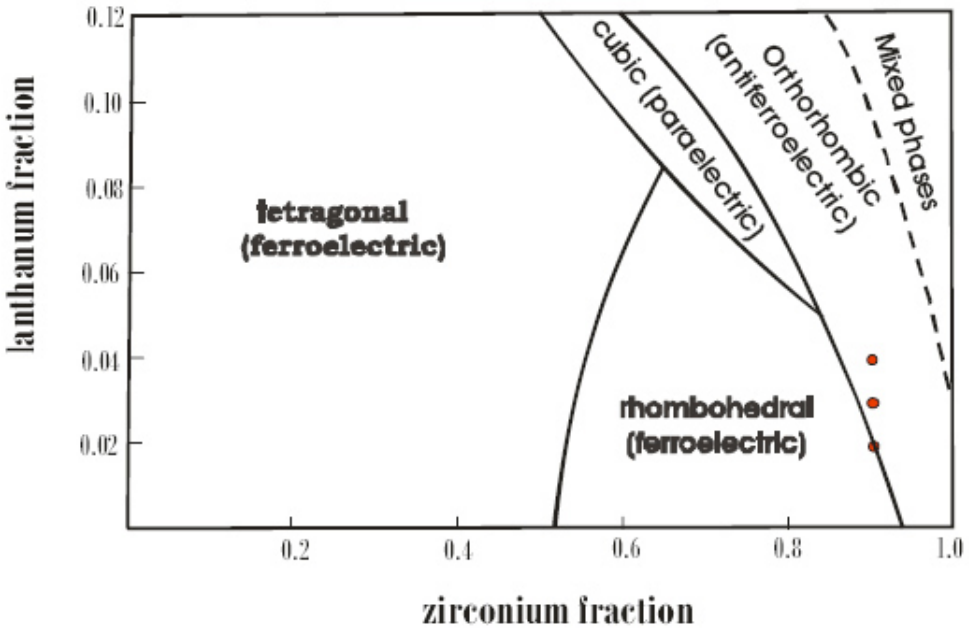

Figure 5.5: Phase diagram of the Lanthanum doped PZT ceramics, showing the 2:90:10, 3:90:10 and 4:90:10 compositions studied in this work (after Jaffe, Cook and Jaffe, [21])

to the classic phase diagram of Jaffe et al. [21], the boundary between the orthorhombic antiferroelectric $PbZrO_3$ phase and the rhombohedral PZT phase lies at a Zr:Ti ratio of 94:6. Dai et al. [9] in their classic study showed that PZT with a Zr:Ti ratio of 90:10 can be driven through a transition from the ferroelectric phase to an antiferroelectric phase by doping with a few at.% of La. Structurally, this result in the appearance of some unusual satellite spots in selected area diffraction patterns: these sit along 110 directions of the primitive cubic reciprocal lattice and were interpreted as evidence for a long-period ordered incommensurate antiferroelectric structure. An intriguing feature of this phase is the appearance of a streaked structure within the domains associated with the incommensurate ordering. Nonetheless, the origin of this streaking is not investigated in detail in this work. In this work, the micro- and nano-structure of La-doped PZT with La:Zr:Ti ratios showed in figure 5.5 of 2:90:10, 3:90:10 and 4:90:10 were studied, correlating this with electrical measurements on the same specimens in order to have a better understanding of the phases present and their microstructures.

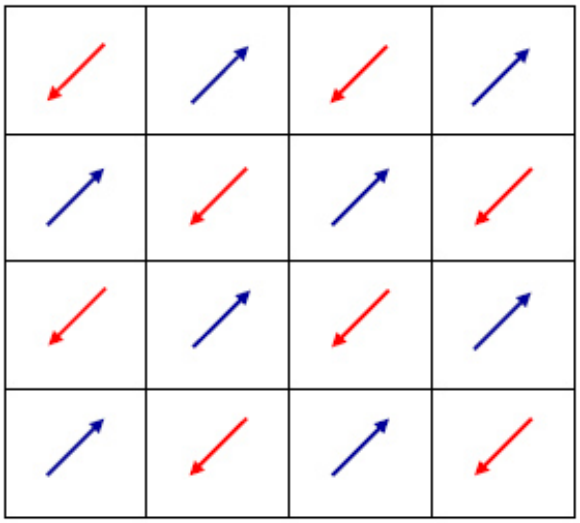

Figure 5.6: Configuration arrangement of dipoles in antiferroelectric compounds (after Reaney, [19])

5.1.2 Domain boundaries in antiferroelectric PLZT

As shown in figure 5.6, antiferroelectric perovskites have dipoles arranged in an antiparallel configuration parallel to ⟨011⟩ (viewed here in a ⟨100⟩ projection). The dipoles are equal in magnitude but opposite in sense and consequently, there is no net polarisation within a unit cell nor within a domain [19]. In that sense, the antiferroelectric phase configuration differs from the paraelectric and ferroelectric ones as discussed in chapter 2.

The prototypic orthorhombic antiferroelectric is PbZrO_3, which has a unit cell roughly consisting of $a_{ortho} \sim \sqrt{2}a_{cubic}, b_{ortho} \sim 2\sqrt{2}a_{cubic}, c_{ortho} \sim 2a_{cubic}$ [3,4], this structure has polarisation along the a_{ortho} direction (the primitive $[1\bar{1}0]$ direction). In the ab plane there is very little distortion from the square shape of this plane in the cubic perovskite cell; calculating primitive cell parameters back from the orthorhombic parameters gives a difference between the a and b directions of about 1 part in 1000. In contrast, to this, the c axis is noticeably shorter than the primitive cell parameters in the ab plane with $a_{primitive}/c_{primitive}$ calculated as ~ 1.012 from published cell parameters [3]; for this reason in early work it was concluded that $PbZrO_3$ was tetragonal [5]. It was expected

that the incommensurate phases studied here were also similar in being pseudotetragonal, and also with an ordering consisting of atomic shifts in the (001) plane. Because of the uncertainty about the precise size of the unit cell in the incommensurate phase, and because this can vary from one location to another within the same sample, we have chosen to express crystallographic indices with respect to a primitive pseudotetragonal unit cell, unless stated otherwise. It has previously been shown that the orthorhombic AFE phase of $PbZrO_3$ forms three major kinds of domain boundaries: 60°, 90°, and 180° [6]. The 60° and 90° domain boundaries are depicted schematically in Figure 5.7.

The 90° domain boundary is perhaps the easiest to understand and occurs when the polarisation direction is switched by 90° in the (001) plane from being parallel to $[1\bar{1}0]_{primitive}$ to parallel to $[110]_{primitive}$. Ideally, to avoid head-to-head polarisation, such boundaries would sit on $\{100\}_{primitive}$ planes and this has been shown experimentally in both $PbZrO_3$ [6], as well as in an incommensurate phase in a Nb,Sn modified $Pb(Zr,Ti)O_3$ [7]. The 60° domain boundary consists of a 120° rotation of the crystal structure about a $\langle 111\rangle_{primitive}$ axis, this has the effect of rotating a_{ortho}, the polarisation direction, by 60°, and the long b axis of the orthorhombic structure by 120°. Such boundaries are sited ideally on $\{101\}_{primitive}$ planes. The additional effect of rotating by 120° about $\langle 111\rangle_{primitive}$ is that a cyclic permutation of $a_{primitive}$, $b_{primitive}$ and $c_{primitive}$ results. Since $c_{primitive}$ is slightly shorter than the other two parameters, in terms of the primitive pseudotetragonal cell, the fit together at the boundary will be similar to that of tetragonal ferroelectrics at 90°-α as shown in Figure 1c. This means that the primitive cell will be slightly rotated about $\langle 010\rangle_{primitive}$ across the boundary by a small angle given by:

$$\alpha = 90^\circ - 2\tan^{-1}(a/c) \tag{5.3}$$

For $a/c = 1.012$ this gives a rotation of 0.68°, and this rotation angle is very sensitive to variations in a/c. Therefore, careful measurements of misorientations at 60° domain boundaries can be used to reveal the local crystallography, much as we have done previously for tetragonal PZT [1].

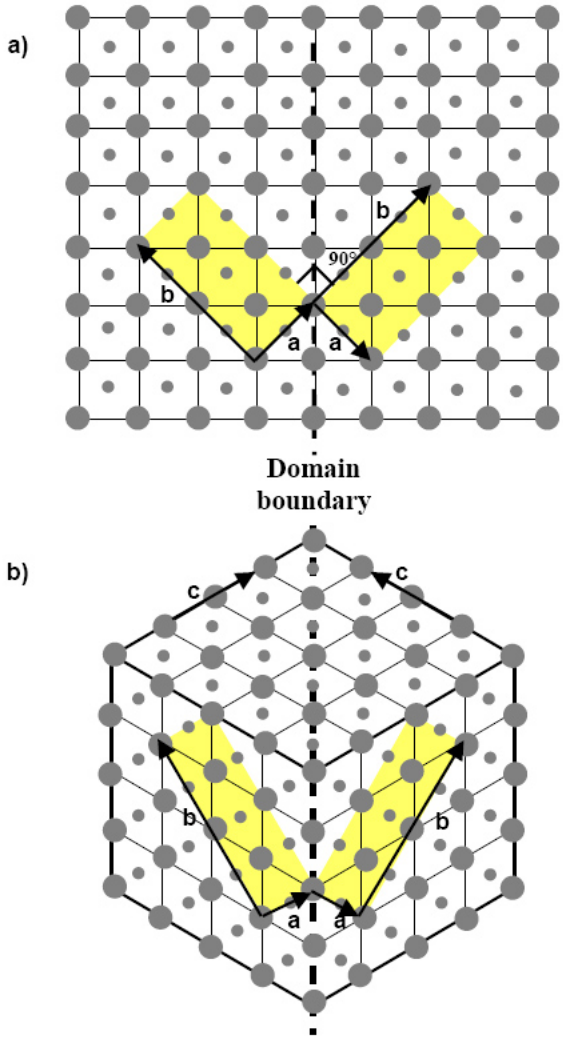

Figure 5.7: Schematic diagrams of domain boundary structure in orthorhombic ferroelectrics. a)90° domain boundary (c-axis normal to the page); b) 60° domain boundary. [after Tanaka, Saito and Suzuki, [6]

5.2 Analysis of PLZT by Transmission Electron Microscopy

5.2.1 General features of the microstructure and nanostructure

Samples with compositions given by $(Pb_{1-x}La_x)(Zr_{0.9}Ti_{0.1})_{1-x/4}O_3$ where x = 2, 3 and 4% were made, and prepared for TEM analysis, according to the methods explained in chapter 4. Transmission electron microscopy was performed using either a FEI Tecnai T20 TEM operated at 200 kV or a FEI Tecnai TF20 TEM operated at 200 kV. Figure 5.8 shows images of one grain recorded under a variety of diffraction conditions. Under bright field illumination and in strong beam dark field conditions, the dominant contrast is typical TEM contrast of bend contours and domain boundaries, as exemplified by the image of Figure 5.8a. Whilst individual domain boundaries are rarely completely straight, and wedge shaped domains are common, most domain boundaries show a strong tendency towards one specific plane. Studies of domain boundaries in all samples studied show that every one had a projected direction consistent with a $\{101\}_p$ plane. This is exemplified in Figure 5.8b where the boundaries running almost horizontal are almost edge-on and perpendicular to the $[01\bar{1}]_p$ vector.

If the sample is tilted a few degrees away from a strong diffraction condition so that the diffraction contrast from the domains no longer dominates, a much weaker nanoscale contrast becomes apparent within the domains as shown in Figure 5.8b and 5.8c. These two images were taken at similar, but slightly different tilt values and using different reflections. This contrast is always associated with the appearance of satellite spots around the diffraction spot used for imaging and the streaking in the nanostructure is always perpendicular to the direction of the satellite spots (see Figure 5.9). Similar results have also been found for the grain of figure 5.8d and other grains in samples in all compositions. It is important to note that the contrast achieved in all the dark field images showing the nanostructure would be difficult to achieve using the traditional method of aligning a selected spot into an objective aperture in diffraction mode, and

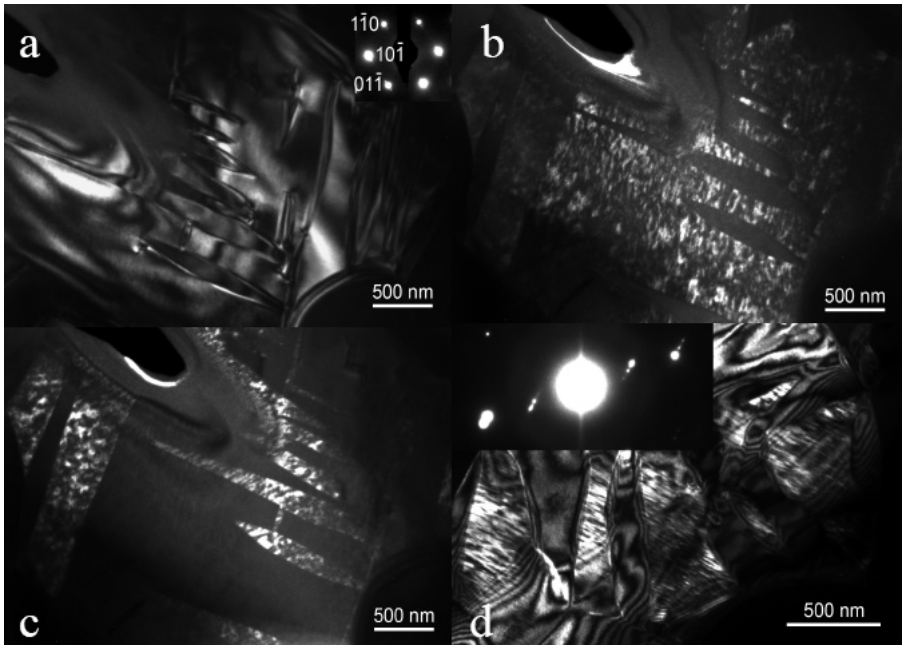

Figure 5.8: Dark field TEM of the domain structure in a 2:90:10 specimen; a) Strong beam dark field image recorded at an orientation near to a $\langle 111 \rangle_p$ zone axis using a 110 diffraction condition showing domain contrast only; b) weaker beam dark field image achieved by tilting the specimen about 3 degrees away from the 110 Kikuchi band showing nanostructure in one set of domains; c) a similar weak beam diffraction image achieved by tilting away from a different 110 Kikuchi band by a few degrees showing nanostructure in a complementary set of domains; d) a different grain in this composition showing the relationship between the nanostructure and the satellite spots; in this case the orientation was closer to a strong diffraction condition and both conventional domain contrast as well as nanostructure may be seen.

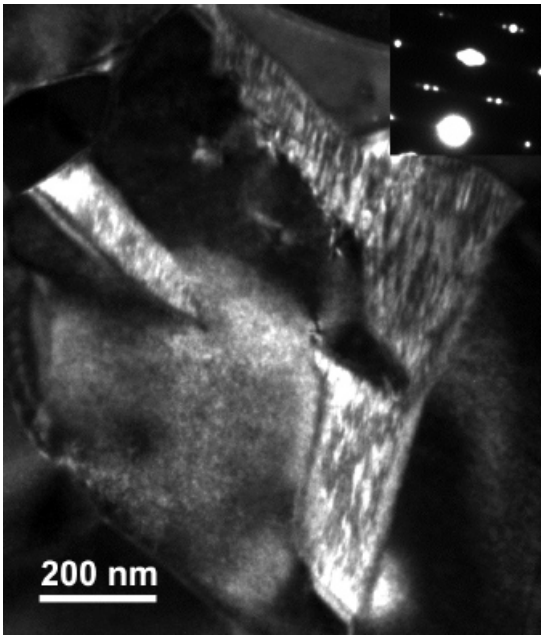

Figure 5.9: Dark field TEM image of an area with a streaked nanostructure together with part of the selected area diffraction from this area (inset). The perpendicularity of the satellite spots and the nanostructure streaking is clearly visible.

is more easily achieved by searching for the nanostructure contrast in image mode by moving the dark field tilts in a conical (r,theta) setting until appropriate contrast is seen. The reflections giving rise to the contrast of interest can then be identified using selected diffraction.

The satellite spots tend to lie along 110-type directions in diffraction patterns, as previously noted by other workers[7,9-11], and have been noted in $\langle 001 \rangle$, $\langle 111 \rangle$, $\langle 210 \rangle$ zone axis diffraction patterns, among others; some examples are shown in figures 5.10 and 5.11. Each domain contains just one direction along which the satellite spots are seen, as illustrated by Figure 5.10a, which was recorded from a single domain. Figure 5.10b was recorded with a larger selected area aperture overlapping several domains and shows three different directions of the satellite spots from the different domains.

Figure 5.11a shows a $\langle 111 \rangle$ diffraction pattern exhibiting the typical incommensurate streaking along $\langle 110 \rangle$. On the other hand, figure 5.11b shows a $\langle 110 \rangle$ diffraction pattern showing observations of $\frac{1}{2}(hkl)$ reflections, similar to those reported by Knudsen, Wood-

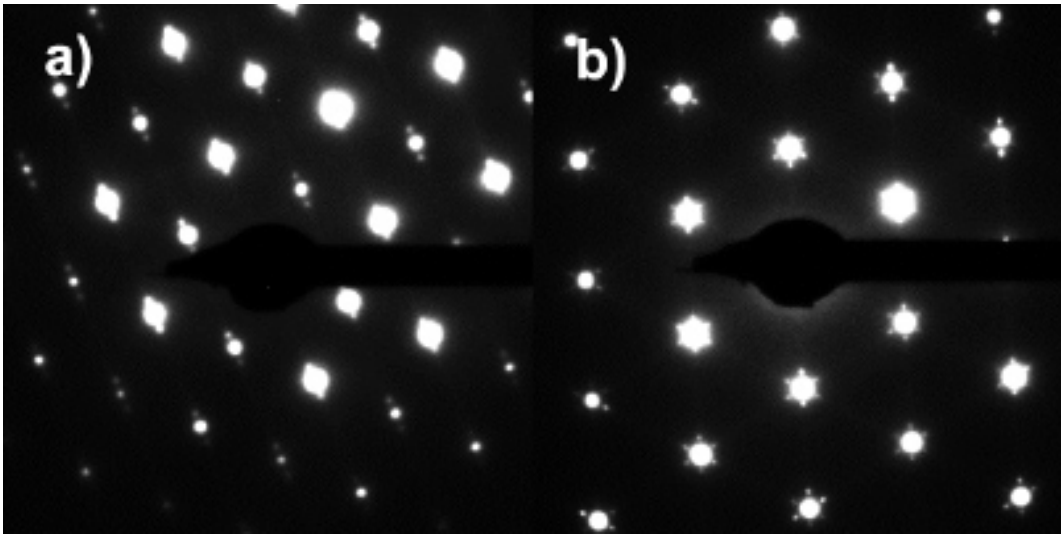

Figure 5.10: Selected area diffraction patterns from 2:90:10 material showing satellite spots arising from the incommensurate antiferroelectric phase

ward and Reaney [10], indicating an antiphase octahedral tilting scheme. In both cases, weak satellite spots are observed about the strong diffraction spots indicating a long period ordering of the crystal structure. So, typically, these materials have very large unit cells, often with periodicities that are not commensurate with the spacings of the primitive perovskite cell [16]. These long periodicities are thought to arise due to competition between antiferroelectric and ferroelectric ordering in these intermediate compositions. The incommensurate modulations spots along the 110 shown in the SADPs can be expressed as $ha^* + kb^* + lc^* \pm (1/n)\{a^* + b^*\}$ [23], where h, k, l, are integers and n can be directly measured from the diffraction pattern. The measured n can be used to derive the modulation wavelength using the lattice parameters [11,32]. The modulation wavelength measured for these incommensurate reflections is $\sim 22.6\mathring{A}$. The spacing of the spots is a factor of 7.70 ± 0.20 shorter than the 110 spacing, which is around $2.93\mathring{A}$, for a unit cell of $4.15\mathring{A}$. Measurements have been made of the periodicity of these satellite spots in many diffraction patterns from all three compositions and they generally correspond to lattice spacings of about 7-8 (110) spacings for all compositions from 2:90:10-4:90:10, in accordance with previous reports [7,9].

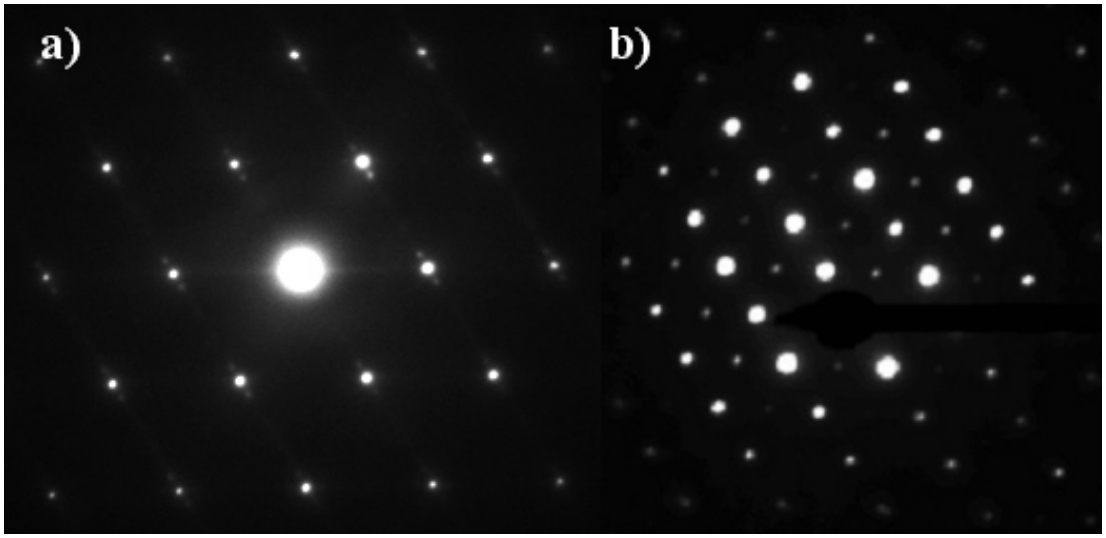

Figure 5.11: Selected area diffraction patterns from PLZT ceramics showing satellite spots arising from the incommensurate antiferroelectric phase a) ⟨111⟩ diffraction pattern exhibiting incommensurate streaking along ⟨110⟩, b) ⟨110⟩ diffraction pattern showing observations of $\frac{1}{2}$(111) reflections.

5.2.2 Detailed characterisation of 60° domain boundarries

5.2.2.1 Structural characterisation using Dark field imaging and selected area diffraction

Whilst 90° domain boundaries have been observed, by far the most common sort of domain boundary observed was the 60° domain boundary, and for this reason the analyses were concentrated on these domain boundaries. Figure 5.12 shows a dark field image of a 60° domain boundary recorded close to a ⟨111⟩ crystallographic orientation, together with two ⟨111⟩ diffraction patterns from the upper and lower domains separated by the boundary. It is clear that the boundary lies on one 110 plane and that the two domains have their long [110] axes at 120° to one another. The [1$\bar{1}$0] polarisation directions must lie at $\sim$ 35° to the beam direction in each grain (and not in the specimen plane like the long [110] axes), and at 60° to one another, but their precise orientation cannot easily be identified from this set of images and diffraction patterns, apart from that it must lie perpendicular to the [110] axis and thus in the same plane as the streaks in the

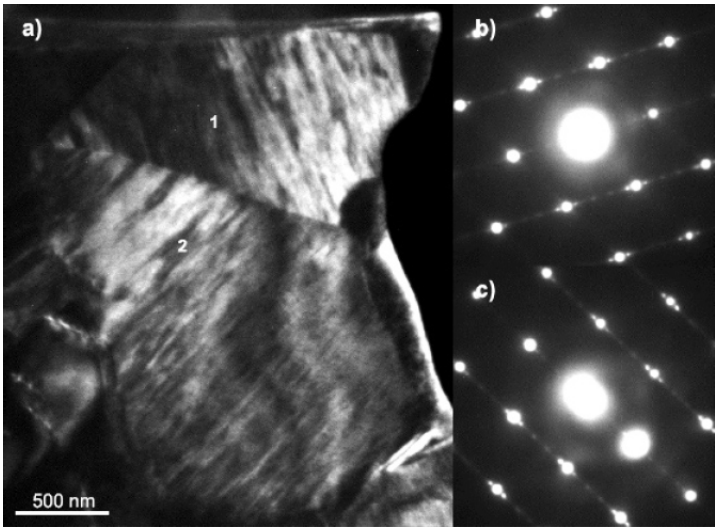

Figure 5.12: DF image of a domain boundary in PLZT 3:90:10, taken slightly tilted off-axis to enhance the nanostructure contrast, together with two selected area diffraction patterns from the upper and lower domains, both recorded along a ⟨111⟩ axis

nanostructure.

Figure 5.13 shows a dark image of a different 60° domain boundary in PLZT recorded close to a ⟨100⟩ direction, as ever, the boundary plane is close to a {101} plane. Selected area diffraction patterns were recorded from both the left and right hand domains and are shown in the top left and top right, respectively. In both patterns the diffraction spots shift from the regular square grid towards the lower edge; in the left hand pattern the shift is a small one to the lower left along a [100] direction, in the right hand pattern the shift goes to the lower right also along a [100] type direction. This is clearly occurring because of the curvature of the Ewald sphere; as the Ewald sphere curves away from the reciprocal lattice points for the primitive perovskite cell, it starts to intersect the incommensurate reciprocal lattice points instead of the reciprocal lattice points for the primitive lattice, as illustrated in the schematic at the bottom of Figure 5.13. The existence of such shifts of reciprocal lattice points at the edges of selected area diffraction patterns has frequently been observed by ourselves and may also be seen in Fig 5.8c of Cai et al. [11]. This also confirms the interpretation of Cai et al. [11] about the shape of the reciprocal lattice of

this incommensurate phase. These shifts at the edges of patterns are actually extremely useful since they allow us to determine the direction of the long $b_{orthorhombic}$ axis, even when this lies out of the plane of the diffraction pattern. Additionally, in this case, since the c-axis must be perpendicular to $b_{orthorhombic}$, then c must lie in plane. Thus, by a process of elimination, it is trivial to determine the direction of the $a_{orthorhombic}$ axis along which the polarisation must lie. Thus, diagrams are set out to the right and the left of Figure 5.13 illustrating the orthorhombic supercell orientation on either side of the domain boundary.

5.2.2.2 Misorientations measurement at 60° domain boundaries and the determination of local crystallography

One feature of this particular orientation of a 60° domain boundary along $[010]_{primitive}$ is that the difference between the $a_{primitive}$ and $c_{primitive}$ lattice parameters should become apparent as a small relative rotation of the two crystal lattices allowing a local measurement of the a/c ratio. This has been performed in one case using selected area diffraction, but the spot splitting is tiny and difficult to measure accurately, but a rotation of $< 1°$ about [010] was found. It is more straightforward to measure such small lattice tilts using orientation measurements from Kikuchi patterns, and the tilt angle can be recovered with reasonable accuracy ($\sim 0.1°$) without too much difficulty [12].

Figure 5.14 shows images of the domain and nanostructure in a 4:90:10 sample together with two processed Kikuchi patterns taken at points 3a and 4, respectively. Such misorientation measurements were recorded from the three different compositions from adjacent 60° domains. The shifts are small and hard to spot but are readily measurable using the Euclide's Phantasies software [1,2]. The misorientation angles were $0.46 \pm 0.18°$ for 2:90:10 (based on 15 measurements), $0.5 \pm 0.29°$ for 3:90:10 (based on 27 measurements), and $0.40 \pm 0.18°$ for 4:90:10 (based on 11 measurements). All these angles agree to within experimental uncertainties, and thus we can conclude that the crystallographic a/c ratio must be similar in all three compositions. This ratio is thus calculated using equation 5.3 as 1.008 ± 0.004, in reasonable agreement with a pseudotetragonal a/c ratio

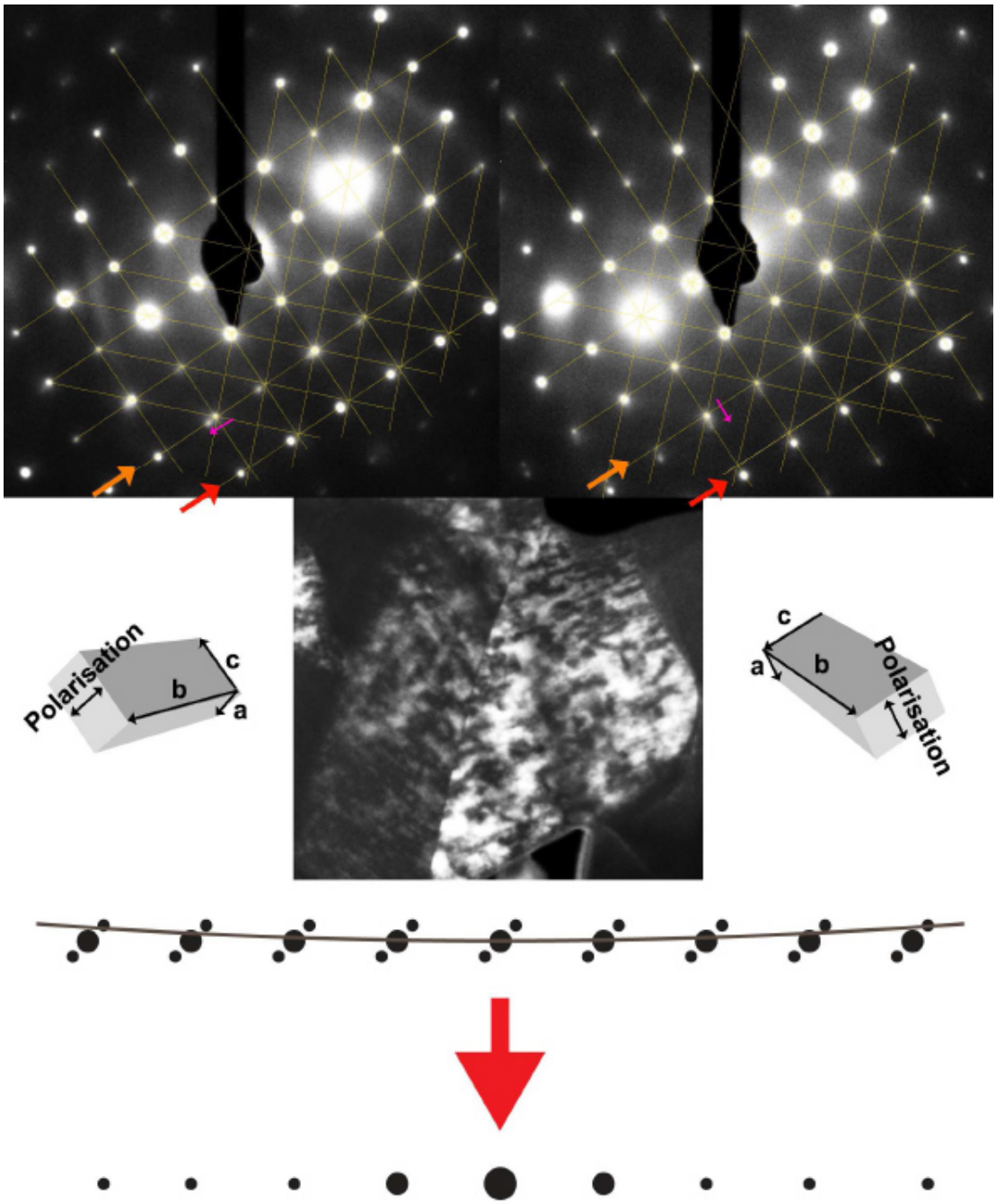

Figure 5.13: Analysis of the unit cell orientations across a 60° domain boundary: the dark field image is recorded close to a ⟨100⟩ direction and selected area diffraction patterns are shown from the domains on the left and right of this boundary.

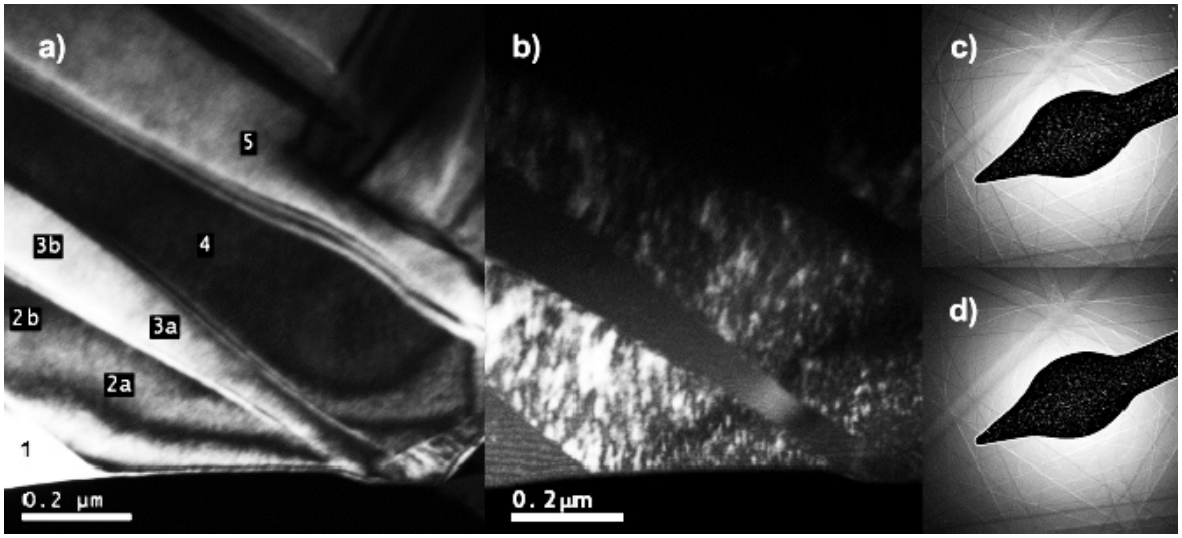

Figure 5.14: Structures in a PLZT 4:90:10 sample: a) Strong beam dark field image of the domain structure; b) weaker beam image of the nanostructure in domains 2 and 4; c) processed Kikuchi pattern from point 3a; d) processed Kikuchi pattern from point 4.

calculated from the published lattice parameters of $PbZrO_3$ [3,8] of ~ 1.012.

5.2.3 In-*situ* TEM heating studies

The relationship between the nanostructure and the micro-sized domains can be understood studying the formation of such nanostructure inside the domains. A very good method to determine the appearance of the nanostructure and their relationship to the domains is the in-situ heating studies in the TEM. As the domain walls are only present below the Curie temperature, it is possible to observe in real time the moment and aproximate temperatures at which the structure of the grains change.

Experiments consisting of heating from room temperature up to 200°C for the three compositions of PLZT ceramics, were carried out in a TEM with a special heating holder. The temperature was increased in steps of 10°C between each image recording. All compositions in the range from 2-4 % La showed a transition temperature close to 160-170°C and the nanostructure disappears either directly at this temperature or within 10°C of it. No changes were found at lower temperatures even in 3:90:10 which changes from

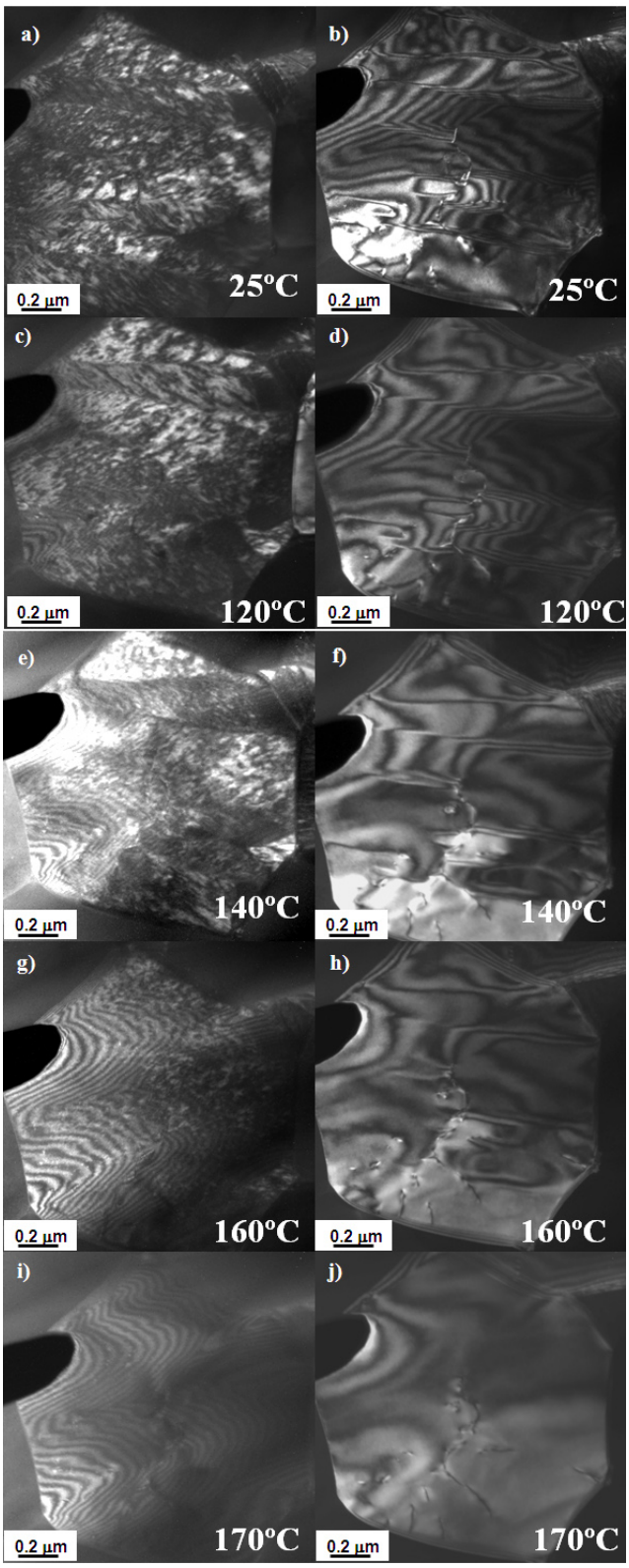

Figure 5.15: Heating sequence in a 4:90:10 PLZT showing the relationship between nano and micro-structure. Both sides images contrast was achieved using a conical beam in the dark field mode.

FE at room temperature to fully AFE above 90°C [28]. Figure 5.15 shows a sequence of images taken in-situ during the heat treatment of a 4:90:10 PLZT ceramic. The images on the right were recorded using dark field tilts to bring strong diffraction spots into the aperture. The images on the left were recorded using weak diffraction spots with satellite reflections of similar intensity to the main spot in order to generate nanostructure contrast as described previously for Figure 5.8. Figure 5.15a shows a DF image of the nanostructure inside the microdomains whilst figure 5.15b shows a DF image of the micro-sized domain structure. Both images were taken at room temperature with different diffraction conditions. Figures 5.15 c and d, are DF images taken at 120°C from the same area than 5.15a and b, showing the relationship between the nano and micro-structure respectively. At this temperature, the nanostructure in figure 5.15c remains the same as at room temperature and no change in domain walls are noticed. The same can be said for the micro-sized domains shown in figure 5.15d as no substantial changes can be noticed. At 140°C there is a slight change in the nanostructure contrast shown in figure 5.15e, although the nanostructure remains in the same direction inside the micro-sized domains. Figure 5.15f shows a slight rearrangement of the domain walls in the bottom part of the image, together with a noticeable rearrangement of the dislocations. At 160°C there is a change in the nano and micro-structure configuration. The domain walls have started to move as can be seen in figure 5.15g, and some of the nanostructure as been erased as shown in figure 5.15h. Nonetheless, it is important to notice that the nano-structure remains in the same direction as at the beginning and the micro-structure has not been erased completely. A drastic change is noticeble at 170°C, the temperature at which, the nanostructure has disapeared completely (as can be seen in figure 5.15i) together with the micro-domain structure (figure 5.15j). The fact that both nano and micro-structure disapear completely at the same temperature (at 170°C) has important consequences. It implies that the Curie temperature should be about 170°C for this composition. It also shows that the fine structure could be an integral part of the antiferroelectric domain structure since it only disappears when the domain boundaries disappear. This argument is based on the supposition that the domain walls will form at the same time that the

nanostructure when the Curie point is reached when cooling from a high temperature to room temperature.

5.2.4 High resolution TEM and STEM studies

As the properties of materials depend both on their microstructure and on the way in which the atoms are arranged, higher resolution investigations are also needed. The aim of using high resolution transmission electron microscopy (HRTEM) is to maximise the useful detail in the image, and obtaining structural information about the material at the length scale of interatomic distances [34]. HRTEM is a powerful technique to study the nano-and atomic structure in modern ceramics. The resolution achieved in such technique is enough to resolve columns of atoms [34]. The point-to-point resolution of a conventional uncorrected HRTEM is usually up to 0.24nm for 200 kV microscopes [29], and it is impossible to distinguish the species of atoms that are located closer within the resolution. On the other hand, scanning transmission electron microscopy (STEM) has been developed to obtain finely focused electron probe less than 0.2 nm and has been applied for characterising modern ceramics. Particularly, a high-angle dark-field STEM (HAADF-STEM) has been used for atomic-resolution imaging [36-39]. In addition, recent development of Cs correction technique enables us to obtain further fine probe size less than 0.1 nm, and has been paid much attention for materials scientists [38]. Z-contrast is expected to be a very powerful technique rather than HREM for characterising ceramics, however, one of the weak points is in observing light elements such as oxygen, nitrogen and carbon because the scattering factor of these elements are small. In recent times one of the most important targets in ceramics nanocharacterisation by TEM is to directly observe light elements such as oxygen and nitrogen, which are main constituent atoms in ceramics. The light elements are frequently bonded to cations at an atomic distance of 0.1 nm [35]. There have been lots of efforts towards a directly imaging of light elements by HRTEM and BF-STEM image using a Cs corrector [40] in order to fully characterise modern electron ceramics. In this sense, the aberration corrected HRTEM has shown to be the appropriate technique in order to imaging the light elements existing in the

perovskite unit cells of such ceramics [41,42].

HRTEM has been used in this work to examine some local areas of the incommensurate structure. Figure 5.16 shows a HRTEM image taken from the domains containing nanostructure at a [001] zone axis with Fourier transform inset and the modulation along the [110] direction is obvious. Based on the results obtained in section 5.2.1 for the modulation wavelength and the spots spacing, we would expect two different blocks of modulated structures: one apparently containing 7 (110) lattice planes and the other containing 8 (110) lattice planes (such models have been found by other workers [11,16]).

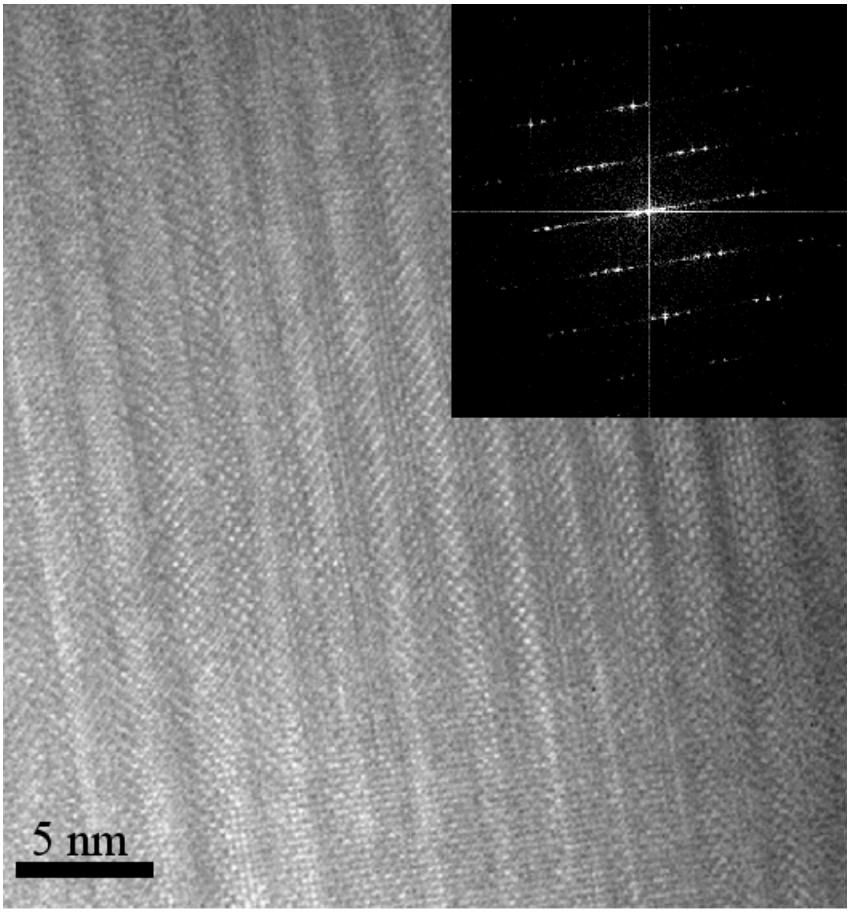

Figure 5.16: HRTEM image taken from the domains containing nanostructure of a 3:90:10 PLZT ceramic, at a [001] zone axis with Fourier transform inset.

More careful observations of figure 5.17, which is an enlargement of the same area reveal that the sequence of blocks can be expressed as a sequence of two main blocks,

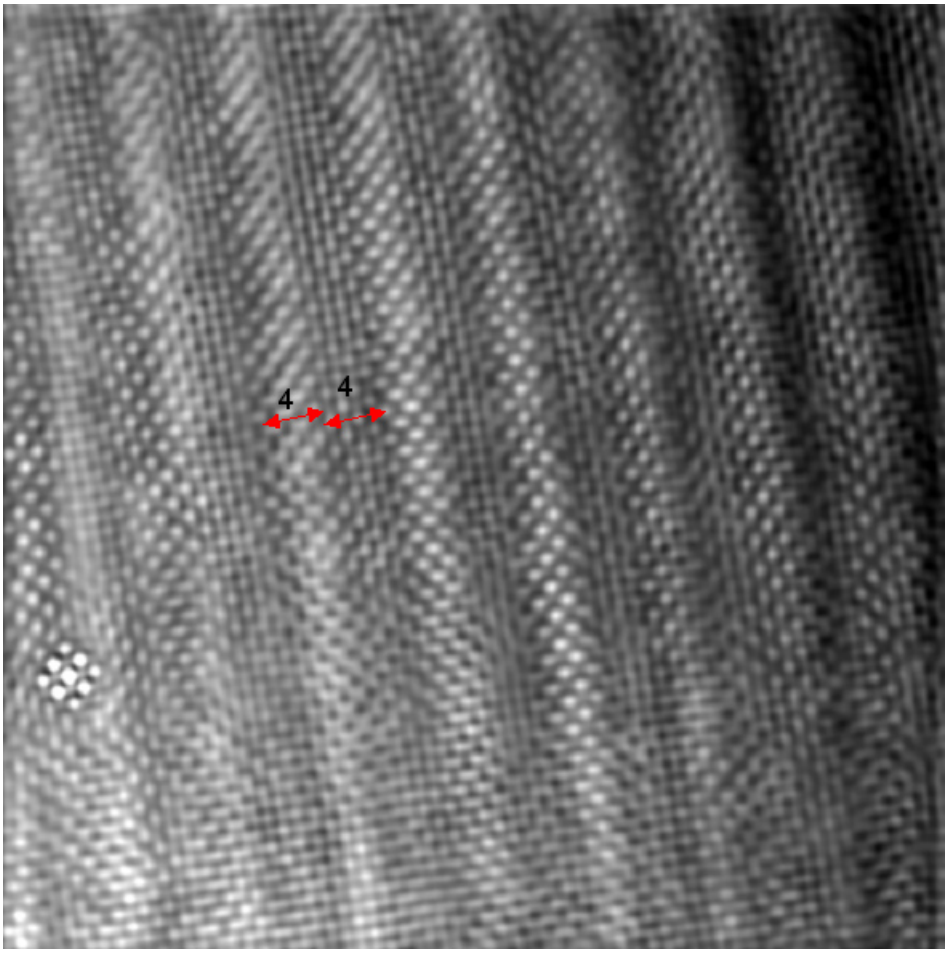

Figure 5.17: Enlargement of part of figure 5.16 , showing the sequence of 4 blocks of modulated structure

each containing 4 (110) lattice planes, making the total periodicity 8 (110) planes, as previously seen [7]. Evidently, if there is a sufficient amount of identical blocks, a locally commensurate area will be formed, albeit with a much longer periodicity than the 4-layer structure of commensurate $PbZrO_3$.

Figure 5.18 shows a HRTEM image from a 90° boundary formed in PLZT 4:90:10 ceramics. Careful examination of the inset reveals that there is not any change in the modulation wavelength from one side to the other, across the domain boundary. Therefore, as the modulation wavelength remain the same, the same description of 2 blocks each containing 4 (110) lattice planes applies.

Taking into account the Fourier transform inset in figure 5.18 we might think that

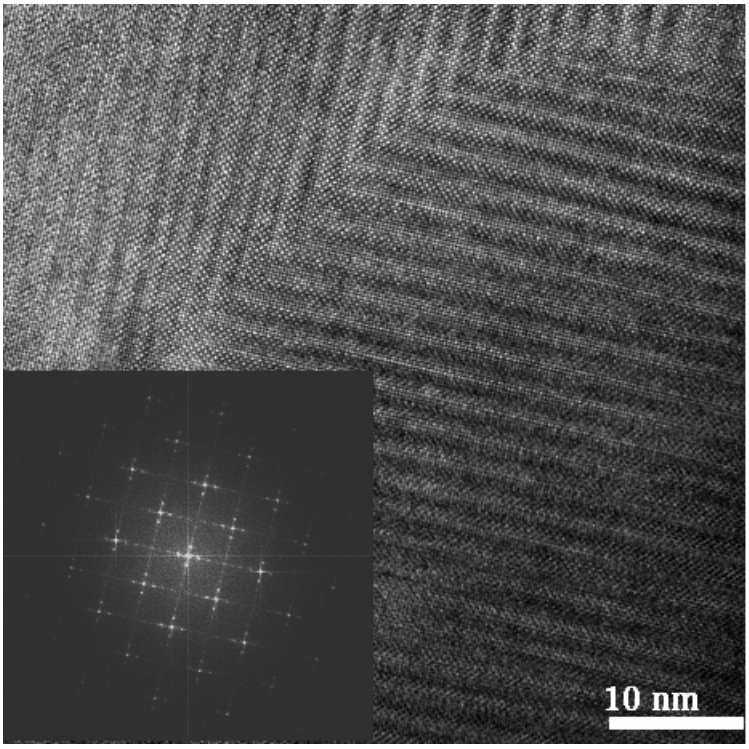

Figure 5.18: HRTEM image from a 90° boundary formed by the modulations in a 4:90:10 PLZT ceramic.

there is no reason to believe in a change of modulated wavelength across the 90° boundary. In order to validate the last argument, high-resolution STEM images from the same 90° boundary were taken using SuperSTEM 2. Figure 5.19a shows the BF image of the 90° boundary taken from an aberration corrected STEM microscope SuperSTEM 2, and figure 5.19b is the same image with a different contrast in order to highlight the 90° boundary. Scanning transmission electron microscopy was carried out using the NION UltraSTEM microscope (Kirkland, WA, USA) at the SuperSTEM laboratory operated at an accelerating voltage of 100 kV and probe semiangle of 36 mrad and the images analysed in this section of the thesis were collected using the High Angle Annular Dark Field (HAADF) mode using a detector with inner radius of 101 mrad and an effective outer radius of 185 mrad. To reduce the effect of scan distortions and readout noise, multiple images were recorded from each area and then cross correlated and summed to produce a sum image using the SDSD drift correction plugin [57] for Digital Micrograph (Gatan Inc., Pleassanton, CA). Figures 5.19a and 5.19b show a scanning transmission electron microscope image recorded with the bright field detector from a single scan of an area suitably oriented with the [001] axis along the beam direction; it is clear in these images that layered structures are present with vertical layers in the lower left and horizontal layers in the upper right with a 90° domain boundary between.

As explained in chapter 3, clear electron microscopy images of PZT ceramics are particularly difficult to acquire because of the charging produced in the sample by the beam. This problem is remarkable when using scanning systems, as they always include distortions to the images. The image shown in figure 5.19a is very noisy and precision atom site location would be difficult and unreliable in this case. This problem was overcome by repeatedly scanning the same area and then cross correlating and summing all the images using a specially designed software tool to produce the average image shown in figure 5.20; this image is much clearer and the atom site locations are much more easily identifiable. It should be noted that the sample was thinnest at the top left and gets thicker towards the lower part, thus accounting for the increased brightness in the lower part. Figure 5.20 shows a processed image result of multiple images of the area

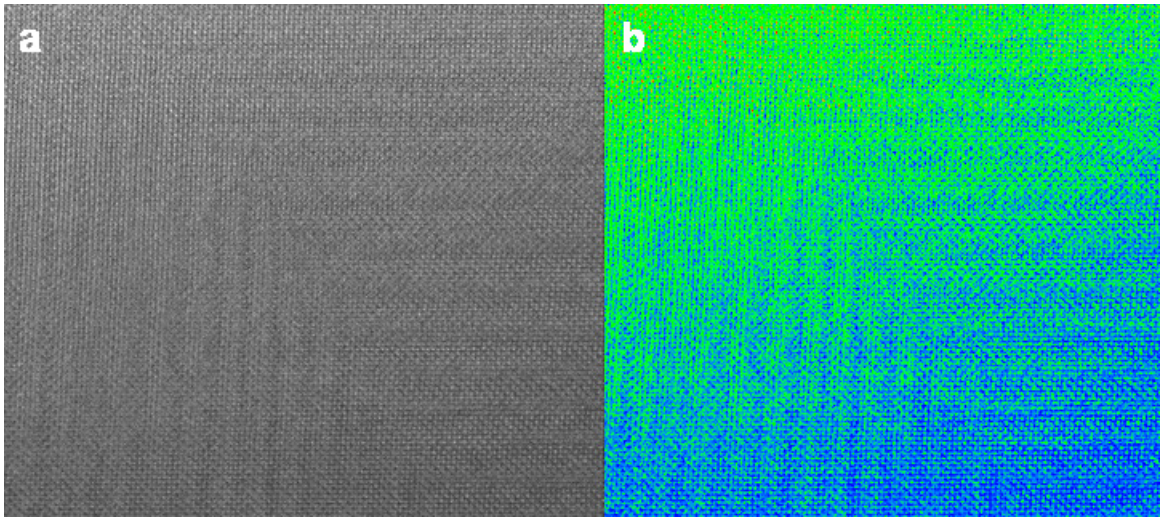

Figure 5.19: Aberration corrected BF STEM image from a 90° boundary in a 4:90:10 PLZT ceramics. Both images are the same a) is in grayscale and b) is false coloured.

including the 90° boundary. It is more difficult to recognise the boundary in HAADF image but it is much easier to study the details of the atomic arrangement. The image was recorded using the aberration-corrected SuperSTEM 2 machine with the incident beam parallel to the [001] direction. This figure was achieved by cross-correlating 28 scans after drift correction with the SDSD plugin [57]. This averaged image is very clear and the atomic sites are easier to identify than in not drift corrected images due to the high noise and drift on the latter. The high atomic number Pb atoms scatter most strongly and are the brightest atoms in the image but weaker atom site positions may also be recognised in the centres of the squares as Zr/Ti positions; weakly scattering oxygen atoms are not visible in this image as explained before.

Figures 5.21 and 5.22 are magnifications of the structure shown in figure 5.20. We can see from figure 5.21 that the atomic arrangement exhibits shifts of the lead atoms with respect to the cubic perovskite structure. These shifts are highlighted with arrows in figures 5.21 and 5.22 and they result in a reduction in symmetry and an increase in the unit cell size. It is possible to notice in both figures the different shift directions which give rise to different atomic arrangements. Two different stacking arrangements can be found: One is a six layers stacking (figure 5.21) and the second one is an eight layers

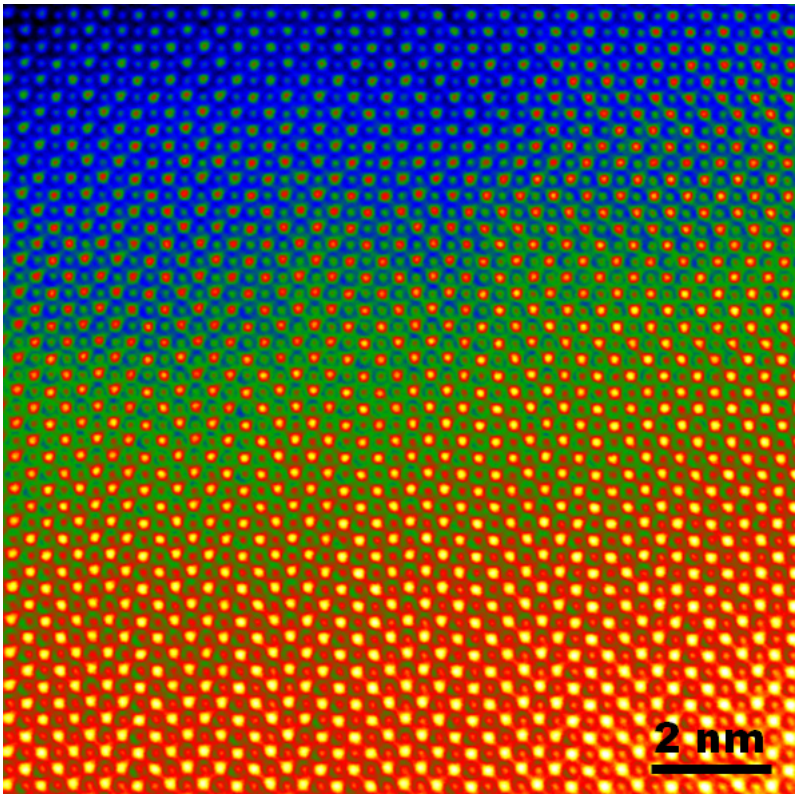

Figure 5.20: Sum image achieved by cross-correlating 28 scans to remove drifts effects. This is the same 90° boundary shown in figure 5.19. The electron beam is parallel to the [100] direction.

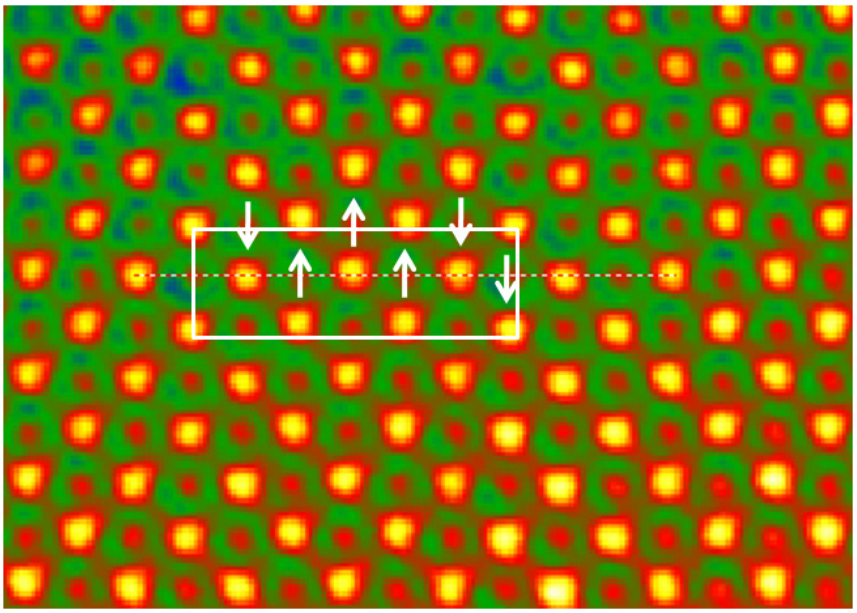

Figure 5.21: Atomic shifts arrangement with unit cell composed by 6 layers. The arrangement is highlighted with the white arrows.

stacking (figure 5.22). The six layers stacking can be found in the left hand side of the 90° boundary, whilst the eight layer stacking can be found in the top right of the same 90° boundary. These two different arrangements are being suggested and they need to be demonstrated in the future using computing techniques to extract from these figures (figures 5.21 and 5.22) the exact atomic possitions and the shifts of the atoms.

In figure 5.22 a unit cell composed of 8 layers is highlighted in the white rectangle, whilst in figure 5.21 a 6 layers unit cell is highlighted in the white rectangle. The shifts in both images are highlighted with white arrows. These 6 and 8 layer stacking sequences, when combined in one domain, would give an incommensurate modulation, thus explaining the 7-8 layer average periodicity obtained from the diffraction experiments. The 6 layer structure has three layers with lead shifted up and three layers shifted down - this must be an antiferroelectric modulation since half is shifted the one way and half the other. Similarly, the 8 layer structure is 4 up and 4 down so we also have an antiferroelectric modulation. It is important say that figure 5.22 was taken from the top right side of the 90° boundary; whilst figure 5.21 was taken from the left hand side of the same

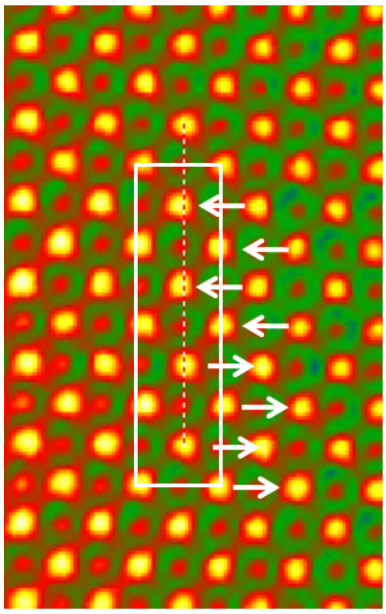

Figure 5.22: Atomic shifts arrangement with unit cell composed by 8 layers. The arrangement is highlighted with the white arrows.

boundary. These results confirm a change in the modulation wavelength across the 90° boundary which was not possible noticing in figure 5.18.

It is interesting to note that the incommensurate phase, which has generally been ascribed to be antiferroelectric dominated all the specimens observed in this work with compositions of 2:90:10, 3:90:10 and 4:90:10, indeed a detailed survey of 10 grains in a 2:90:10 sample showed incommensurate structures in every region of each grain (when sufficient tilt was employed). We never saw any hint of the modulated ferroelectric structure previously observed in a 2:90:10 sample (separately manufactured) by Knudsen et al. [10]. Previous work by Pelaiz-Barranco et al. has shown that 2:90:10 and 3:90:10 are both ferroelectric at room temperature, whereas 4:90:10 is antiferroelectric; nevertheless, X-ray diffraction shows that there are significant quantities of the pseudotetragonal antiferroelectric phase even in 3:90:10 [13]. It may be that thinning the sample has changed the relative stability of the antiferroelectric incommensurate and the ferroelectric rhombohedral phases: the ferroelectric phase would have an extra electrostatic energy contribution when thin due to stray electric fields emanating from the sample surfaces, which would

be an issue for the antiferroelectric phase. This may have prompted a stabilisation of the antiferroelectric phase with respect to the ferroelectric one on thinning resulting in us only finding the antiferroelectric incommensurate phase. This could be the principle behind the results obtained from the in-situ TEM heating experiments carried out on these ceramics. The fact that the domain walls and the streaked nanostructure found inside the micro domains, disappeare at 170°C (very below the Curie temperature) can be due to the change in stability of the antiferroelectric phase. These results are important as well because we can corroborate that the streaked nanostructure is a consistent feature of the incommensurate phase. Such nanostructure is found perpendicular to the incommensurate reflections along [110] directions in the diffraction patterns.

Other interesting facts are that the domain structures are seen everywhere in the incommensurate antiferroelectric phase and that the most common domain boundaries are the 60° domains which have a strong tendency towards {101} planes. This is exactly the same tendency as in rhombohedral materials, where a systematic study found that the majority of rhombohedral domains tend to lay close to {101} planes [14]; in the latter case it is the 71° domains that lay ideally on {101} planes. This idea allows us to think that the rhombohedral FE and orthorhombic incommensurate AFE phases may well be more closely related than is immediately apparent and that it would be possible to transform between the two phases without any gross changes of domain structure.

On the other hand, the rigid body rotation of the perovskite unit cells by about 0.5° shows a remarkable similarity with the $PbZrO_3$ phase. All the evidence thus points to a very clear relationship of the incommensurate phase to the commensurate antiferroelectric $PbZrO_3$ but with a longer periodicity. This longer periodicity can be noticed in figures 5.21 and 5.22, from where it is possible to see that the parallel polarisation bands are wider in the PLZT incommensurate structure than in the typical commensurate structure found in $PbZrO_3$ antiferroelectric (figure 5.6). There is lacking some work in order to perfectly demonstrate the existence of the 6 and 8 stacking sequences suggested for PLZT incommensurate structure. The lacking work must include a method for making quantitative structural measurements. Such a method must extract the peaks

from the top right and bottom left of figure 5.20 in order to show that the antiferroelectric behaviour includes a local ferroelectric ordering. This means that there is a compromise between the antiferroelectric and ferroelectric ordering in these ceramics.

Bibliography

[1] Farooq, M.U., Villaurrutia, R., MacLaren, I., Kungl, H., Hoffmann, M.J., Fundenberger, J.-J. and Bouzy, E., Journal of Microscopy, 230, 445, (2008).

[2] Fundenberger, J.J., Morawiec, A., Bouzy, E., and Lecomte, J.S., Ultramicroscopy, 96, 127-137, (2003).

[3] Corker, D.L., Glazer, A.M., and Dec, J., Acta Crystallographica Section B-Structural Science. 53, 135 (1997).

[4] Yamasaki, K., Soejima, Y., and Fischer, K.F., Acta Crystallographica Section B-Structural Science. 54, 524, (1998).

[5] Megaw, H.D., Proceedings of the Physical Society of London, 58, 133 (1946).

[6] Tanaka, M., Saito, R., Ernst, F., and Tsuzuki, K., Jpn. J. Appl. Phys 2, 21, 291 (1982).

[7] He, H., and Tan, X., Phys. Rev. B, 72(2005).

[8] Glazer, A.M., and Mabud, S.A., Acta Crystall. B, 34, 1065-1070, (1978).

[9] Dai, X.H., and Xu, Z., Li, J.F., Journal of Materials Research, 11, 626 (1996).

[10] Knudsen, J., Woodward, D.I., and Reaney, I.M., Journal of Materials Research, 18, 262 (2003).

[11] Cai, Y., Phillipp, F., and Zimmermann, A., Acta Mater., 51, 6429 (2003).

[12] Bate, P.S., Knutsen, R.D., and Brough, I., J. Microsc. (Oxford), 220, 36 (2005)

[13] Pelaiz-Barranco, A., Guerra, J.D.S., and Garcia-Zaldivar, O., J. Mater. Sci., 43, 6087 (2008).

[14] Ricote, J., Whatmore, R.W., and Barber, D.J., Journal of Physics-Condensed Matter, 12, 323 (2000).

[15] Xu, Z., Viehland, D., and Yang, P., J. Appl. Phys., 74, 3406 (1993).

[16] He, H., and Tan, X., Phys. Rev. B., 72, 24102, (2005).

[17] Tilley, R., Crystals and Crystal Structures, Wiley, (2006)

[18] De Graef, M., and McHenry, M.E., Structure of Materials, Cambridge (2007).

[19] Reaney, I.M., Glazounov, A., Chu, F., Bell, A., and Setter, N., British Ceramic Transactions, 96, 6, 217 (1997).

[20] Hao Quan, Liu Yi-wei, and Fan Hai-Fu, Acta. Cryst., A43, 820-824, (1987).

[21] Jaffe, B., Cook, R. Jr., and Jaffe, H. (1971) Piezoelectric Ceramics, Academic Press, New York.

[22] Kittel, C., 8th edition Introduction to Solid State Physics, John Wiley Son (2005).

[23] Smaalen, S. van, (2007), Incommensurate Crystallography, Oxford Science Publications, [Printed in Great Britain] .

[24] Wagner, T., and Schonleber, A., Acta Cryst., B65, 249-268, (2009).

[25] Smaalen, S., and van, Z. Kristallogr., 219, 681-691, (2004).

[26] Wolff, P.M. de, Acta. Cryst., A30, 777-785, (1974).

[27] Janner, A., and Janssen, T. Phys. Rev. B., 15, 643-658, (1977).

[28] Xu, Z., Dai, X., and Viehland, D., Appl. Phys. Lett., 65, 25 (1994).

[29] Randall, C.A., Markgraf, S.A., Bhalla, A.S., and Baba-Kishi, K. Phys. Rev. B., 40, 413-416, (1989).

[30] Yamamoto, A., and Nakazawa, H. Acta Crystallogr. A., 38, 79-86, (1982).

[31] Asada, T., and Koyama, Y., Phys. Rev. B., 69, 1040108, (2004).

[32] Makovec, D., Zuo, J-M., Twesten, R., and Payne, D.A.., J. Solid State Chem., 179, 1782-1791, (2006).

[33] Zuo, J-M.., and Tao, J., Phys. Rev. B., 63, 060407, (2001).

[34] De Graef, Introduction to Conventional Transmission Electron Microscopy, Cambridge University Press, UK (2003).

[35] Wen, J., Mabon, J., Lei, C., Burdin, S., Sammann, E., Petrov, I., Shah, A.B., Chobpattana, V., Zhang, J., Ran, K., and Zuo, J., Microsc. Microanal., 16, 183-193, (2010).

[36] Pennycook, S.J., and Jesson, D.E., Phys. Rev. Lett., 64, 938, (1990).

[37] Browning, N.D., Chrisholm, M.F., and Pennycook, S.J., Nature, 366, 143-146, (1993).

[38] Yan, Y., Meaden, Chrisholm, M.F., Duscher, G., Maiti, A., Pennycook, S.J. and Pantelides, S.T., Phys. Rev., 81, 3675-3678, (1998).

[39] Abe, E., Pennycook, S.J., Painter, G.S., and Becher, P.F., Nature, 428, 730-733, (2004).

[40] Urban, K.W., Nature Materials, 8, 460-462, (2009).

[41] Matsunaga, H., Nishimura, H., Saito, T., Yamamoto, T., and Ikuhara, Y., Philos. Mag., 83, 4071-4082, (2003).

[42] Spence, J.C.H., Science, 299, 839, (2003).

[43] Dai, X. and Viehland, D., J. appl. Phys. , 76, 3701 (1994).

[44] Haertling, G., and Land, C., J. Am. Ceram. Soc. 54, 1 (1971).

[45] Lines, E. and Glass, M., Principle and Applications of Ferroelectricsand Related Materials (1997) Clarendon, Oxford.

[46] Jaffe, B., Proc IRE 49:1264, (1961).

[47] Pan, W., Zhang, Q., Bhalla, A., and Cross, L.E., J Am Ceram Soc. 72-571, (1989).

[48] Kim, I.W., Lee, D.S., Kang, S.H., and Ahn, W., Thin Solid Films. 441, 115, (2003).

[49] Biggers, J.V., and Schulze, W.A., Bull Am Ceram Soc 53, 809, (1974).

[50] Ishchuk, V.M., Baumer, V.N., and Sobolev, V.L. J Phys Condens Matter 17, 177, (2005).

[51] Zhou, L., Lupascu, D.C., Zimmermann, A., and Zhang, Y., J Appl. Phys. 97, 124106, (2005).

[52] Ranjan, R., and Pandey, D., J Phys Condens Matter 13, 4239, (2001).

[53] Pokharel, B.P., and Pandey, D. J Appl Phys, 88, 5364, (2000).

[54] Xu, Y., and Singh, R.N., J Appl Phys, 88, 7249, (2000).

[55] Bharadwaja, S.N., and Krupanidhi, S.B., J Appl Phys, 89, 4541, (2001).

[56] Xu, Y., Ferroelectric materials and their applications, Elsevier Science Publishers BV, The Netherlands, (1991).

[57] Schaffer, B., Grogger, W., and Kothleitner, G., Ultramicroscopy 102, 27-36, (2004).

Chapter 6

Conclusions and future work

The solid solution system $Pb(Zr_{1-x}Ti_x)O_3$ (PZT) has a complex phase diagram containing a number of materials which exhibit useful ferroelectric and piezoelectric properties. In particular, compositions near the morphotropic phase boundary (MPB) around $x \sim 0.5$ have attached considerable interest for many years due to their high piezoelectric response and technological applications. However, throughout this time, achieving accurate structural studies has been severely hampered by various factors, including complex structural distortions and pseudo-symmetry. Due to this reason, new microscopy techniques based on diffraction and orientation information need to be applied in the study of such ceramics in order to present a clearer understanding of their nanostructure. In this sense, this work presents a reliable comparison between Kikuchi patterns in TEM and EBSD analysis, a precise and valuable analysis of the stress accumulated in these ceramics. Throughout section 4.2, successful EBSD mapping of 90° domain structures in a perovskite ferroelectric has been demonstrated for the first time. The results also allow us to measure the misorientation angle distribution at these domain boundaries and the deviation from 90° allows us to determine the local c/a ratio. Local crystallography has been confirmed as a very accurate analysis method to study domain structure in these ceramics. With local crystallography it is possible to get local (c/a) ratio for tetragonal PZT using either EBSD in the SEM or Kikuchi diffraction. The analysis by TEM and EBSD shows similarities in global results from XRD refinement, but some hints of

local variations. Both methods are suitable for more detailed local crystallography experiments, especially in compositionally graded specimens. Some uncertainties appear in both methods: EBSD dominated by noise in measurement from things like pattern diffuseness, possibly local charging, electronic noise in patterns due to short acquisition; TEM dominated by sample bending and best avoided by staying away from the thinnest areas.

Automated orientation measurement from TEM-Kikuchi patterns from domains in PZT has also been demonstrated for the first time, and comparable results have been achieved. The sources and quality of orientation scatter or noise in both the EBSD system and the TEM have been considered, in EBSD orientation scatter leads to an uncertainty, δ, of the order of 0.16° misorientation measurements on PZT. In TEM, the accuracy of individual measurements is generally better ($< 0.1°$) but is limited by sample preparation since samples often relax on thinning resulting in bending and buckling and this can give errors of greater than 0.5° if too widely spaced points are used for analysis. The effects of such random errors on misorientation angle measurements were considered, and it has been shown that for high misorientation angles this will lead to an approximately cosine distribution of misorientation angles about the mean, with a standard deviation of $\delta/\sqrt{\pi}$, the distribution shape is well reproduced in most cases, and the distribution width matches well to our estimates in some cases, whereas in others higher errors are found. In general we find that the local c/a ratios are in good agreement with global values measured by X-ray diffraction, but some cases have been found where local values appear to show significant discrepancies from XRD values. In addition to the study of Ti-rich PZT, the detailed study of lanthanum doped Zr-rich PZT formed the main part of the work reported in this thesis. When doped with lanthanum at rates of 2, 3 and 4 %, the Zirconium rich (90/10) phase of PZT ceramics show an antiferroelectric behaviour which differs radically from the one exhibited by the Ti-rich phase.

In this work, incommensurate phases achieved by phase transitions in Lanthanum doped PZT were analysed as well as the different domain boundaries presented in such ceramics. In section 5.2, TEM studies of lead zirconate titanate of the Zr:Ti composition

90:10, doped with 2-4 cat. % La show that these samples are dominated by an incommensurate, presumably antiferroelectric, phase characterised by a long period ordering of the unit cell along a single $[110]_p$ direction; this long period ordering is typically 7-8 (110) spacings in length. The microstructure of this phase is dominated by domain boundaries on planes close to $\{101\}_p$, but which often display small deviations from ideal orientations and which are sometimes rather wedge-like in appearance. It is shown using a combination of dark field imaging and selected area diffraction that these are 60° domain boundaries, as have been observed previously in antiferroelectric $PbZrO_3$. Using the Kikuchi diffraction method pioneered in chapter 4, in combination with selected area diffraction, it was shown that there is a rigid body rotation of the perovskite unit cells by about 0.5° about $[010]_p$ due to a contraction of the c-axis in the antiferroelectric phase, also in a similar way to that in $PbZrO_3$. All the evidence thus points to a very clear relationship of the incommensurate phase to the commensurate antiferroelectric $PbZrO_3$ phase, but having a much longer periodicity with a structure which is yet to be fully solved. Each domain contained within it a finer scale nanostructure perpendicular to its long period ordering, and this appeared to arise from planar faulting in the stacking of this long period ordered structure. In section 5.2.4, a high resolution study of the 90° boundary found in a 4:90:10 composition, revealed that the modulation wavelength is the same in both sides of the boundary, and the modulated structure can be represented as stackings of 8 layers stacking (4+4). Nonetheless, when the same boundary was analysed by aberration corrected STEM, it was found that the modulated wavelength changes from one side of the boundary to the other, and that two different stackings can be found of 6 and 8 layers each. By using aberration corrected STEM it was possible to prove that the hypothesis of the 4 layers model deduced by using HRTEM was wrong. As has been demonstrated in chapter 5, this new model includes a six layers structure with three layers with lead shifted up and three layers shifted down. This must be an antiferroelectric modulation since half is shifted one way and half the other. The same can be concluded with the eight layer structure with four layers shifted up and four down. This is as well an antiferroelectric modulation. This results give rise to a new and interesting

model which is the atomic scale roots of the incommensuration for these antiferroelectric ceramics. By stacking 6 and 8 layer cells together we will end up with an incommensurate average periodicity that is less than 8 cells in length. It has been shown as well that high resolution scanning transmission electron microscope images can be used to measure the cation positions. This results allow to make quantitative measurements of the polarisation distribution in the unit cell for the first time in these materials. Work is in progress in this topic and will be published after the completion of this thesis.

6.1 Future work

The aim of this thesis work was to study the structure of different phases of PZT ceramics using traditional bright field and dark field microscopy techniques, together with Kikuchi and selected area diffraction patterns. The electron backscatter diffraction technique was applied as well as part of the microscopy techniques in order to gain different information and to complete the analysis. Even though, a very good understanding of the microstructure and hence the macroscopic properties of these materials was achieved in this work, a lot of work needs to be done. Especial attention requires the Zr-rich phases near the MPB of PZT with compositions between 53 to 60% Zr. Such compositions present very well defined nanodomain structures that need to be analysed using the approach presented in this work, in order to obtain a clear model of the structural changes at phase transitions in these ceramics. On the other hand, nanoscale studies of the mechanisms of temperature-induced orelectric field-induced phase transformations in the morphotropic region in PZT or other perovskite solid solutions, must be carried out using in-situ transmission electron microscopy in order to know how the micro and nanostructure co-exist. These studies have never been done before and using Kikuchi diffraction to monitor local crystallography changes through the transformation would be essential. Many other materials, both perovskite and other, which go through displacive phase transformations will form domain structures that can usefully be analysed by these Kikuchi diffraction and/or EBSD methods and this would provide useful information in understanding such

transformations at the nanoscale.

The discovery that these incommensurate structures indeed represent a so-called bridging phase between ferroelectric and antiferroelectric states in the PLZT system is of huge significance. It is now widely appreciated that optimal properties for piezoelectrics tend to occur close to structural phase boundaries such as the well known morphotropic phase boundaries in systems such as the ones analysed in this thesis (among many other examples). Increasing attention is focusing on the subject of bridging phases and/or nanodomain structures at such phase boundaries that allow easier polarisation rotation or extension giving rise to the bulk properties that are so valuable. Determining the structure of such complex phases or nanostructures is a vital step in understanding how these properties arise and thus the results here are both important for better understanding the specific case of zirconium rich doped PZTs, including the technologically useful antiferroelectric to ferroelectric phase transformations, as well as offering great promise for studying similar bridging phases at other morphotropic phase boundaries. The HRSTEM method presented in this thesis is extremely promising for a wide range of materials which are ordered at the nanoscale, but which do not possess long-range periodicity. With the aid of methods for making quantitative structural measurements on HRSTEM, computing simulations and aberration corrected HRTEM in order to image the oxigen atoms, it can be reasonably expected to complete the detailed unit cell model of these materials.

This analysis is being carried out by MacLaren et. al. at the University of Glasgow. This would be invaluable in understanding phase transformations in these "incommensurate" antiferroelectrics, but would also be much more widely applicable to a whole range of nanostructured materials.